Self-assembly of organic molecules on metals and thin insulating films: Hydrogen-bonded systems, chiral induction and peptide aggregation

Nataliya Kalashnyk

Self-assembly of organic molecules on metals and thin insulating films: Hydrogen-bonded systems, chiral induction and peptide aggregation

NATALIYA KALASHNYK

Interdisciplinary Nanoscience Center (iNANO)
University of Aarhus, Denmark

PhD thesis
October 2009

This thesis has been submitted to the Faculty of Science at the University of Aarhus in order to fulfil the requirements for obtaining a PhD degree in nanoscience. The work has been carried out under the supervision of Associate Professor Trolle R. Linderoth at the Interdisciplinary Nanoscience Center (iNANO).

1st edition
–
This document was typeset and compiled in pdfLaTeX
with Hyperref package
31 October 2009

Contents

List of publications

Publications related to this thesis

[I] *Hydrogen-bonded molecular networks of melamine and cyanuric acid on thin films of NaCl on Au(111)*

Ch. Bombis, N. Kalashnyk, W. Xu, E. Lægsgaard, F. Besenbacher, and T.R. Linderoth, *Small* **5**, 2177 (2009).

[II] *Comparative UHV-STM study of adsorption structures formed by the KFFE and KVVE tetrapeptides on Au(111)*

N. Kalashnyk, J.T. Nielsen, N.Chr. Nielsen, D. Otzen, E. Lægsgaard, F. Besenbacher, and T.R. Linderoth, *In preparation*.

[III] *Synthesis of closely related non-chiral and homochiral C2-symmetric molecular rods and UHV-STM studies of their selective formation of chiral surface patterns on Au(111)*

M.M. Knudsen, N. Kalashnyk, F. Masini, J.R. Cramer, T.R. Linderoth, and K.V. Gothelf, *In manuscript*.

[IV] *Chiral induction by co-adsorption of chiral and prochiral conformational switches on Au(111)*

F. Masini, N. Kalashnyk, M.M. Knudsen, J.R. Cramer, K.V. Gothelf, and T.R. Linderoth, *In manuscript*.

[V] *Self-assembly of hydrogen-bonded chains of molecular Landers on Au(111*)

M. Yu, N. Kalashnyk, R. Barattin, Y. Benjalal, M. Hliwa, X. Bouju, A. Gourdon, Ch. Joachim, E. Lægsgaard, F. Besenbacher, and T.R. Linderoth, S*ubmitted to Small*.

[VI] *Supramolecular architectures on surfaces formed through hydrogen bonding optimized in 3 dimensions*

M. Yu, N. Kalashnyk, W. Xu, R. Barattin, Y. Benjalal, E. Lægsgaard, I. Stensgaard, M. Hliwa, X. Bouju, A. Gourdon, Chr. Joachim, F. Besenbacher, and T.R. Linderoth, *In manuscript*.

[VII] *Self-assemblies of Hydrogen bonded 1D and 2D supramolecular nanostructures formed by two Lander molecules codeposited on Au(111)*

N. Kalashnyk, M. Yu, R. Barattin, Y. Benjalal, M. Hliwa, X. Bouju, A. Gourdon, Chr. Joachim, E. Lægsgaard, F. Besenbacher, and T.R. Linderoth, *In manuscript*.

Other publications

[VIII] *From zero to two dimensions: supramolecular nanostructures formed by interplay between H-bonding and metal-organic coordination*

M. Yu, N. Kalashnyk, W. Xu, Y. Benjalal, S. Nagarajan, F. Masini, E. Lægsgaard, I. Stensgaard, M. Hliwa, X. Bouju, A. Gourdon, Chr. Joachim, T.R. Linderoth, and F. Besenbacher, *In manuscript*.

[IX] *Dimerization of serine on the Cu110surface*

T. Eralp, A. Shavorskiy, Z.V. Zheleva, N. Kalashnyk, Y. Ning, T.R. Linderoth, and G. Held, *In manuscript*.

List of abbreviations

1D,2D,3D	One, two, and three dimensional
A	alanine
AES	Auger electron sepectroscopy
AFM	Atomic force microscopy
ASED	Atom Superposition-Electron Delocalization
Antiparallel	β-strands arrangement in β-sheets
CA	Cyanuric acid
Cross-β	Perpendicular to fibril axis
DAT	$C_{64}H_{68}N_{10}$
DCI	$C_{112}H_{102}N_20_4$
CuPc	Copper phthalocyanine
DC	Decacyclene
DFT	Density functional theory
DNA	Desoxyribonucleic acid
DTP	3,5-di-tert-butyl-phenyl
E	Glutamate
F	Phenylalanine
H-bond	hydrogen bond
HPB	hexaphenyl benzene
EHMO	Extended Huckel Molecular Orbital
ESQC	Elastic Scattering Approach in Quantum Chemistry
HOMO	Highest Occupied Molecular Orbital
KAAE,KFFE	Tetrapeptides
KFFK,KLLE,KVVE	Tetrapeptides
HtBDC	Hexa-*t*-butyl-decacyclene
K	Lysine
L	Leucine

LEED	Low-Energy Electron Diffraction
LUMO	Lowest Unoccupied Molecular Orbital
M	Melamine
MDFF	Molecular Dynamic Force Field
MM4	Molecular Mechanics software code
ND	$C_{58}H_{62}$
NMR	Nuclear Magnetic Resonance
NOE	Nuclear Overhauser Effect
Parallel	β-strands arrangement in β-sheets
Para-compound	1,4-bis[(5-*t*-butyl-3-formyl-4-hydroxyphenyl)ethynyl]benzene
PTCDI	Perylene tetracarboxylic diimide
PVBA	4-trans-2-(pyrid-4-yl-vinyl)benzoic acid
RAIRS	Reflection-Absorption Infrared Spectroscopy
RT	Room temperature
SPM	Scanning probe microscopy
STM	Scanning tunneling microscopy
SubPC	Chloro[subphthalocyaninato]boron
textbfTLES	The ten MDFF lowest energy structures
TPA	Terephthalic acid
UHV	Ultrahigh vacuum
UV	Ultra violet
V	Valine
vdW	van der Waals
VL	Violet Lander $C_{108}H_{104}$
XPS	X-ray photoelectron spectroscopy

List of Figures

CHAPTER 1

Introduction

This chapter introduces the main subjects developed in the thesis. A general description of the basic processes leading to molecular self-assembly at surfaces is given. Specific mechanisms concerning hydrogen-bond mediated self-assembly, chiral systems and biomolecules adsorbed at surfaces are shortly described. It is shown that the latter topic is particularly relevant to better understand self-assembly in protein aggregation.

1.1 Motivation

There's Plenty of Room at the Bottom [1] is the title of a famous public lecture given by physicist Richard Feynman at an American Physical Society meeting at Caltech in 1959. This talk predicted the emergence of an unprecedented interdisciplinary field of science, and the development of a crucially new branch of fabrication technology covering the nanometer length scale.

Nanoscience is concerned with a broad range of phenomena occurring at atomic, molecular and macromolecular scales where properties are significantly different from those at a larger scale. ***Nanotechnology*** in turn refers to the manipulation, the production and the design of materials, structures, devices and systems by controlling their shape and size in the range of about 0.1-100nm. The main feature of nanotechnology is that it spans across all fields of science, touching medicine, physics, engineering and chemistry. Therefore, it has a huge potential to bring benefits in areas as diverse as drug development, medical diagnostics, water decontamination, catalysis, new supersensitive sensors, information and communication technologies, production of stronger, lighter materials, etc.

The engineering of highly organized and functional nanosize systems on surfaces is a main issue of the rapidly growing nanotechnology industry. In order to accomplish this task in a controlled and repeatable manner two basic approaches referred as "top-down" and "bottom-up" are proposed for nanoscale engineering [2, 3]. In the "top-down" approach, the nano-objects, i.e. structures or patterns on the substrate, are produced by methods such as electron-beam writing, and advanced lithography using extreme ultraviolet or hard X-ray radiation [4]. These techniques are able to fabricate surface patterns and devices within sub-100nm range. However, this approach requires huge investments into production facilities, besides fundamental limitation in achievement of desired pattern feature and size. In contrast, the "bottom-up" method deals with processes governing the self-ordering of atomic and molecular constituents adsorbed on well-defined surfaces into organized nanometer-scale architectures, which can be relevant for molecular electronics, nanomechanical devices, surface coatings, biochemical sensors, heterogeneous catalysis.

1.2 Basic processes at surfaces

The growth strategy of 2D molecular nanostructures by "bottom-up" methods requires the comprehensive understanding of adsorption, dynamics and molecular organization on the substrate [2, 5]. Moreover, these surface processes depend on electronic structure and atomic lattice of the substrate. As can be seen from Fig. 1.1, essentially different mechanisms can occur simultaneously on a well-prepared surface exposed to the molecular beam. For instance, single molecules can either adsorb in a definite configuration at specific sites on the substrate or desorb from the surface when adsorption energy is too low. Dynamical phenomena such as diffusion, rotation and conformational interaction direct the growth of molecular structure on a solid surface. These mechanisms are thermally activated since energy barriers have to be overcome when molecules jump from one stable adsorption configuration to another. Surface diffusion has been reported in many cases for large organic molecules, e.g. PVBA and C_{60} on Pd(110) [6, 7], and rota-

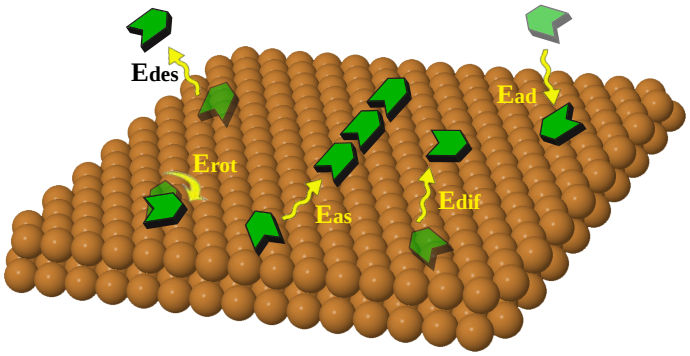

Figure 1.1: Basic processes at surface: adsorption, desorption, diffusion, rotation, assembly.

tion was observed for HtBDC molecules on Cu(100) [8]. Finally, in presence of a suitable adsorbate and appropriate conditions highly mobile molecules can self-assemble into ordered structures via molecular recognition.

1.2.1 Molecular self-assembly

In biology the term self-assembly is introduced to describe processes of biomolecular recognition and organization into stable complex systems, and consequently it appears to be a key factor in the functioning and proliferation of living organisms. The fundamental principles expressed in biomolecular self-assembly have been applied to chemistry, and were recently considered in the context of molecular self-assembly on a surface. *Molecular self-assembly* [9] is the spontaneous association of molecules under equilibrium conditions into stable, structurally well-defined aggregates joined by relatively weak non-covalent bonds such as hydrogen bonds [10, 11], metal-ligand [10, 12] and dipole-dipole [13] interactions.

Hydrogen bonding [14] is the most fascinating example of non-covalent molecular interactions due to its selectivity and directionality properties which offer exceptional potentialities for the design of supramolecular surface structures.

As a result of the development in the area of supramolecular chemistry an enormous number of functionally and structurally distinct molecules became available over the last decade [15]. Such molecules can self-assemble via non-covalent bonding interactions into 3D organized supramolecular architectures with tailored properties. When transferring this approach to surface one has to consider how the chemical nature and symmetry of the substrate influence the non-covalent bonding process of molecular self-assembly. An accurate balancing of intermolecular and surface interactions is then required to ensure supramolecular ordering. For example, non-rigid molecules possess higher number of internal degrees of freedom which allow them to undergo intramolecular distortions [16] or even conformational adsorption on a solid surface [17]. Such conformational switching can also occur in reversible fashion [18]. Furthermore, the molecular symmetry reduction caused by 2D confinement imposes steric constraints for molecular recognition, which may promote 2D molecular chirality [19–21] or supramolecular chiral

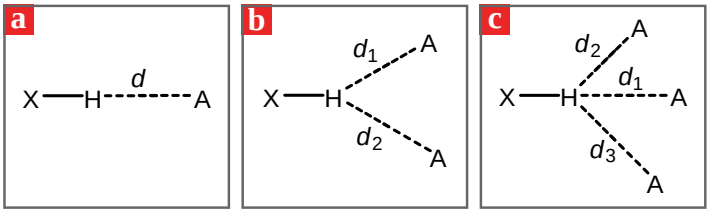

Figure 1.2: Different types of hydrogen bridges. (a) Normal hydrogen bond with one acceptor. (b) Bifurcated hydrogen bond; if the two H···A separations are distinctly different, the shorter interaction is called major component, and the longer one the minor component of the bifurcated bond. (c) Trifurcated hydrogen bond.

ordering [19, 22]. Additionally, the presence of a reactive surface can induce chemical modification in the functional groups of adsorbed molecules. However, thorough selection of substrates with appropriate symmetry, surface patterns or chemical functions makes feasible the exploration of all these effects for steering non-covalent interactions. Besides conventional self-assembly some adsorbed organic molecules may undergo polymerization reaction to form 2D covalently interlinked networks on the surface [23].

Advanced fabrication and characterization techniques with high-level accuracy are required for engineering of atomic and molecular nanostructures at surfaces. In the last decades, a number of sophisticated tools have been invented to study and manipulate matter at ultra-small scales. The most important techniques that revolutionized this field are scanning probe microscopies (SPM). At present both Atomic Force Microscope (AFM) and scanning tunneling microscopies (STM) are recognized as unparalleled tools for imaging material surfaces with atomic resolution, and also for manipulating atoms or molecules on surfaces

1.2.2 Hydrogen bond-mediated self-assembly

Over the last century the hydrogen bond has been the subject of extensive research and debate in various scientific branches including mineralogy, material science, inorganic and organic chemistry, supramolecular chemistry, biochemistry, molecular medicine and pharmacy [14]. The interest in this particular interaction is stimulated by its distinctive features, i.e. high selectivity and directionality. This type of bond offers the inherent ability to form supramolecular nanostructures from both inorganic and organic molecules.

The intermolecular ***hydrogen bond*** is the attractive interaction between the hydrogen attached to an electronegative atom of one molecule and an electronegative atom of another molecule. Consequently, a hydrogen atom is shared by two other atoms [24]. The atom to which the hydrogen is covalently bonded is called the *hydrogen donor* (X), whereas the other atom is the *hydrogen acceptor* (A). These electronegative atoms are usually oxygen, nitrogen, or fluorine, which have a partial negative charge. The hydrogen then has a partial positive charge. As a result, the acceptor with a partial negative charge attracts the hydrogen atom. The length of hydrogen bond is defined to

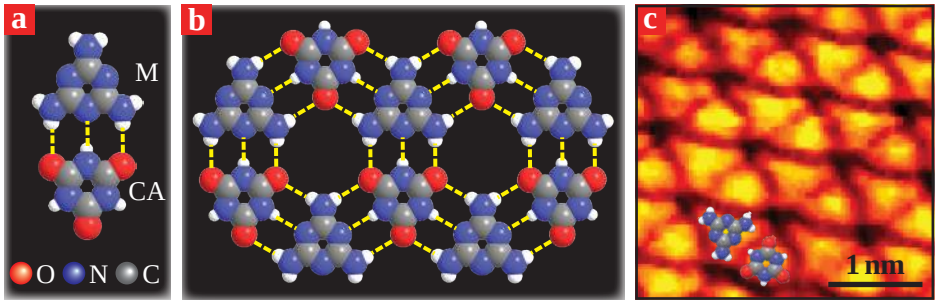

Figure 1.3: Self-assembly of the M-CA system on Au(111). (a) hetero-molecular interaction between cyanuric acid (CA) and melamine (M) molecules. (b) Schematic representation of the M-CA rosette structure stabilized by NH···O and NH···N hydrogen bonds as indicated. (c) STM image of the M-CA rosette structure formed on Au(111) with superimposed molecular models. The characteristic ball- and three-spoke shapes for CA and M are clearly resolved.

be intermediate between covalent (0.96 Å) and van der Waals (3-4 Å) bonds. It implies that the hydrogen bonds are stronger than van der Waals interactions, but weaker than covalent bonds. This bond strength depends on temperature, pressure, bond angle and environment. The strongest hydrogen interaction is anticipated when donor-hydrogen and acceptor atoms are collinear (Fig. 1.2).

In a pioneering work, Whitesides et al. [9] demonstrated the principles for self-assembly of a bimolecular hydrogen-bonded network formed by Melamine (M) and Cyanuric Acid (CA) in aqueous solution. The M-CA system (Fig. 1.3a) is a prototypical model system for molecular self-assembly in which the two compounds are complementary and interact through comparatively strong triple hydrogen bonds, i.e. 2 NH···O and 1 NH···N. This interaction results in the formation of a characteristic hexagonal "rosette" motif which consists of 3 M and 3 CA molecules shown in Fig. 1.3b. Growth of extended molecular networks of the M-CA rosette structure on Au(111) was recently characterized by high-resolution STM [25, 26] as exemplified in Fig. 1.3c. The same complementary hydrogen-bonding interactions are important in a number of other molecular systems guiding the formation of porous networks [27] and molecular chains [28] at surfaces.

This type of triple H-bonding will be the main driving force for molecular self-assemblies described in two other chapters of this thesis devoted to (i) the investigation of M-CA ordered structures on *ultra thin insulating NaCl films* grown on a Au(111) surface (Chapter 5) and to (ii) the self-assembly of Lander molecules on Au(111) which are studied for their possible ability to serve as moulds for growing metal wires (Chapter 6).

1.2.3 Stereochemistry in adsorption systems

One of the most important properties governing the biological and chemical interactions between molecules is *molecular recognition*. It depends not only on the ability of atoms within the interacting molecules to create specific bonding schemes like hydrogen bonds or $\pi - \pi$ interactions but also on the positioning of their atoms in space which de-

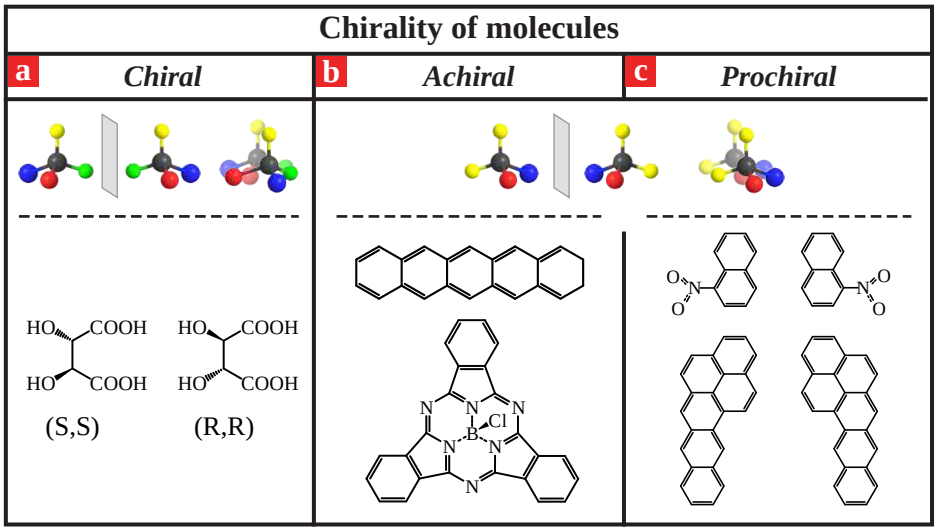

Figure 1.4: Chirality of molecules. (a) Chiral molecules: tartaric acid. (b) Achiral molecules: pentacene and SubPC. (c) Prochiral molecules: 1-nitronaphthalene and naphtho[2,3-a] pyrene.

termines their particular geometrical conformation [21]. The study of the relative spatial arrangement in molecules is a subdiscipline of chemistry called *stereochemistry* [29]. To this area of research belongs the very important class of *chiral* molecules that are non-superimposable on their mirror image by rotation and translation as shown in Fig. 1.4a. The most common type of chiral molecules possesses point chirality at a tetrahedral single atom, usually carbon, attached to four different groups. This central atom is the *stereogenic* (assymetric) centre of the molecule. These molecules can exist in two non-superimposable mirror forms, called *enantiomers*. An equal mixture of enantiomers is said to be *racemic*. Molecules which contain an inversion symmetry or mirror plane are *achiral* (Fig. 1.4b). However, some molecules may bear several chiral centers without being chiral overall.

Molecular chirality was first discovered in 1848 when Louis Pasteur accidentally found out that a crystalline deposit of sodium ammonium tartrate presented equal amounts of left- and right-handed crystals [30] thus forming a racemic mixture of tartaric acid.

Over the past years a large number of experimental works were particularly devoted to surface chirality [15, 19]. The increasing interest to this field has been stimulated by the growing importance of enantioselective heterogeneous catalysis in chemical and pharmaceutical industries [31, 32]. However, surface chirality is not limited to biochemistry. Additionally, and in many instances, thin film chirality is of primary importance for physical applications. Chiral films can possess extraordinary nonlinear optical activity [33] or generate, for example, asymmetric scattering of polarized electrons [34]. As illustrated in Fig. 1.5a, chirality at surfaces can be induced by adsorption of chiral molecules [35, 36]. In some cases, surface chirality can stem even from achiral molecules through their chiral ordering on the substrate (Fig. 1.5c). For instance, a pinwheel struc-

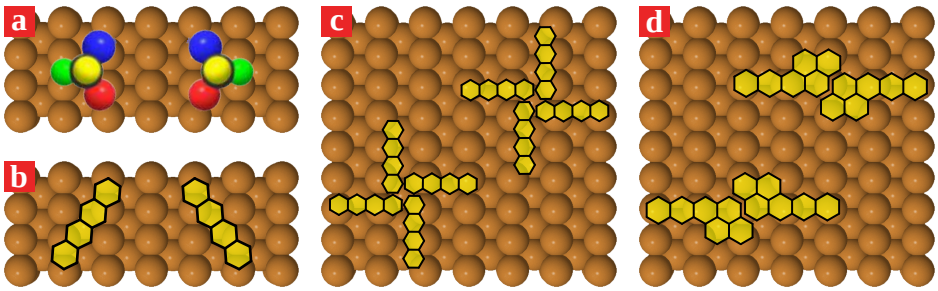

Figure 1.5: Chirality at surfaces. (a) Surface chirality induced by adsorption of chiral molecules. (b) Point chirality for achiral molecules. (c) Organizational chirality by achiral molecules. (d) Surface-induced chirality for prochiral molecules.

ture was observed for intermixed C_{60} and chloro[subphthalocyaninato]boron (SubPC) [22].

Moreover, the chirality of the molecular pattern at the surface can be influenced by the substrate crystallography (see Fig. 1.5b). Benzene adsorbed under UHV conditions on Ni(111) is a classic example [37]. An intermediate case occurs for molecules which are achiral in the gas phase, but become chiral upon adsorption [38–40]. This feature of so-called *prochiral* molecules (Fig. 1.5c) is associated with the reduced symmetry of the adsorbate complex or distortions of the molecular frame due to the interaction with the surface as illustrated in Fig. 1.5d. Adsorption of prochiral molecules always leads to formation of a racemic mixture since two surface enantiomers are formed with equal probability.

The chirality of self-assemblies formed by both *sec*-butyl and codeposited *sec*- and *tert*-butyl oligophenylene-ethynylene molecules on Au(111) will be discussed in Chapter 3 on the basis of previous results obtained in the iNANO group on these systems. It will be shown that co-adsorption of these chiral and prochiral conformational switching molecules is able to induce chirality on Au(111).

1.3 Self-assembly of biomolecules

Inherent complexity and efficiency of biological systems are very strong incentives for combined effort of all sciences to unravel the mechanisms generating their hierarchical organization. Over the last century a lot of attempts were made to understand and subsequently to mimic fascinating structures which nature has been producing for years.

Biomolecules can spontaneously self-assemble into highly-ordered structures. The most well-known example of such behavior is the formation of double helical DNA through H-bonding of the individual strands or protein folding. Importantly, the self-assembly of biomolecules is mainly driven by non-covalent interactions, such as hydrogen bonding, hydrophobic clustering, polar-polar, electrostatic interactions, etc. Balanced cooperation between these interactions leads to the formation of supramolecular structures. Moreover, the environmental conditions can influence on this process which is vital to the normal functioning of biological systems. A small alteration of these subtle

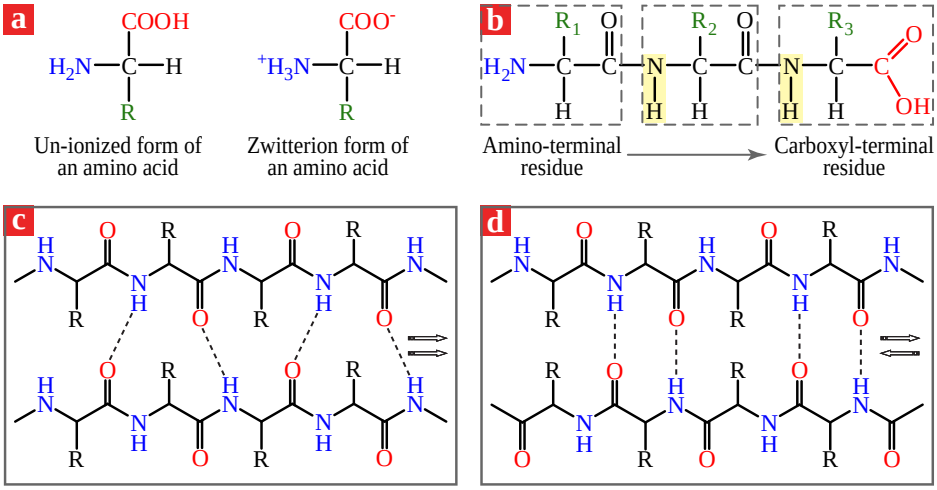

Figure 1.6: (a) The two amino acid forms; (b) Amino-acid residues; (c) Parallel β-sheet formed by two peptide chains (β-strands); (d) Antiparallel β-sheet formed by two peptide chains.

mechanisms will cause hazardous effect on living organisms.

1.3.1 β-(Pleated) sheet

Before introducing the self-assembly of β-sheet proteins into amyloid fibrils, it is necessary to define the terminology associated with this research field. Amino acids are the elementary building blocks of proteins. An amino acid [24] consists of an amino group, a carboxyl group, a hydrogen atom and a distinctive R group which are bounded to an α-*carbon atom* (see Fig. 1.6a). This carbon atom is named α since it is next to the carboxyl (acidic) group and amino acids with an R group bonded to this carbon are referred to as α-*amino acids*. The R group is called a *side chain*. In these acids, the α-carbon is a chiral carbon atom, with the exception of glycine. In gas phase, amino acids are unionized while in solids or polar solutions they exist as zwitterions bearing both positive and negative charges as shown in Fig. 1.6a.

Amino acids combine together into chains to form peptides, polypeptides, and proteins (Fig. 1.6b). In this condensation reaction, the α-carboxyl group of one amino acid reacts with α-amino group of another amino acid to form a CO-NH *peptide bond* or *amide bond* [24]. By convention, the α-amino group ($-NH_2$) and α-carboxyl group ($-$COOH) are defined to be the beginning and end points of a polypeptides chain. Thus, polypeptide chains have a directionality which is usually represented in protein topology diagram by an arrow pointing towards their carboxyl-terminal residues. The polypeptide chain contains a regularly repeating part, called the *main chain* or *backbone*, and a variable part, incorporating the distinctive side chains.

The β-*pleated sheet* is a common secondary structure of proteins [24]. Contrary to an α-*helix*, polypeptide chains in a β-sheet, called β-*strands*, are almost fully extended. Consequently, this biomolecular architecture is stabilized by hydrogen bonds between

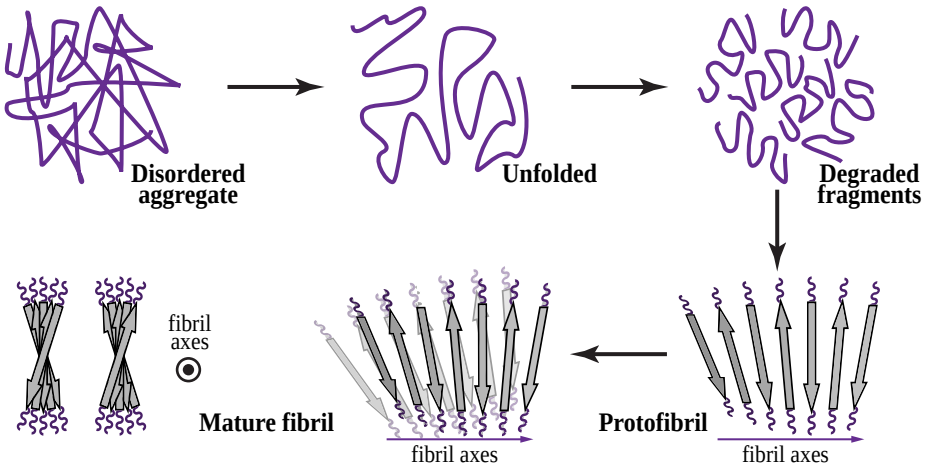

Figure 1.7: The fibrillation process: from disordered aggregates to β-sheets and fibrillar structures.

amine (N−H) and carbonyl (C=O) groups in the backbones of adjacent polypeptides strands, forming a usually twisted and not completely flat sheet. Depending on mutual orientation of β-strands, β-sheets can be either parallel or anti-parallel. If all N-terminus of successive strands point in the same direction the sheet is referred to as *parallel* β-pleated sheet (Fig. 1.6c). In *antiparallel* β-sheets consecutive β-strands adapt their positions so that the C-terminus of one strand is adjacent to the N-terminus of the next one (Fig. 1.6d). Adjacent β-strands run in opposite directions. This arrangement has the strongest stability since the inter-strand H-bonds between carbonyls and amines are planar. Additionally, β-sheets may exhibit a mixed bonding pattern, where some strands are parallel and others are antiparallel.

1.3.2 Formation of amyloid fibrils by peptides

Under specific conditions, proteins and peptides can form toxic oligomers and fibrillar aggregates accumulated in the human tissue in the shape of amyloid plaques which are associated with numerous neurodegenerative pathologies like Alzheimer's, Huntington's, and Parkinson's diseases [41]. The most attention-compelling finding is that inherently different peptides actually generate amyloid fibrils of similar structure.

Based on experimental results a tentative model for hierarchical organization of peptides into such fibers was developed [41]. As illustrated in Fig. 1.7, globular proteins undergo initially the misfolding process. In turn, unfolded proteins degrade into smaller fragments followed by their self-assembly. In a first organizational step, these fragments polymerize into long cross-β-sheets running along the fibril axis. These protofibrils are composed of parallel or antiparallel β-strands that are assembled side-by-side perpendicular to the fibril axis. Cross-β means that the strands of a β-sheet run perpendicular to the fibril axis. A preferential 1D growth of β-sheets can ensue from the formation of strong H-bonds parallel to their axes. Finally, these extended sheets can self-assemble

into mature fibrils stabilized by hydrophobic clustering of the side chains perpendicular to the fibril axes. Initially, the ability to form amyloid structure was assigned to the relatively small number of large proteins and peptides. However, it was shown that even short fragments of amyloidogenic proteins can give rise to fibrilar structure.

1.3.3 Adsorption and organization of biomolecules on surfaces

Over the last decade, a lot of studies were devoted to the self-assembly of biomolecules at solution-surface interfaces. It was demonstrated that templates can induce large-scale order in peptide assembly [42–44]. Such ordering might be quite different from that observed in the physiological environment. This comes from the fact that molecules adsorbed on a surface have less degree of freedom than in vitro.

An understanding of the processes driving self-assembly of biomolecules motivates the investigation of the H-bonding interaction which is known for example to determine the conformation and biochemical activity of nucleic acids. RNA and DNA strands are indeed stabilized via H-bonds provided by the complementary nucleobase pairs.

Therefore, the study of H-bonding interaction between nucleobases in the absence of any other perturbing interactions is an essential starting topic for more complex explorations inolving larger molecules. This can be achieved by depositing these small biomolecules onto ultra-clean inert surfaces such as Au(111) in controlled UHV conditions. Such studies are relevant not only to understand the topology of large biomolecular structures, but also in an attempt to comprehend the self-organization of spontaneous formed biomolecules into early precursors of life which might have occurred via adsorption onto natural surfaces. The problem of finding what kind of interactions occur between biomolecules adsorbed at surfaces is also crucial in the study of protein aggregation and amyloid fibril formation which are responsible for a number of neurological pathologies.

Previous works have shown that small organic molecules such as nucleobases and amino acids bearing several kinds of interacting functional groups can form many self-assembled structures on surfaces [45–49]. For example guanine self-assembles into a H-bonded network having the same square arrangement as that found in DNA sequences which are rich in guanine [11, 50]. Thymine has been reported to form extended ordered 2D patterns and isolated chains when deposited onto the Au(111) surface [51]. Surface-induced chirality in self-assembled molecular chains of adenine has been evidenced on the Cu(110) substrate [52]. Additionally, a few studies concern the self-assembly of dipeptides onto surfaces [53–55].

All these examples show that the determination of biomolecular interactions in UHV surface studies is a fundamental issue for understanding biophysical processes. This context motivates the study of tetrapeptide self-organization discussed in Chapter 4 in the more general frame of the H-bonding, which takes place in all the molecular self-assembled structures described in this thesis.

1.4 Outline of the thesis

The present PhD thesis consists of a number of STM studies spanning through self-assembly processes of different adsorbates on both metallic and dielectric surfaces. Chapter 2 gives a short introduction to the theoretical background of the experimental

technique. Additionally, the Aarhus STM, ultra high vacuum (UHV) chamber and theoretical methods used in the present studies are briefly discussed. Chapter 3 is concerned with self-assembly of *sec*-butyl molecules on the Au(111) substrate. In order to induce global homochirality on the surface, an effort to transfer enantiomorphous structure from truly chiral *sec*-butyl molecules to prochiral *tert*-butyl molecules was done. Chapter 4 is dedicated to a comprehensive study of tetrapeptide self-assembly on Au(111). This investigation provides evidence that short peptides can self-organize into both parallel and antiparallel configurations. Chapter 5 describes self-assembly of cyanuric acid and melamine molecules simultaneously deposited on NaCl/Au(111) surface. It is shown that the stabilization of 2D molecular structures on an ultrathin insulating NaCl layer can be achieved at submolecular coverage and relatively high temperature of 160K with complete molecular decoupling from the metallic Au(111) substrate. Chapter 6 gathers several studies on the deposition and codeposition of large molecules known as Landers. Chapter 7 summarizes the main experimental results acquired during this research, and outlines perspectives for future work.

CHAPTER 2

Methods

In this chapter, the operating principles of scanning tunneling microscopy under ultrahigh vacuum conditions are given. Another section is a short description of two theoretical tools used to simulate STM images of molecules adsorbed on a surface and to calculate biomolecular structures from STM image features.

2.1 Scanning tunneling microscopy

The determination of surface structure is one of the most essential problems in surface physics. The invention of scanning tunneling microscopy (STM) [56] has revolutionized surface science by providing a *direct*, *real-space*, *local probe* technique with a high atomic-scale resolution [57]. STM is an outstanding surface science tool because of its ability to investigate, atom-by-atom, the electronic and geometric structure of surfaces [57, 58], by contrast to conventional techniques like low-energy electron diffraction (LEED), X-ray photoelectron spectroscopy (XPS), Auger electron spectroscopy (AES). These features permit the STM unparalleled effectiveness to explore the structure of conducting surfaces of metals, semi-conductors, transition metal oxides, and metallic nanoclusters with molecules supported on these substrates at an atomic scale. Moreover the STM has been widely used as a powerful tool to study chemisorption [59], epitaxy [60], solid-liquid interfaces, biological molecules [61] and electron confinement with quantum size effects [58] on metal surfaces. Apart from enabling atomic-resolution imaging, the STM has proved to be an unique and crucial manipulation tool for controlled moving of single atoms [62], molecules [63] or clusters [64] on a surface with atomic-scale precision. This finding has opened up a potential route for formation and characterization of single chemical bonds [65], and furthermore for building artificial nanostructures by assembling of adsorbates [2]. The principal limitation of STM is that it requires a conducting substrate. In the case of insulating surfaces this drawback is overcome by using ultrathin insulating films on conducting substrates [66, 67]. So, STM can also investigate the electronic structure and self-assembly of adsorbates on these insulating films [68, 69]. As a result, it is an important technique in a number of key nanotechnology areas such as miniaturization of electronic circuits and devices, molecular electronics, quantum computers, nanochemistry, etc [70].

2.1.1 The principle of STM

The first scanning probe microscope was developed in the early 1980's by Gerd Binnig and Heinrich Rohrer [56] at the IBM Zurich Research Laboratory in Rüschlikon (Switzerland). A tremendous contribution of STM to world science was acknowledged already in 1986 when inventors of this marvelous instrument were awarded the Nobel Prize in Physics.

The working principle of the STM is based on the quantum mechanical tunneling effect. As can be seen from Fig. 2.1, when the metal tip is brought in very close proximity of the conducting surface ($\leq$ 10 Å), but *not* actually in physical contact, and a small bias voltage is applied between them, the electrons can tunnel across the tip-surface gap. Such current is called *tunneling current* which is the result of the overlapping wavefunctions between the tip atom and surface atom. As it will be demonstrated in section 2.1.2, the magnitude of the tunneling current, measured in the nano-ampere range, is extremely sensitive to the gap distance between the tip and the sample, the local density of electronic states of the sample and the local barrier height. Thus, the inherent surface sensitivity of STM can be well understood from an idealized potential-energy diagram for the electrons in a metal tip and in a conductive sample a distance z apart, with work functions ϕ_t and ϕ_s, respectively, and a positive or negative bias voltage V_t

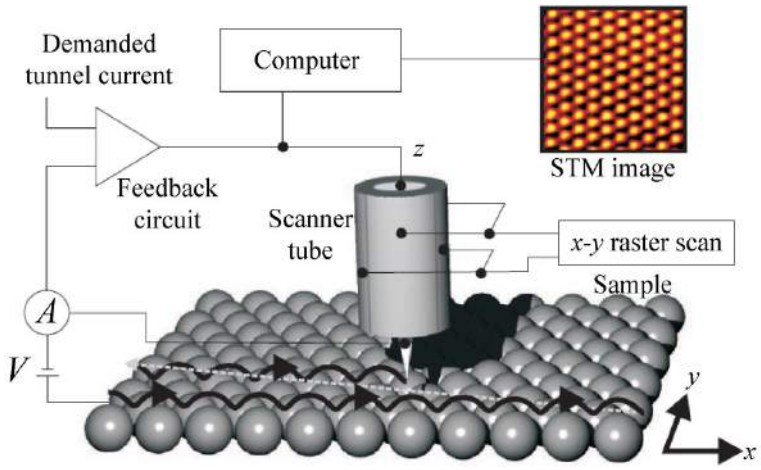

Figure 2.1: The operative principle of the scanning tunneling microscope (STM).

applied to the sample (Fig. 2.2). As follows from this diagram, the work function is the energy required to move an electron at the surface from the Fermi level (E_F) to the vacuum (E_V), and consequently prevents electron transport between the two electrodes. A positive sample bias, $eV_t > 0$, permits electrons occupying filled states on the tip to tunnel elastically into the energy equivalent empty states on the sample (Fig. 2.2). For a negative sample bias, $eV_t < 0$, electrons will tend to tunnel out of the filled states of the sample, into the empty states of the tip.

The foremost operational mode of STM is the so called *constant current imaging*. In this mode the feedback circuit controls the tip position in such a way that the tunneling current and, hence, the tip-surface distance is kept constant, while the tip is raster-scanned across the surface. Thus, when a protrusion is traversed, the feedback signal provides a correction voltage to the z transducer, and consequently causes the displacements of the metal tip. These height modulations are recorded and used to produce a topographic image of the surface via computer.

2.1.2 Theory of STM

In order to understand and interpret the STM images for different surfaces, it is required to determine the tunneling current. However the tunneling between tip and surface is a complex many-body problem, which at present has not been solved exactly. The "perturbative-transfer Hamiltonian" formalism introduced by Bardeen [71] in 1961 was implemented in several tunneling theories applied to STM. This formalism neglects the interaction between surface and tip, so that the corresponding wave functions can be calculated separately. Then, in the first-order perturbation theory the tunneling current can be written as

$$I_t = \frac{2\pi e}{\hbar} \sum_{\mu\nu} f(E_\mu)\left[1 - f(E_\nu + eV_t)\right] \times \left|M_{\mu\nu}\right|^2 \delta(E_\mu - E_\nu) \tag{2.1}$$

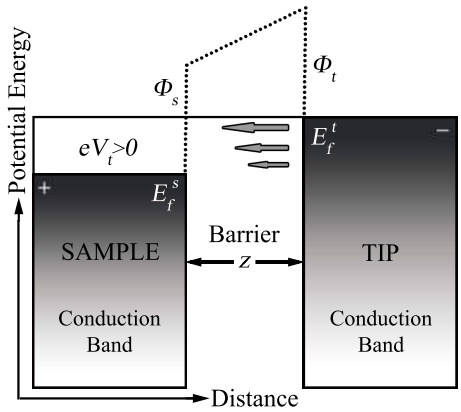

Figure 2.2: Schematic diagram of metal-vacuum-metal system for positive bias voltage.

where $f(E)$ is the Fermi function, V_t is the bias voltage, $M_{\mu\nu}$ is the tunneling matrix element between the tip states ψ_μ with energy E_μ and the surface states ψ_ν with energy E_ν. The Fermi functions in Eq. 2.1 entail that tunneling take place, for instance, from a filled tip state, $f(E_\mu)$, into an empty surface state, $1-f(E_\nu+eV_t)$ at positive bias. The crucial point, in the calculation of the tunneling current, lies in evaluating the matrix element $M_{\mu\nu}$. Bardeen [71] showed that

$$M_{\mu\nu} = \frac{\hbar^2}{2m}\int \overrightarrow{dS}\cdot\left(\psi_\mu^*\overrightarrow{\nabla}\psi_\nu - \psi_\nu\overrightarrow{\nabla}\psi_\mu^*\right) = \frac{\hbar^2}{2m}\int \overrightarrow{dS}\cdot\overrightarrow{j_{\mu\nu}} \tag{2.2}$$

where $\overrightarrow{j_{\mu\nu}}$ is the current density operator and m is the electron mass. The integration is over any surface lying entirely within the vacuum gap region. In 1983, Tersoff and Hamann [72, 73] developed a simplified STM theory based on Bardeen's formalism. They made assumption that the tip is spherical, and therefore well-described by a spherically symmetric s-wave function. For small bias voltage the tunneling current Eq. 2.1 can be reduced to

$$I_t \propto V_t\sum_\nu |\psi_\nu(\overrightarrow{r_t})|^2\,\delta(E_\nu - E_F) = V_t\rho(\overrightarrow{r_t}, E_F) \tag{2.3}$$

where $\rho(\overrightarrow{r_t}, E_F)$ is the local density of states (LDOS) of the surface at the Fermi level evaluated at the centre of the tip apex $(\overrightarrow{r_t})$. It follows that the STM images obtained at constant current mode are images of the contours of LDOS for the surface.

As result of the exponential decay of the surface wave functions in the vacuum region, the tunneling current varies exponentially with the distance z between tip and surface:

$$I_t \propto V_t \exp\left(\frac{-\sqrt{8m\phi}z}{\hbar}\right) \tag{2.4}$$

where ϕ is the effective tunneling barrier height. The ability of STM to achieve atomic resolution is based on this exponential dependence.

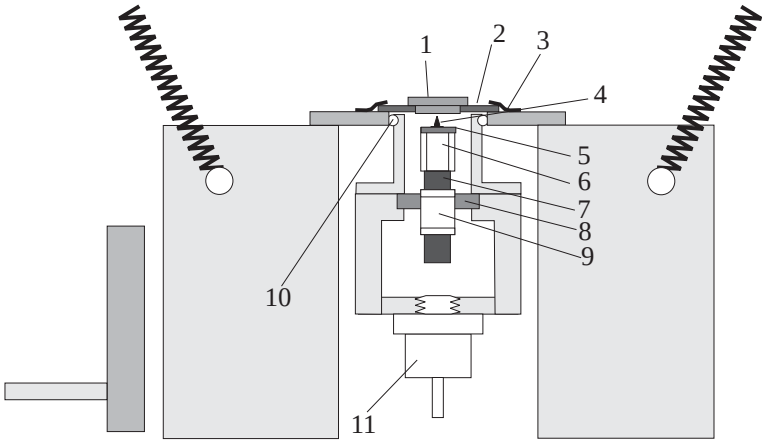

Figure 2.3: Schematic drawing of the Aarhus STM.

2.1.3 The Aarhus STM

To utilize the STM principle in real experiments one has to overcome a number of technical obstacles to ensure that the position of the tip and sample is within sub-Ångstrøm precision. All experimental data presented in this work has been obtained with the home-built Aarhus STM designed by Erik Lægsgaard et al. [74].

The schematic drawing of the Aarhus STM is given in Fig. 2.3. The sample (1) is mounted in a tantalum sample holder (2) which is clamped into the contact with the STM top plate by two copper springs (3). The top plate is thermally and electrically insulated from the STM body by three quartz balls (10). The top plate is mounted on a Al block, which can be cooled via solid/solid contact to a liquid-nitrogen cooled dewar. It is thus possible to achieve a sample temperature of 115 K, while keeping the scanner part (4-9) with piezoelectric elements at RT by a counter heating with a Zener diode (11). During scanning block and dewar should be disconnected and no longer in contact.

The scanning itself is performed by a tungsten tip (4) held by a macor holder (5) which is glued to the top of the scanner tube (6). The scanner tube is made from piezoelectrical elements which constitute an inner single electrode and an outer electrode divided into four equal sections. The scanning in the $x-y$ direction, as result of tube deflection, can be achieved by applying a high voltage antisymmetrically to two opposite sections of the 4-fold segmented electrode with respect to the inner electrode. By applying voltage to the inner electrode relative to the whole outer electrode the length of the tube can be changed. In this manner, the tip-surface distance can be adjusted in the sub-Ångstrøm scale. The scanner tube is glued to the rod (7) which together with the piezo tube (9) forms a small inchworm motor used for coarse approach. The electrode of this tube is divided into three rings. The upper and lower electrodes simply clamp and unclamp the piezo tube to the rod while the centre electrode elongates or contracts. With the right sequence of voltages applied to the three electrodes the rod will move up or down since the tube is fixed to the STM body by the macor ring (8).

2.2 UHV chamber

Ultra high vacuum (UHV) is the vacuum regime characterised by pressures lower than 10^{-9} mbar. Only such low pressures can insure that a surface is kept ultraclean for a time long enough to do experiment. UHV requires the use of compatible materials like stainless steel for pipes, copper for gaskets, and extreme cleanness to maintain high vacuum. The entire system should also be baked to remove airborne molecular contamination like water and other trace gases.

In the ongoing experiments an atomically clean Au(111) single-crystal surface was prepared in UHV chamber by a standard sputtering/annealing procedure. A typical cleaning cycle for this substrate is sputtering with 1.5 keV Ar^+ ion for 20 min followed by annealing at 850 K for 10 min. Sample sputtering is performed by a differentially pumped sputtergun, while its annealing is done with a filament mounted in the sample house at the end of the manipulator. An automated system controls the sputtergun and the filament in the sample house. For molecular evaporation a home-built evaporator is mounted in the UHV chamber. In order to eliminate molecular contamination, the evaporator is isolated from the main UHV chamber by a gate. Additionally, the chamber is equipped with the above described home-built STM and a differentially pumped mass spectrometer, enabling the rest gas analyses.

2.3 STM image simulation with EHMO-ESQC method

The group of CEMES in Toulouse has developed a specific STM image calculation technique based on the EHMO-ESQC method. It is a combination of the extended Hückel molecular orbital (EHMO) theory and of the elastic scattering approach in quantum chemistry (ESQC). The ESQC technique uses a full molecular orbital description of STM tip-adsorbate-surface tunnel junction to calculate the corresponding current in a multichannel scattering approach between the bulk of the tip and the metallic bulk underneath the surface [75]. It allows computing the molecular orbitals and the corresponding energy levels of the molecule adsorbed at the surface. This calculation technique has proved to be very reliable to simulate experimental STM images of various small and large molecules adsorbed on metallic and semiconducting substrates and on thin insulating films.

Efforts are made to reduce considerably the computation time since this method requires the optimization of the atomic and orbital composition of the tip apex and of the conformation of the molecule. The calculated STM image should match as precisely as possible the corresponding experimental one in the x,y plane. There is no way to deal rapidly with an automated procedure taking into account the distance z at which the molecule is adsorbed at the surface. Therefore, automatic investigation of the molecular conformational states on surfaces is practically very slow and time consuming, and the optimization relies mainly on faster successive "manual" and not fully automated steps to reach the observed conformation.

2.4 Restrained molecular dynamic force field method

The restrained molecular dynamic force field (MDFF) is a computational method to simulate the macromolecular structure of proteins [76]. This method is based on the

following protocol:

1. A force field is defined mimicking the chemical properties of the molecule.
2. The dynamics of the molecule is simulated by using the energy derivative in a Newtonian mechanics set-up.
3. The hybrid energy with (empirical) distance restraints is calculated.

In the restrained MDFF approach the total (or hybrid) potential energy E_{tot} of the system is minimized to obtain the most probable structures. E_{tot} is the sum of the chemical force field energy E_{FF} and of the experimental restraint energy E_{exp}

$$E_{tot} = E_{FF} + E_{exp} \tag{2.5}$$

E_{FF} is the potential energy of the system obtained from a priori knowledge of atom masses, covalent bond lengths and angles, vdW and Lennard-Jones potentials, electric charges, force constants, chirality, peptide geometry (trans-cis etc.), planarity (peptide bonds, aromatics).

E_{exp} is an empirical energy obtained from experimental data. This energy is implemented with restraints. It is possible to use various types of distance restraints, for example

$$E_{exp} = \sum_i K_i \Delta_i^2 \tag{2.6}$$

where

$$\Delta_i = d - d_0 \tag{2.7}$$

is the difference between the calculated distances d, and the ideal measured distances d_0 which will be the distances determined from STM images in Chapter 4. The functional form of the AMBER "force field" used to simulate biomolecules writes as

$$E_{FF} = \sum_{bonds} K_r (r - r_0)^2 + \sum_{angles} K_\theta (\theta - \theta_0) + \sum_{dihedrals} \frac{V_n}{2} [1 + \cos(n\phi - \gamma)] + \sum_{i<j} \left[\frac{A_{ij}}{R_{ij}^{12}} - \frac{B_{ij}}{R_{ij}^{6}} + \frac{q_i q_j}{\varepsilon R_{ij}} \right] \tag{2.8}$$

where r_0, θ_0, and γ are the ideal bond lengths, angles, and dihedral angles and K_r, K_θ, and V_n are the corresponding force constants. In Eq. 2.8, the first and second terms represent the energy between covalently bonded atoms and the energy due to the geometry of electron orbitals involved in covalent bonding. The third term is the energy for twisting a bond. The fourth term represents the non-bonded energy between all atom pairs, which can be decomposed into vdW and Lennard-Jones potentials, and electrostatic energy. The R_{ij} are the distances between atoms, q_i the charges, and A_{ij}, B_{ij} are parameters.

The most probable structure is calculated when a global minimum is found at the energy surface. Energy minimization of the hybrid energy function can be precluded by convergence toward a local minimum instead of the global minimum, especially in

the refinement of macromolecular structures like proteins. A way to circumvent this problem is to introduce an efficient minimization method called the simulated annealing. The method mimics the annealing of metals. The initial velocities of each atom are assigned according to the Boltzmann distribution. This allows to calculate the atomic accelerations using small time steps, and to derive the atomic coordinates by numerical integration of the velocities and the force from the derivative of the potential hybrid energy E_{FF} with respect to the atomic coordinates.

The temperature of the system, which can be defined in terms of atomic velocities, is virtually raised to a certain level. This avoids the calculation of conformational space regions to be stopped at local minima. Then the system is gradually and very slowly cooled down in order that the total energy reaches a global minimum at which the topologically-constrained structure lies in its lowest energy conformation.

XPLOR is a software system implementing the restrained MDFF method for computing the 3D structure of biochemical macromolecules from nuclear magnetic resonance (NMR), crystallographic diffraction, or other experimental data [77]. This program was originally developed by Axel Brünger at Yale University. The program is highly versatile since the total energy function of the molecular system can be minimized by gradient descent algorithms, simulated annealing, and conformational search procedures.

XPLOR-NIH is an improved version of XPLOR incorporating new capabilities: additional NMR-specific features for refinement against NMR observables, generalized minimization, molecular dynamics in Cartesian coordinate and torsion angle space, effective treatment of rigid bodies, automatic NOE assignment,[2] and refinement against an ensemble of structures. The calculation of peptide self-assembled structures with XPLOR-NIH will be decribed in more details in Chapter 4.

[2] with Nuclear Overhauser Effect Spectroscopy - NOESY - an NMR technique for structure determination of macromolecular motifs

CHAPTER 3

Towards Induction of Chirality in Surface Assemblies

Relevant issues relating molecular chirality and chiral recognition in adsorption systems are addressed in this chapter. When molecules interact at a surface, they can sense their relative handedness, giving rise to specific patterns of chiral recognition. We show that it is possible to induce homochirality in surface assemblies of both sec-butyl and codeposited sec- and tert-butyl oligo-phenylene-ethynylene molecules by chiral amplification mechanisms. In the first case sec-butyl molecules adsorb on the Au(111) surface with the so called windmill and brickwall molecular patterns. For co-deposited molecules, the "sergeants-and-soldiers" principle can be applied. In this case, the sec-butyl moieties act as seeds to induce homochirality in co-deposited tert-butyl molecules.

3.1 Introduction

Supramolecular nanostructures formed by the self-assembly of chiral or prochiral molecules adsorbed at surfaces have been studied extensively in view of their unique properties and potential applications such as in enantioselective heterogeneous catalysis and nonlinear optics [78, 79]. In many cases, complex organic molecules generate a wide variety of chiral patterns upon surface confinement. In particular, several scenarios were developed to account for the self-assembly of a racemic mixture on a surface. On the one hand, chiral discrimination between mirror-image stereoisomers, can cause the spontaneous resolution of a racemic mixture into enantiopure domains. The idea that planar confinement can initiate enantioseparation of chiral molecules was first proposed by Stewart and Arnett [80]. STM studies have shown that both chiral and prochiral molecules adsorbed on surfaces can undergo spontaneous resolution into homo-chiral domains [39, 40, 81], molecular wires [52, 82], molecular rings [83], and nanoclusters [84]. On the other hand, racemate structures consisting of racemic [40, 85] or hetero-chiral domains [20] can be formed when both enantiomers co-assemble.

Many chiral biomolecules, such as amino acids and biologically relevant sugars, are predominantly found in one enantiomeric form. As a result the alternative form of enantiomer is inactive, and can be even toxic for living organisms. Therefore, the pharmaceutical needs require making effort forward separation of enantiomers of organic molecules [86]. At present, enantioselective chiral modifiers is exploited in asymmetric heterogeneous catalysis to promote single handedness of adsorbates, but there is only a few numbers of these compounds available today. Therefore, it is necessary to get more insight into the mechanisms which can lead to homochirality in molecular assemblies at surfaces.

3.1.1 Amplification of surface chirality

One way to control the chirality in supramolecular systems is chiral amplification. Two types of cooperative mechanisms for chirality amplification have been observed. These effects are referred to as “the sergeants-and-soldiers” principle and the “majority rule” principle [87–89]. The former arises when a small amount of homochiral molecules is mixed with a large amount of achiral ones. A few chiral units (the sergeants) control the helicity or handedness of a large number of achiral moieties (the soldiers) therefore promoting single chirality in the mixture [87, 90].

The “majority rule”, although similar regarding chirality amplification, operates via a quite different mechanism. Indeed, this effect occurs in mixtures of eniantiomeric forms of chiral molecules. A slight excess (or majority) of one of the enantiomers induces a disproportionately large preference toward the handedness (or helicity) of that enantiomer [91, 92]. These phenomena have been observed for covalent and noncovalent polymeric structures [93–95] and in the recognition of chiral amines or acids by hydrogen-bonded assemblies [96, 97].

The “sergeants-and-soldiers” principle was recently transferred to the 2D case on surfaces. It was shown that doping of an achiral monolayer (succinic acid, SU) with small amount of chiral dopant (tartaric acid, TA) is sufficient to induce global homochirality on the surface [98]. In short, the presence of the TA enantiomer suppresses com-

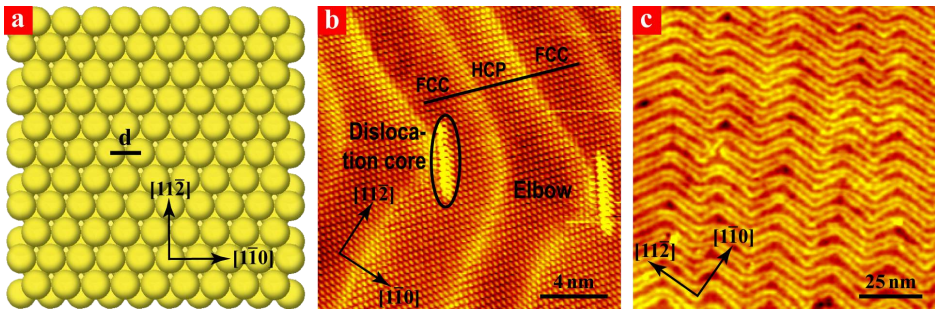

Figure 3.1: Au(111)-$(22 \times \sqrt{3})$. (a) Ball model of the 2 topmost (111) close-packed layers of an unreconstructed fcc crystal. (b) Atomic resolution of Au(111) (180×180 Å^2, $I_t = 1.13$ nA, $V_t = 88.5$ mV). (c) Herringbone reconstruction (1200×1200 Å^2, $I_t = 0.13$ nA, $V_t = 1.4$ V).

pletely the formation of one mirror domain in the SU lattice. Similarly, the "majority rule" was recently reported for heptahelicene [7]H on Cu(111) [99]. It was demonstrated that a small enantiomeric excess can cause amplification of chirality in 2D enantiomorphous lattice i.e., the entire molecular monolayer consists of domains of one mirror structure. Finally, a similar amplification effect can be achieved by the action of a magnetic field. This has been demonstrated for liquid crystal molecules which form single enantiomorphous lamellar structure on HOPG [100].

In the following, we discuss the possibility to induce homochirality in surface assemblies of both sec-butyl and codeposited sec- and tert-butyl oligophenylene-ethynylene molecules by chiral amplification mechanisms.

3.1.2 Au(111)- $\left(22 \times \sqrt{3}\right)$

A typical feature of some metal surfaces is that the topmost atoms adopt new equilibrium positions compared to a bulk truncated structure. This phenomenon is known as a *surface reconstruction*. Such a surface modification is inherent for all low-index faces of the fcc metals. However, gold is the only fcc metal that exhibits reconstruction of the closed-packed (111) surface at room temperature [101, 102]. This reconstruction can be rationalized in terms of the relief of the excess tensile surface stress present on the unreconstructed surface (Fig. 3.1a) [58].

Previous STM studies have demonstrated that the clean Au(111) surface exhibits unique $\left(22 \times \sqrt{3}\right)$ reconstruction where 23 topmost atoms lie over 22 bulk atoms. It implies a local 4.4% uniaxial contraction of the surface layer in a $\langle 1\bar{1}0 \rangle$ direction. Due to this directional compression, the registry of surface gold atoms alternates between hollow sites of the fcc and hcp stacking order. In turn, the gradual transition between fcc and hcp regions, known as the *discommensuration lines*, consist of atoms sitting on the bridge sites [103]. It results in a small vertical modulation of 0.2 Å in the form of bright double rows running along the $\langle 11\bar{2} \rangle$ direction as depicted in Fig. 3.1b. The distance between neighbouring double rows (fcc region) is about 63 Å; and within double lines (hcp region) is equals to 44 Å. Consequently, fcc surface stacking is energetically more favourable than hcp stacking, since fcc regions are broader than hcp regions [58]. As

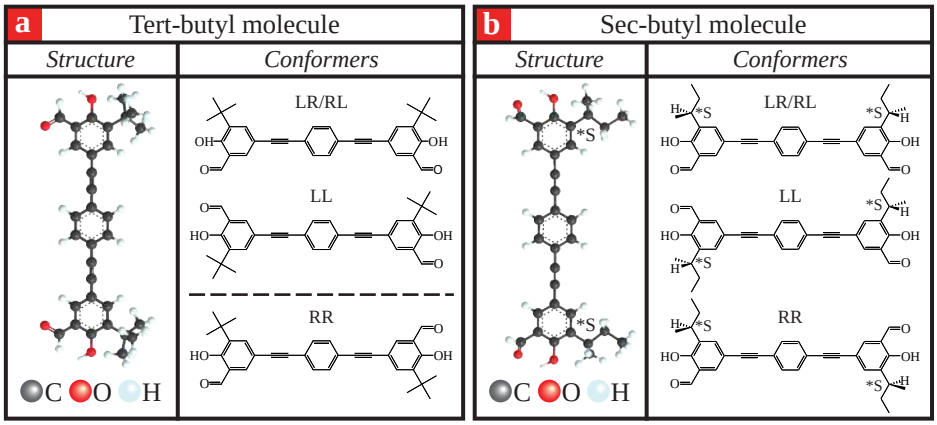

Figure 3.2: Structure and surface conformers of (a) the *tert*-butyl and (b) the *(S)-sec*-butyl molecules. The dashed line and * indicate a mirror plane and a chiral center, respectively.

shown in Fig. 3.1c the 3-fold symmetry of Au(111) results in three possible 120°-rotated to each other domains forming the well-known zigzag or *herringbone reconstruction pattern*. An extensive inspection of this zigzag structure reveals that in the vicinity of the bending points, known as "elbows", the discommensuration lines are characteristically deformed due to a surface dislocation. The distance between neighbouring atoms on the unreconstructed Au(111) surface is $d = 2.88$ Å.

3.1.3 The molecular systems

The results presented here are built on previous work performed in our laboratory, which was devoted to the study of two-spoke molecules from the oligo-phenylenes-ethynylenes family [18]. These prochiral compounds can adsorb both as chiral and achiral surface conformers and form chiral surface assemblies as outlined below.

The achiral *tert*-butyl molecules

The linear, π-conjugated backbone of *tert*-butyl molecules is built up from three benzene rings coupled by ethynylene spokes, and is additionally functionalized at both ends with an aldehyde, a hydroxyl, a *tert*-butyl group as depicted in Fig. 3.2a. The *tert*-butyl group consists of three methyl groups, CH_3, attached to a carbon atom, and molecule is therefore achiral. In gas phase the molecular rotation around the ethynylene spokes is facile, while the molecules adsorbed with the π-system parallel to the surface partially loose this ability. Consequently, the adsorbates confinement by the substrate enables these molecules to assume three different surface conformers, which can be distinguished by the position of the *tert*-butyl group on the right (R) or left (L) side of the molecular backbone when viewed from the centre of the molecule and towards the end of the spoke. As a result it is possible to discriminate between the achiral (LR/RL) surface conformers that are superimposable by rotation and translation in the plane of the substrate, and the two chiral (LL and RR) ones which do not contain a mirror plane (see Fig. 3.2a).

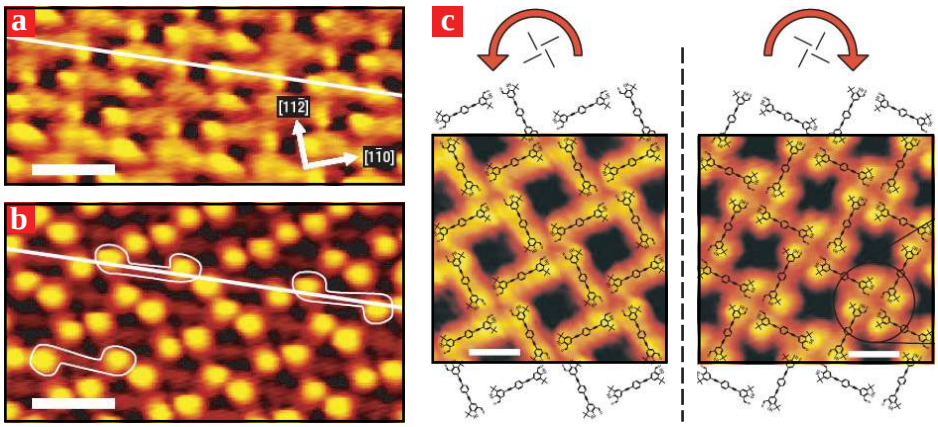

Figure 3.3: Supramolecular structures formed by the *tert*-butyl molecules. STM images of the brick-wall structures obtained in (a) the π-system imaging mode, and (b) the *tert*-butyl imaging mode. (c) STM images with schematic models of the windmill structure showing two domains of opposite chirality.

Two principally different imaging modes can be distinguished by means of STM. The most frequently encountered imaging mode is presented mainly by clearly paired protrusions. These bright features can be attributed to the *tert*-butyl groups at the ends of the achiral molecules. The mere fact that these protrusions are positioned off-axis with respect to the backbone allows determining the molecular conformation. Furthermore, a spontaneous change of tip conditions can entail an alternative imaging mode. In this instance the image contrast is caused mainly by the conjugated π-system of the molecule. Only the molecular backbone built up from the benzene rings is imaged in this mode.

As revealed by STM, the *tert*-butyl molecules deposited onto an atomically clean Au(111) surface self-assemble into two coexisting ordered adsorption phases referred to in the following as the brick-wall and windmill structures. In the phase shown in Fig. 3.3a, the neighbouring molecules form parallel rows by head-to-head interaction, that are shifted relative to each other by half the repeat distance along the rows like in a brick-wall stacking. In this particular case, the structure comprises all three molecular conformers (see Fig. 3.3b), which are adsorbed with their backbone parallel to the substrate. Moreover, the bright protrusions ascribed to the *tert*-butyl groups spontaneously flip from one side of the molecular backbones to the other, as it can be noticed from time-lapse sequences of STM images. This dynamical phenomenon is accounted for by the rotation of the functionalized benzene ring around the axis of the ethynylene spoke. Thus, these molecules are not completely stereochemically fixed by the substrate, and consequently can switch between different surface configurations, i.e. chiral (RR/LL) and achiral (RL/LR) conformers, or even between two chiral enantiomers by a rotation of one or both endgroups, respectively. Adjacent molecules in the rows adopt either a *cis*-configuration, where their *tert*-butyl groups line up at the same side of the molecular row, or a *trans*-configuration, where the *tert*-butyl groups are at opposite sides (see

Fig. 3.3b).

The prevailing motif exhibited by this *para*-compound is a configuration in which four molecules form a windmill figure with their backbone meeting at a common central node as shown in Fig. 3.3c. Each molecule connects two adjacent nodes, producing an ordered tiling pattern with square openings delimited by four molecules. Since the windmill motif was found on the surface in two mirror-image forms with opposite rotations (Fig. 3.3c), the extended molecular islands present a chiral tiling structure. In this structure the *tert*-butyl groups are located at the side of the molecular backbone pointing away from the central node. This means that each chiral form of the tiling pattern is generated by only one of the two possible surface conformers, either RR or LL. Consequently, the chirality of the tiling pattern is correlated with the chirality of the surface conformers, and results in *globally heterochiral* surface. Interestingly, an achiral RL conformer occasionally attached to the edge of a homochiral domain consisting of RR conformers undergoes a conformational change to the chiral RR conformer through thermal activation, in order to fit into the host structure. Such switching between enantiomeric forms can induce chiral ordering on surface, termed *chiral accommodation*, and is a promising route towards formation of extended *homochiral surface* domains.

The chiral *sec*-butyl molecules

The key idea sustaining the present investigation was to modify very slightly the *tert*-butyl molecules by replacing a *tert*-butyl substituent with a group containing a stereogenic centre making the compound chiral. It may thus be hoped that the intermolecular interaction already evidenced for *tert*-butyl molecules will be preserved in novel compounds enabling them to create the same supramolecular patterns on the surface. On the other hand, this slight change was carried out with the hope that one chiral molecular surface conformer (RR or LL) will dominate over the other leading to preferential surface homochirality.

The novel molecules investigated in the present work differ from the previous ones by the substitution of *tert*-butyl groups by *sec*-butyl groups containing a chiral centre C^* atom (Fig. 3.2b). This chiral centre is of the *(S)*-type according to the Chan Ingold Prelog priority rules based on molar mass.[1] Due to the chiral centre *(S)* present in the *sec*-butyl group, these molecules are chiral in gas phase, in contrast to the *tert*-butyl ones which are achiral. Like for *tert*-butyl molecules, the *sec*-butyl ones possess three molecular conformers on surfaces depending on whether the *(S)-sec*-butyl groups is positioned to the left (L) or to the right (R) with respect to the molecular backbone. The presence of *sec*-butyl groups with chiral centre may introduce energy difference between L and R surface conformers as will be detailed in section 3.2.4.

3.2 STM of *sec*-butyl molecules

The enantiopure *(S)-sec*-butyl molecules were sublimated from a glass crucible resistively heated to a temperature of 378 K. The deposition was carried out in UHV chamber (base pressure in the low 10^{-10} mbar region) onto an atomically clean Au(111) substrate

[1] If the centre C^* is oriented so that the lowest-priority, H, of the four groups is pointed away from a viewer, the viewer will then see that the priority of the remaining three substituents (phenylene , $-CH_2CH_3$, $-CH_3$ groups) decreases in counterclockwise direction.

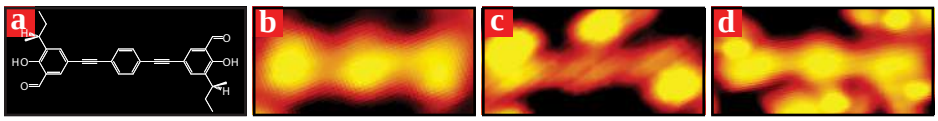

Figure 3.4: STM imaging modes for the *(S)-sec*-butyl molecules.(a) Stick model of the molecular species. RR molecular surface conformer is chosen to approximate the accompanying STM images.(b) π-system mode revealing the molecular backbone. (c) *Sec*-butyl mode characterized by prominent *(S)-sec*-butyl groups. (d) Simultaneous imaging of the *(S)-sec*-butyl groups and the conjugated π-system.

held at RT. The Au(111) single-crystal has been cleaned by repeated cycles of Ar^+ ion sputtering at 1.5 keV for 20 min followed by sample annealing at 850 K for 10 min until herringbone reconstruction was clearly visible. Further stabilization of the molecular structures was achieved by sample cooling to 120 K in the main manipulator. The molecular structures on the Au(111) substrate were studied with STM in the temperature range 120-140 K.

High resolution images of the individual *(S)-sec*-butyl molecules are given in Fig. 3.4. By comparing Fig. 3.4b,c with the previous study of Weigelt et al. [18], it is apparent that the prominent features of these imaging modes are similar for the original *para*-compound and its derivative. Interestingly, the chiral molecules can additionally present simultaneous imaging of the *(S)-sec*-butyl groups and the conjugated π-system as illustrated in Fig. 3.4d.

As shown in Fig. 3.5a,b, the *(S)-sec*-butyl molecules sublimated onto the inert Au(111) surface dominantly form two coexisting highly ordered adsorption structures, which are very similar the brick-wall and windmill structures observed for *tert*-butyl molecules. Additionally, hetero-chiral domains (see Fig. 3.5c) are also observed but seldom in proportion to other structures. All these structures are built from molecules adsorbed with their π-system parallel to the surface. Moreover, the molecular adsorption does not affect the herringbone reconstruction of the Au(111)-$(22 \times \sqrt{3})$ surface. This conclusion

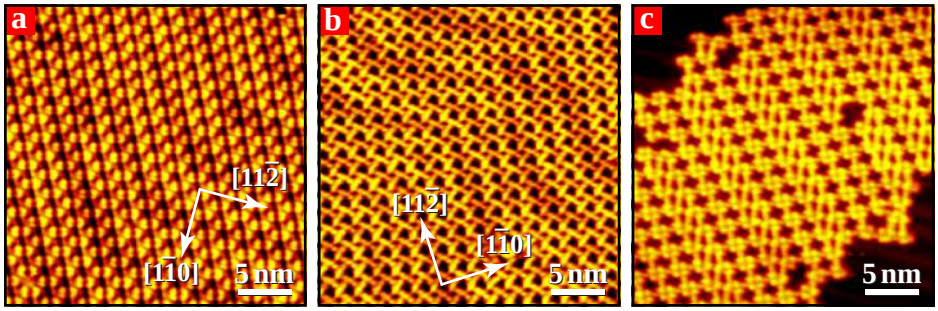

Figure 3.5: Coexisting monolayer molecular islands formed from *(S)-sec*-butyl molecules: (a) brick-wall (390×390 Å^2, $I_t = 0.51$ nA, $V_t = 1.04$ V), (b) grid-like (390×390 Å^2, $I_t = 0.59$ nA, $V_t = 1.0$ V), and (c) hetero-chiral (390×390 Å^2, $I_t = 0.43$ nA, $V_t = 1.81$ V) structures.

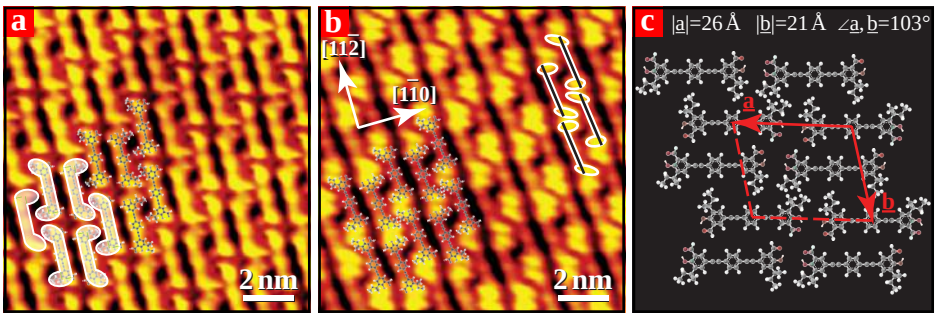

Figure 3.6: The brick-wall structure formed by the *(S)-sec*-butyl molecules. (a) STM image obtained in the π-system imaging mode (120×120 Å^2, $I_t = 0.45$ nA, $V_t = 1.28$ V). (b) STM image in the *sec*-butyl imaging mode (120×120 Å^2, $I_t = 0.45$ nA, $V_t = 1.04$ V). (c) Schematic model of the brick-wall adsorption structure deduced from the STM image.

is confirmed by the presence of a characteristic corrugation of the reconstructed Au(111) surface underneath the adsorbed molecular overlayers, as revealed by Fig. 3.5a,b. Thus, the *(S)-sec*-butyl molecules relatively weakly coupled to the Au(111) substrate. The next sections are concerned with a detailed description of the *sec*-butyl tiling patterns compared to *tert*-butyl ones. In addition, a statistical analysis of domains consisting of different conformers is carried out.

3.2.1 Brick-wall structure

Typical high resolution images of the brick-wall structure are shown in Fig. 3.6. The STM image obtained in the π-system imaging mode (see Fig. 3.6a) reveals that the *(S)-sec*-butyl molecules self-assemble into a regular tiling pattern with molecular backbones aligned parallel to each other. Moreover, the neighbouring molecules form parallel rows by head-to-head interaction. The *sec*-butyl imaging mode (see Fig. 3.6b) allows determining the molecular surface conformers within rows, which is visualized by STM as a protrusion pair separated by a line of lower brightness level. Thus, the bright protrusions imaged next to each other belong to adjacent molecules encountering in a head-to-head fashion. These neighbouring protrusions assume a cis-configuration, i.e. *(S)-sec*-butyl groups on adjacent molecules are at the same side of the line connecting two molecules. The features described above indicate that the rows entirely consist of molecules in the LR/RL conformation, compared to *tert*-butyl molecules which exhibit all three conformers equally distributed. Additionally, the backbones of the *(S)-sec*-butyl molecules in the row do not align into a straight line (see Fig. 3.6b) compared to the case of the tert-butyl molecules in the corresponding brick-wall structure. The slight shift between adjacent molecular backbone within rows can be accounted for by (i) maximization of H bonding between the aldehyde and hydroxyl groups of neighbouring molecules; (ii) intermolecular steric hindrance with overlap minimization of adjacent bulky *(S)-sec*-butyl groups.

The STM images also reveal an ordering interaction between molecular rows. The molecules form double rows by side-to-side intermolecular interaction with *sec*-butyl

groups pointing towards the interior of row pairs, where individual molecular rows are shifted with respect to each other by half the repeat distance along the row. Furthermore, *neighbouring double rows* are displaced relative to each other by a small amount. In the case of the *tert*-butyl molecules, *all rows* are slipped relative to each other by half the repeat distance forming a structure completely identical to a brick-wall stacking. Additionally, the *(S)-sec*-butyl groups of the truly chiral molecules in adjacent rows are oriented only in the opposite directions, in contrast to the prochiral molecules where the *tert*-butyl groups preferentially point to the same direction. From the overall description above it follows that the brick-wall structure of *(S)-sec*-butyl molecules exhibits complete conformational order which may result from the presence of chiral centers.

3.2.2 Windmill structure

The second tiling pattern formed by the *sec*-butyl molecules is the windmill open structure (see Fig. 3.7). The pattern is similar to that exhibited by *tert*-butyl molecules, i.e. this motif is built by four molecules joined at a common node in a windmill configuration. It is also possible to define the basic unit of the tiling motif as a regular rhomb formed by the backbones of four molecules delineating an opening as depicted in Fig. 3.7a,b. This tiling pattern with rhombic shape is slightly different from the square openings of the *tert*-butyl windmill motif. Structural stabilization of such open structure is most likely provided by intermolecular hydrogen bondings which can occur between hydroxyl and aldehyde groups of neighbouring molecules sharing the same node as follows from model in Fig. 3.7e,f. The presence of periodic openings in the windmill structure reduces the molecular packing density with respect to that of the brickwall network.

An important point is that the windmill pattern occurs with two opposite rotational directions, and consists entirely of one of the two chiral surface conformers. Domains with a counter-clockwise rotating windmill motif are built exclusively from RR conformers (Fig. 3.7c), while domains with a clockwise rotating windmill motif are built from LL conformers (Fig. 3.7d). Thus, the RR/LL conformers of *(S)-sec*-butyl molecules self-assemble into enantiopure mirror domains with opposite sense of rotation. Molecules are highlighted in different colors in Fig. 3.7a,b, to underscore the different bulky group surface confinement in the presented models which will be discussed in the following.

3.2.3 Statistical analysis

As outlined in a previous study [18], LL/RR conformers of *tert*-butyl molecules can self-assemble into conformationally enantiopure domains with opposite chirality, such as clockwise/anticlockwise rotating windmill motifs, with *equal probability*. From high resolution STM images shown above, *(S)-sec*-butyl molecules form patterns structurally similar to those of tert-butyl molecules. However, the statistical distribution of adsorption structures formed by sec-butyl molecules might show some differences. The chiral centers in the *(S)-sec*-butyl moieties should introduce an asymmetry in the occurrence probability of the molecular conformers, which may favor the formation of one pattern to the detriment of the other. To verify this hypothesis, a careful statistical analysis was carried out.

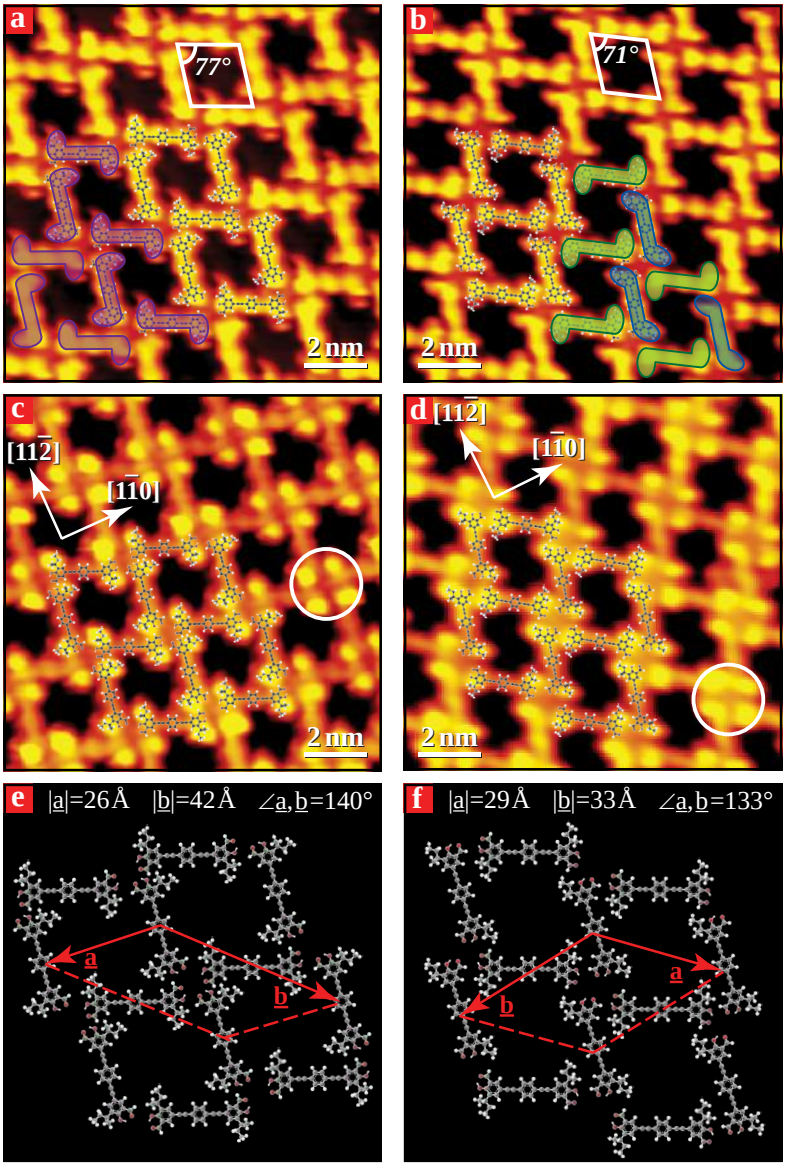

Figure 3.7: The windmill structure formed by RR (a,c,e) and LL (b,d,f) conformers of the *(S)-sec*-butyl molecules. (a,b) STM images obtained in the π-system imaging mode for RR (120×120 Å^2, $I_t = 0.5$ nA, $V_t = 1.28$ V) and LL (120×120 Å^2, $I_t = 0.5$ nA, $V_t = 1.24$ V). (c,d) STM images in the *sec*-butyl imaging mode for RR (120×120 Å^2, $I_t = 0.42$ nA, $V_t = 1.1$ V) and LL (120×120 Å^2, $I_t = 0.45$ nA, $V_t = 1.04$ V. (e,f) Schematic models of the windmill adsorption structures deduced from the STM images for RR and LL.

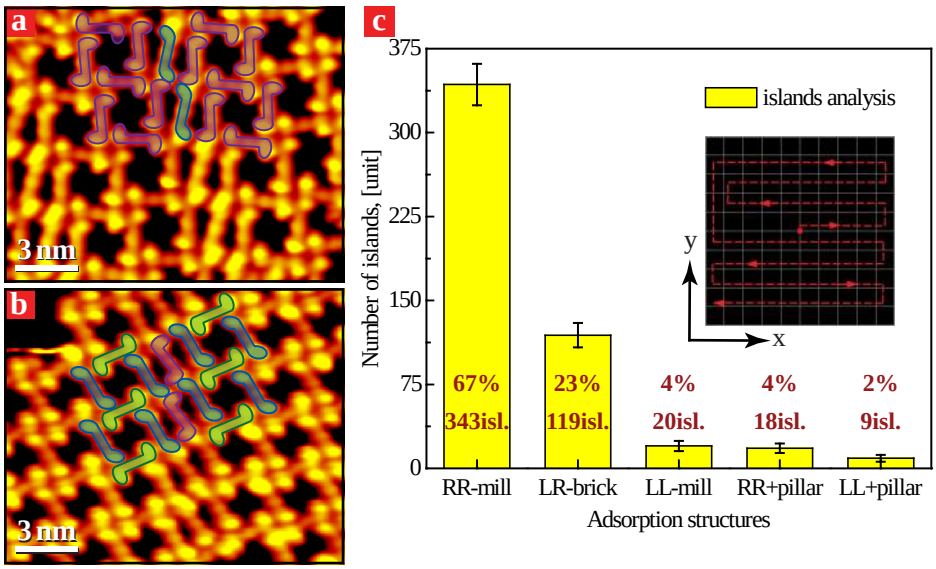

Figure 3.8: (a) The grid-like structure formed by LL conformers of the *(S)-sec*-butyl molecules. (b) The hetero-chiral structure consisting of alternate windmill (violet) and "pillar" (green) tiling patterns built from RR and LL conformers, respectively. (c) Statistical analysis of the different structures on the surface carried out by counting the islands with different conformational types of molecules.

The size of the samples investigated in this work was about 8×8 mm^2. When the STM tip was brought into close proximity of the surface a sample area of 2000×2000 nm^2 could be scanned by moving the tip across this window. The tip was placed in the middle of the selected sample area and rastered across the surface to explore systematically the whole sample area as shown by the red line in Fig. 3.8c, inset. The encountered islands presenting different molecular motifs were carefully counted along this path. After this sample area was entirely scanned this way, the tip was retracted from the surface and the sample was moved to another position corresponding to another spot of 2000×2000 nm^2. This operating procedure was carried out for several identical preparations of samples by keeping exactly the same experimental conditions over several days, ensuring reliable statistical analysis of the collected data.

A statistical analysis concerning the occurrence of the adsorbed structures on the surface is summarized in Fig. 3.8c. In this histogram, the bar height is proportional to the number of islands presenting a specific structure. The island size is not considered when counting the island number for each structure. Since RR islands are larger than LL ones this counting somewhat underestimates conformer excess.

As can be seen from Fig. 3.8c the formation of the two windmill phases with different sense of rotation is not equally probable for truly chiral *(S)-sec*-butyl molecules. The most frequent structure is the anticlockwise rotating windmill motif consisting solely of RR conformers. This structure represents the largest population in the STM images in

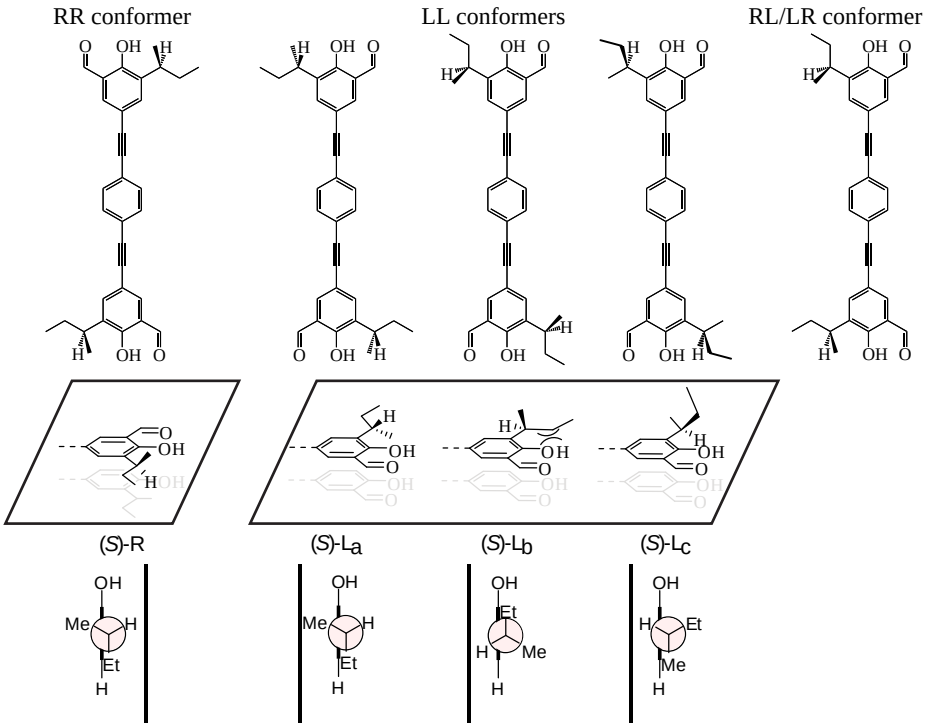

Figure 3.9: Bulky group conformations for *sec*-butyl surface conformers.

a proportion of 67% while the probability to find the pattern displaying the clockwise rotating windmill motif of LL conformers is only 4%. Therefore, the *(S)-sec*-butyl molecules show a strong preference for one of the two conformers in contrast achiral *tert*-butyl species. The second largest population with a probability of 23% is the non-chiral brickwall structure. The other patterns (see Fig. 3.8a,b) consist of alternate windmill and "pillar" tiling structures built from opposite conformers, namely "RRmill+LLpillar" and "LLmill+RRpillar", and account for only 4% and 2% of the islands, respectively.

3.2.4 Bulky group conformations

Origin for the preference of the RR surface conformer over the LL one must be sought in the intrinsic chirality of *(S)-sec*-butyl molecules. By flipping the *(S)-sec*-butyl group from R to L conformation an identical geometry cannot be reproduced; therefore, some difference in energy between the *(S)-sec*-butyl R and L adsorption geometries has to be expected (see Fig 3.9, top panel).

The models shown in Fig. 3.9 report possible geometries for *(S)-sec*-butyl bulky group in RR, LL and RL/LR surface conformers. We restricted the infinite number of possible bulky group conformations to those presenting, in particular, the ethyl chain lying entirely on the surface. In this way, the adsorbed molecule will maximize the stabilizing interaction with the surface. In the RR surface conformer the bulky group is

assumed to adopt only one conformation, denoted as (*S*)-R in Fig. 3.9, where the H atom points towards the surface. This conformation will minimize steric hindrance between the ethyl chain and the hydroxyl group.

The LL conformer leaves more possibilities open: in the first one, the methyl group is pointing towards the surface (denoted as (*S*)- L_a); in the second one, the H is pointing towards the surface ((*S*)- L_b), implying a higher steric hindrance between the ethyl chain and the hydroxy group; in the third one, methyl and H are pointing to the surface while the ethyl is oriented in the opposite direction ((*S*)- L_c). The last option would minimize intramolecular steric hindrance, however, at the price of less stable adsorption geometry. In the case of RL/LR conformers, the two *(S)-sec*-butyl groups belonging to the same molecule are supposed to interact with the surface via the H atom. This condition is satisfied when the bulky groups in R conformation keep the ethyl chain perpendicular to the molecular backbone; and when the other bulky group in L conformation has been rotated 180 degrees around the C−C bond connecting it to the benzene ring, or vice versa (see RL/LR model in Fig. 3.9).

Evidences of the presence of different bulky group conformations are found in the high resolution STM images previously presented. The assignment of bulky group conformation is justified by differences in orientations of bright protrusions observed in STM images. The bulky group conformation is assumed to be (*S*)-R for all molecules in the RR windmill phase shown in Fig. 3.7a,c, which are therefore depicted with the same color (violet). Molecules marked in violet in this STM image have bright protrusions aligned perpendicular to the molecular backbone which is consistent with ethyl group orientation of the *(S)*-R model. By contrast, the LL windmill structure shown in Fig. 3.7b,d is built from molecules with two different bulky group conformations marked by blue and green colors.

The first conformation (green) is expected to be (*S*)- L_a with the methyl group pointing towards the surface and the ethyl group perpendicular to the molecular backbone. In the other conformation (blue) one can suggest that the H atom is pointing towards the surface while the ethyl group is oriented outwards from the molecular backbone, in agreement with a (*S*)- L_b bulky group geometry. A closer look at the molecules marked by green and blue colors in Fig. 3.7b,d shows that the bright protrusions are aligned either perpendicular to or outwards from the molecular backbone in agreement with the orientation of ethyl groups in the proposed models.

Additionally, the *sec*-butyl groups within a single molecule of the brick-wall structure are imaged asymmetrically with respect to the molecular backbone (see Fig. 3.6b). One of the protrusions is clearly pointing orthogonally to the molecular backbone, while the other one is slanted. These observations correspond to the ethyl orientation in the RL conformer described in the model above.

3.2.5 Other windmill structures

A few minority phases not observed for the *tert*-butyl compounds were identified for the novel *sec*-butyl molecules.

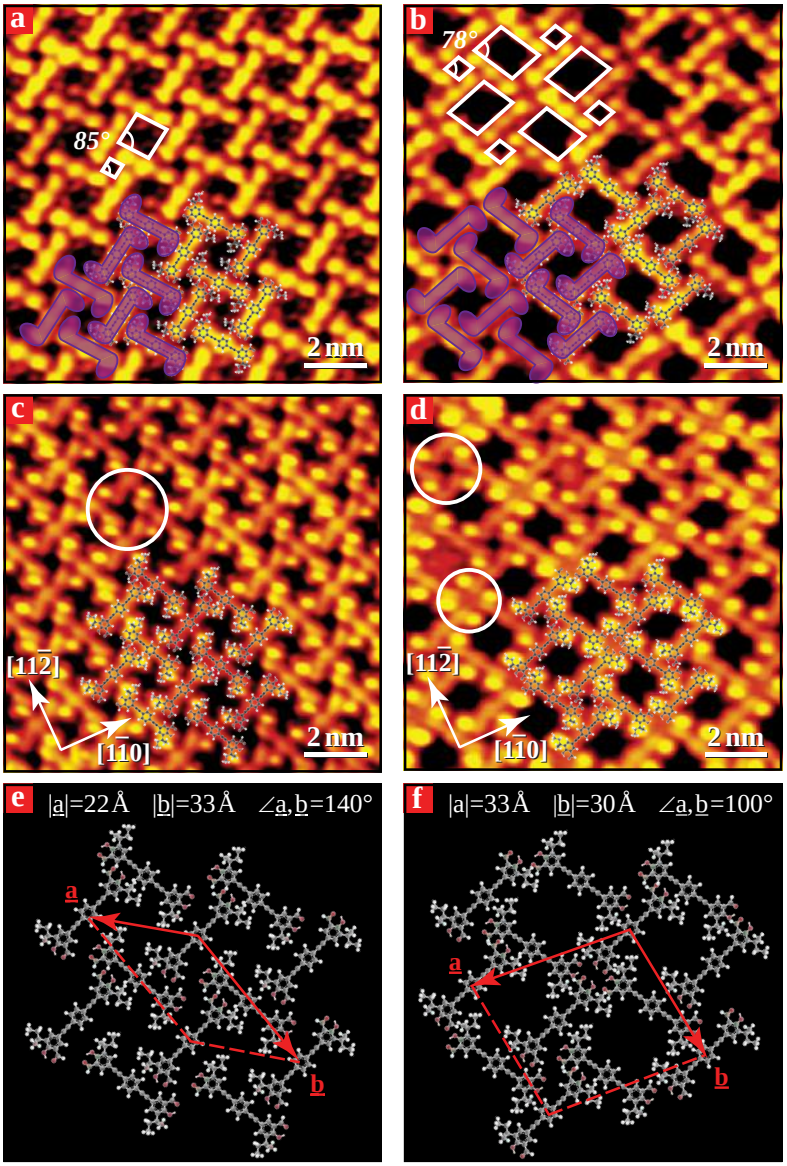

Figure 3.10: The cross-like (left) and complex (right) patterns formed by the (*S*)-*sec*-butyl molecules. (a,b) STM images obtained in the π-system imaging mode for cross-like (120×120 Å^2, $I_t = 0.45$ nA, $V_t = 1.2$ V) and complex structures (120×120 Å^2, $I_t = 0.4$ nA, $V_t = 1.54$ V). (c,d) STM images in the *sec*-butyl imaging mode for cross-like (120×120 Å^2, $I_t = 0.56$ nA, $V_t = 1.32$ V) and complex patterns (120×120 Å^2, $I_t = 0.45$ nA, $V_t = 1.54$ V. (e,f) Schematic models of the corresponding adsorption structures deduced from the STM images.

Crosslike pattern.

In the structure shown in Fig. 3.10a,c mutually skew-orthogonal molecules form an extended crosslike network which is similar to the windmill structure described above. In this novel molecular arrangement, the crosslike pattern exhibits the two senses of rotation, even if this character is less pronounced compared to the windmill one. Here, a high packing density is achieved by intermolecular slipping such that all *(S)-sec*-butyl groups are positioned close to the central benzene rings of the neighbouring orthogonal molecules (see Fig. 3.10c,e). As a result, the backbones of the molecules form two rhombic-shaped openings of large and small size clearly depicted in Fig. 3.10a, which are however smaller than that of the windmill pattern.

The crosslike pattern also resembles to some extend the windmill structure due to the fact that the *(S)-sec*-butyl groups are always pointed inward the core of the largest rhombic openings. Besides, the *(S)-sec*-butyl molecules self-assemble into enantiopure domains consisting of either RR or LL conformers leading to a counter-clockwise, or a clockwise rotating motif, respectively. It follows that this structure exhibits a complete order as regards both organizational and conformational chirality. All molecules have the same *(S)*-R conformation indicated in violet color.

Complex pattern.

The last molecular structure presented in Fig. 3.10b,d generates a complex pattern combining both windmill and crosslike motifs. As seen from the *sec*-butyl imaging mode in Fig. 3.10d,f the molecules self-assemble in such a way that the headgroups from one side of the molecules interact with neighbouring molecules sharing the same node, while the headgroups from the opposite side are shifted towards the central benzene ring of the neighbouring skew-orthogonal molecules. Thus, each molecule connects adjacent windmill and crosslike motifs constructing an extended highly ordered network with two types of openings that are large oblique-shaped and contiguous smaller rhombic-shaped "hollow" sites (see Fig. 3.10b).In spite of the complexity of this pattern, this structure is also chiral since enantiopure domains consisting of either RR or LL conformers are found on the Au(111) substrate. Windmill, crosslike, and complex patterns were counted together for statistical analysis of islands with either RR or LL conformers.

3.3 STM study of co-deposited *sec*-butyl and *tert*-butyl molecules

In the previous section it was established that the chiral *(S)-sec*-butyl molecules can self-assemble into windmill and brick-wall structures on Au(111) surface. Statistical analysis revealed that the RR-windmill motif significantly predominates over both LL-windmill and RL-brickwall molecular structures. The drastic asymmetry in the statistical occurrence of the two *(S)-sec*-butyl surface enantiomers (RR and LL) can be used to induce homochirality in self-assembly of initially achiral *tert*-butyl molecules. This strategy can be achieved by implementing the "sergeants-and-soldiers" approach to these molecular systems. Therefore, this project will concern the coadsorption of *sec*- and *tert*-butyl molecules on the Au(111) substrate under different deposition conditions with the objective to demonstrate amplification of surface homochirality by "seeding" the achiral *ter*t-butyl moities with the chiral *sec*-butyl ones. Two separate protocols were used to

look for the influence of chiral *sec*-butyl molecules on patterns formed by *tert*-butyl molecules on the metal surface.

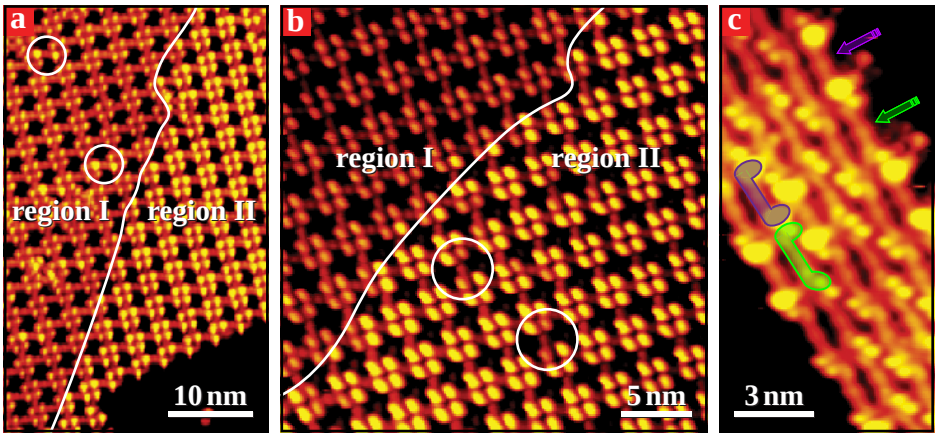

Figure 3.11: Supramolecular structures formed by codeposition of *ter*t-butyl molecules after the growth of *sec*-butyl molecular islands. (a) Molecular island showing grid-like structure where *tert*-butyl molecules (higher brightness) accommodate to *sec*-butyl molecules (lower brightness). (b) Zoom-in into the seamless boundary between *sec*- and *tert*-butyl regions as indicated by the line. (c) Brick-wall structure consisting mainly of *sec*-butyl molecules (green) with a few *tert*-butyl molecules (violet) well-identified by protrusion pairs of the highest brightness.

3.3.1 "Nucleation" approach

The initial experiment concerning the self-assembly of this bimolecular system can be coined as the "nucleation approach". This protocol consists in the formation of ordered *sec*-butyl islands on the gold surface acting as nuclei for the subsequent growth of homochiral *tert*-butyl ordered islands via a chiral accommodation process and without disruption of the initial ordered structure.

The experimental procedure was carried out in several steps:

- Dosing *sec*-butyl molecules on the Au(111) surface held at RT;
- Cooling down the sample to 200K at rate of 6K/min;
- Dosing the *tert*-butyl moities followed by sample annealing at 200K for 30 min;
- Cooling down the sample to 115K at rate of 6K/min.

Fig. 3.11a shows an STM image of a windmill structure obtained after codeposition. One can clearly distinguish in this island two regions of different brightness which might be composed of two kinds of molecules. A close up view at the boundary between these two regions (see Fig. 3.11b) reveals that the brighter molecules decorate the edge of the dimmer molecular island and accommodate a windmill pattern of the same chirality. It is striking that the geometry and interaction between the two different molecules are

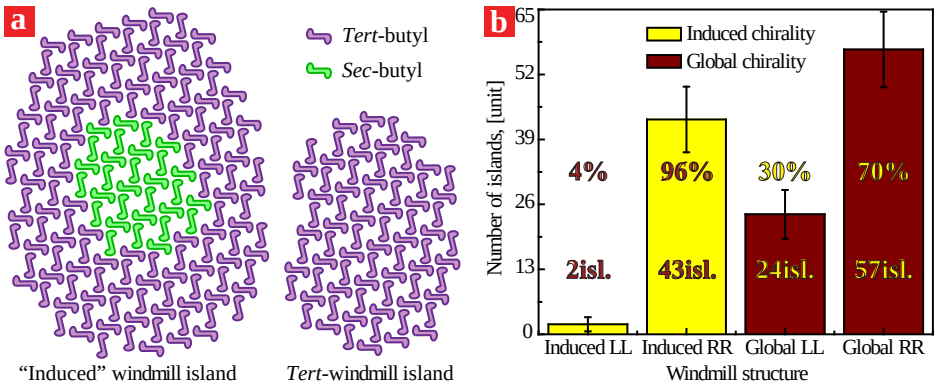

Figure 3.12: (a) Scheme of the "nucleation" process during codeposition.(b) Statistical distribution of patterns formed by co-deposited *sec*- and *tert*-butyl molecules.

similar enough that they can form this type of seamless phase boundary. Since *sec*-butyl and *tert*-butyl molecules are commensurate single molecular species can be even embedded in a domain formed by the other one as highlighted by circles in Fig. 3.11a,b.

To ascertain the nature of the two molecular species a careful analysis of additional structures is necessary. As shown in Fig. 3.11c, a few islands adopt the brick-wall pattern by co-assembling molecules of low and high brightness. One can notice that the orientations of protrusions in dimmer molecules (green) forming the RL-brickwall phase are identical to those previously observed for the analogous structure of *sec*-butyl molecules. It is thus reasonable to assign the lower- (green) and higher-contrast (violet) features to *sec*-butyl and *tert*-butyl molecules, respectively. The difference in contrast imaging may arise from a higher elevation of *tert*-butyl groups above the surface.

Statistical analysis

A statistical survey should be performed in order to verify that the asymmetry in the formation of clockwise and anticlockwise windmill patterns by *sec*-butyl molecules has been transferred to *tert*-butyl ones. The statistics of induced chirality in such islands is presented by the histogram in Fig. 3.12b (yellow bars). The same counting procedure as for the *sec*-butyl self-assembly study was used. However, the sampling criteria exclude islands that did not show a clear boundary between a *sec*-butyl nucleus and a surrounding *tert*-butyl domain.

This analysis shows that the RR-windmill pattern is preferentially formed (96%) and that the LL-windmill pattern is a minority phase (4%). Additionally, islands consisting solely of pure *tert*-butyl molecules were found on the surface (see Fig. 3.12a). Therefore, the global chirality should be estimated. In this case, *tert*-butyl molecular islands are counted together with islands presenting both *tert*- and *sec*-butyl molecular domains separated by seamless phase boundaries. In other words, the brown bars in Fig. 3.12a sum out the two islands species. A clear-cut predominance of RR conformers (70%)

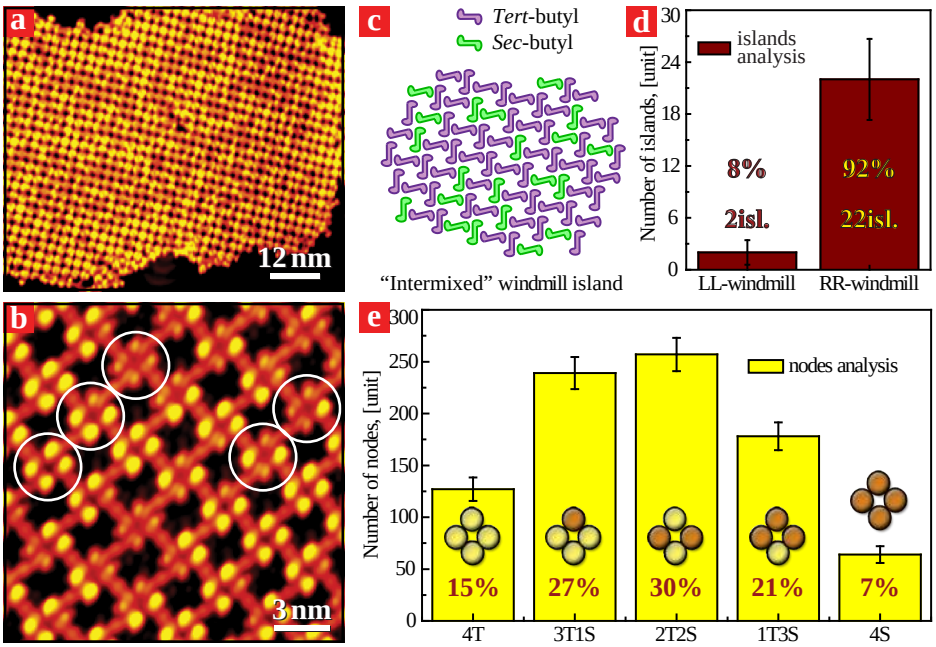

Figure 3.13: "Intermixing" approach.(a) Large scale STM image of intermixed windmill structure. (b) Zoom-in into this island presenting all possible combination of nodes.(c) Sketch showing an "intermixed" island. (d) Statistical analysis of LL or RR windmill structures and (e) different types of nodes.

over LL ones (30%) is found.

3.3.2 "Intermixing" approach

To avoid the formation of extended ordered domains composed only of *tert*-butyl molecules, a second protocol, denoted as the "intermixing" approach, was implemented. In contrast to the previous preparation procedure, the molecular species are dosed sequentially on the Au(111) substrate held at RT, followed by sample annealing at 320 K for 30 min. Finally, the sample was cooled down to 115K at rate of 6K/min.

This codeposition protocol favors exclusive formation of intermixed islands preserving RR and LL chiral windmill patterns. Pristine islands of either *sec*- or *tert*-butyl molecules were not observed while the RL-brickwall structure was present in negligible amount. A typical island with an obvious intermixed structure is shown in Fig. 3.13a,b. This island is made of 1073 *tert*- and 790 *sec*-butyl molecules accounting for 58% and 42% of the total number, respectively.

Statistical analysis

As for the previous experiments, a statistical analysis of "intermixed" domains was performed (see Fig. 3.13c,d). It shows that the RR windmill motif overwhelms the LL one in proportion of 92% against 8%. This large disparity demonstrates clearly that in the

case of intermixed phases *sec*-butyl molecules are able to amplify homochirality in the self-assembly of achiral *tert*-butyl moieties. Here, the homochiral induction effect is enhanced by the absence of pure *tert*-butyl molecular islands.

The intermixed nature of this self-assembly can be firmly established by 5 types of nodes which are clearly identified in the windmill pattern (Fig. 3.13b). The nodes are formed either by 4 *sec*-butyl and 4 *tert*-butyl molecules (4S, 4T), or by the intermixed molecular combinations 3S1T, 3T1S and 2S2T in the proportions depicted in Fig. 3.13e. The nodes 2S2T, 3T1S, and 3S1T are found to be the most abundant varieties (respectively 30%, 28%, and 21%), indicating that this experimental approach promotes global intermixing of the coexisting phases in this self-assembly.

3.4 Conclusion

STM studies of *sec*-butyl molecules deposited on Au(111) surface evidence highly ordered brickwall and windmill molecular patterns. Statistical analysis of the observed self-assemblies reveals a predominance of the RR-windmill pattern (67%) over the LR-brickwall (23%) and the LL-windmill (4%) structures due to the presence of chiral centers in *sec*-butyl molecules.

The second part of this study was devoted to the co-adsorption of *sec*- and *tert*-butyl molecules using "nucleation" and "intermixing" approaches. In both experimental protocols, amplification of surface homochirality was successfully achieved by seeding achiral *tert*-butyl molecules with chiral S-*sec*-butyl ones. The phenomenon responsible for chiral amplification resembles strongly the "sergeants-and-soldiers" effect with the difference that a higher concentration of "sergeants" (*sec*-butyl moieties) was necessary to induce homochirality in the "soldiers" (*ter*t-butyl moieties). In the first codeposition process, the induction is significantly favored by the formation of seamless boundaries between *sec*-butyl nucleation islands and *tert*-butyl domains which facilitate the propagation of *sec*-butyl chiral conformation to *tert*-butyl domains. In the second protocol, *sec*-butyl and *tert*-butyl molecules are strongly intermixed in extended domains where *tert*-butyl moities adopt the chirality of the *sec*-butyl molecules. In both cases the resulting surface is almost homochiral.

Thorough statistical analyses demonstrate that islands subjected to chiral induction have a strong preference for the RR chiral conformer. This result agrees with a previous study reporting that *sec*-butyl moities tend to adsorb on surfaces with the RR conformation. The novelty of the investigation presented in this chapter lies in the ability of the seeded molecules (*tert*-butyl) to locally adapt to the chirality of the seeding species. This adaptability is due to the low conformational flipping energy barrier of *tert*-butyl molecules, which does not involve any bond breaking contrary to the case of other compounds like for instance the couple tartrate/succinate.

CHAPTER 4

Adsorption structures formed by tetrapeptides on Au(111)

A systematic UHV STM investigation of the adsorption structures formed on Au(111) by two biomolecules, the tetrapeptides KFFE and KVVE, is presented in this chapter. This study presents submolecular-level evidence for self-organization of relatively long flexible biomolecules into various patterns on a metallic substrate. Emphasis is laid on the role of residues in the formation of these structures. Molecular dynamic force field calculations (MDFF) based on a priori knowledge including force fields, distance and symmetry restraints derived from interpretation of the STM data yields information about the intermolecular interactions which might be responsible for the observed patterns. It is demonstrated that these short tetrapeptides can self-assemble into parallel and antiparallel structures of interest in relation to amyloid fibrils formation.

4.1 Introduction

As described in Chapter 1, proteins and peptides can form fibrillar structures composed of β-sheets under specific conditions. The propensity of these biomolecules to aggregate into amyloid fibrils appears to be strongly dependent on their inherent chemical structures. In particular, the lengths and sequences of peptides seem to be among the key determinants for fibrillation. However, the causal factors leading to this event are not yet well understood. Long peptides forming fibrillar structures are mainly aligned *parallel* in β-sheets (see Fig. 1.6). For short peptides, the debate regarding *parallel* or *antiparallel* arrangement in β-sheets is still open. Anyhow, of utmost importance for the present study, tetrapeptides are the smallest peptides able to form fibrillar structures in vitro.

4.1.1 Amyloid fibril formation by KFFE tetrapeptides

By virtue of the fact that KFFE has been identified as one of several minimal peptide units that can form amyloid fibrils in vitro (Fig. 4.1a) this molecule has been the object of intense studies in various research fields [104–107]. In reliance on available experimental data it was earlier proposed an *a priori* model describing the main interactions which might direct fibrillation of KFFE [108]. As shown by the model in Fig. 4.1b fibril-forming tetrapeptides exhibit β-strand structure, and preserve *antiparallel* alignment to generate a β-sheet. Therefore one can anticipate that the β-strand structure of KFFE on its own is a decisive factor for fibril formation. This suggests that KFFE peptides possess the highest β-strand propensities due to the presence of aromatic hydrophobic residues in the middle of KFFE. Additionally, these side groups can contribute to peptide aggregation via their hydrophobic and $\pi - \pi$ interactions. However, all previous studies agreed that the hydrogen bonds between main chains and electrostatic interaction between oppositely charged residues play a dominant role in stabilizing the associated complex.

All research works devoted to this problem have been mainly performed by a combination of cryo-electron microscopy (EM), x-ray, and solid-state nuclear magnetic resonance techniques with molecular modelling. However, the above-listed experimental and theoretical tools cannot give full information about tetrapeptides organization in β-sheets at the molecular level. UHV STM is recognized as one of the most powerful probe techniques for studying molecular self-assembly with nanoscale precision. There are many experimental constraints in biological and medical sciences which should be considered when studying biological systems. For instance, one can reasonably suspect that self-assembly of peptides in UHV might significantly differ from that occurring in the physiological environment, especially due to the absence of liquid interface. Nevertheless, the examination of tetrapeptides that self-assemble into fibrillar structure with UHV STM can be the step towards the understanding of amyloid aggregation mechanisms.

4.1.2 Previous UHV STM studies of amino acids and peptides

In order to understand how peptides and proteins interact with surfaces, the first step is naturally to investigate the behavior of the basic structural units constituting these molecules. Amino acids are the building blocks of proteins, which are inherently essential in

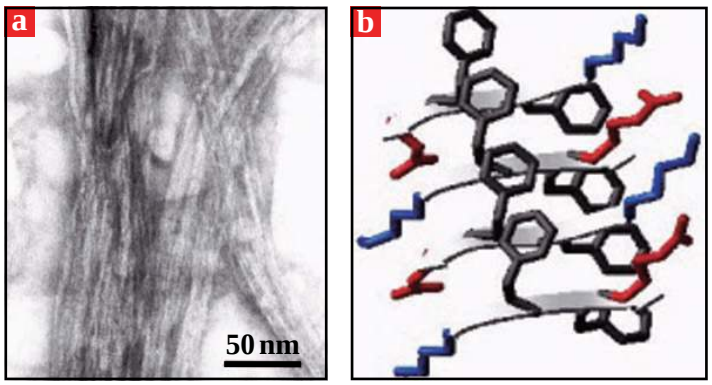

Figure 4.1: Amyloid fibrils formed by the KFFE tetrapeptide. (a) Electron micrograph of KFFE tetrapeptide fibrils obtained after peptide incubation. (b) In this model structure, four *antiparallel* KFFE tetrapeptides associate together to form a β-pleated sheet which is symbolized by flat gray arrows pointing alternately in opposite directions. The β-strands structure is stabilized by electrostatic interactions between the terminal K (blue) and E (red) side chains, van der Waals interactions between phenylalanine side chains (black), and H-bonds between main chains (gray). This figure is adapted from figures 1 and 5 of Ref. [108].

practically all biological functions. The assembly and bonding of simple amino acids on single crystal surfaces has been extensively studied under UHV conditions with various techniques. Most of these studies concern vapour deposited amino acids on Cu substrate due to the affinity of their functional groups for this surface [109, 110]. Moreover, it was found that the sulfur-containing amino acids cystine and methionine can self-assemble or even anchor to Au(111) and Au(110) surfaces through S-Au covalent bonding [84, 111–113]. The only articles addressing the structure and bonding of non-containing sulfur amino acids on Au(111) and Ag/Cu(001) concerns histidine and glycine, respectively [114, 115]. From the theoretical side, a DFT calculation was performed to simulate the interaction of phenylalanine with various substrates, namely a purely repulsive surface of graphene and close-packed surfaces (111) of group 10 (Ni, Pt, Pd) and group 11 (Cu, Ag, Au) metals [116]. SPM studies for larger molecules, such as peptides and proteins, have been restricted to films prepared from solution onto surfaces [117–120]. With these preparation conditions, it is hard to tune parameters such as adsorption rate, film thickness, or to take into account effects due to adsorption at specific sites on the surface. Adsorption of high molecular weight molecules in vapour phase, i.e. avoiding any possible effect of an aqueous solution, is another challenge.

A pioneering work was devoted to the investigation by reflection-absorption infrared spectroscopy (RAIRS) and low-energy electron diffraction (LEED) of the bonding, organization and dynamical growth behaviour of tripeptides, namely tri-L-alanine and tri-L-leucine on Cu(110) [121]. This work was followed by an UHV STM study of di-L-alanine on the same surface. STM images at submolecular resolution demonstrated that these dipeptide molecules are able to form 1D rows at low coverage and extended 2D patterns at higher coverage on this substrate [55].

Recently, chiral recognition events of adsorbed di-phenylalanine on Cu(110) were directly detected by STM [53]. The adsorption of this dipeptide on this substrate leads to the formation of chiral 1D chains. For this biomolecular system, DFT and molecular dynamics (MD) calculations provided a detailed description of the physical processes controlling the adsorption and supramolecular assembly on the Cu(110) surface [54]. The interconnection of these 1D dipeptide chains was realized by coadsorption of diphenylalanine with the organic linker terephthalic acid (TPA) [122]. As a result continuous and a highly ordered 2D motif could be formed by this bimolecular system on both the anisotropic Cu(110) and the isotropic Cu(100) surface.

From all these works, it is clear that even short peptide segments such as dipeptides display topological characteristics related to much larger proteins. The uncovering of well-ordered structures generated by short peptides adsorbed on surfaces is one of the cornerstones toward the understanding of self-assembly processes in complex biological systems.

In this chapter, we show that large flexible biomolecules, i.e tetrapeptides, can be adsorbed on Au(111) by conventional thermal evaporation. These molecules are able to self-assemble on the surface into multiple patterns. The identification of peptides can be derived from a detailed analysis of the STM images obtained at submolecular resolution. In the present study, the focus is to establish how specific intermolecular interactions can stabilize the self-assembly of KFFE and KVVE tetrapeptides on surfaces. To this aim, the experimental investigation is combined with calculations of the peptide self-assemblies in order to provide as much information as possible on the complex determinants directing surface assembly process of biomolecules.

4.1.3 The molecular systems

In this context, two slightly different tetrapeptides, i.e. KFFE and KVVE, were synthesized and investigated in our group. These tetrapeptides are intrinsically formed of four amino acid molecules joined together upon water release and formation of amide bonds. As can be seen from Fig. 4.2, the peptide chains of KFFE and KVVE bear the same lysine (K) and glutamate (E) side groups at the ends, and different two side groups at their centers, viz. di-phenylalanine (FF) and di-valine (VV), respectively. Furthermore, the peptides can possess distinct charge states depending on the surrounding environment. In concordance with previous studies solvated molecules can be found in neutral, ionic or zwitterionic form depending on the pH of the solution while in vacuum the molecule should preserve its neutral state.

The high flexibility of both molecules provides a large number of molecular conformational states. Moreover, the phenyl side groups of KFFE peptide have also high conformational flexibility. As demonstrated by the ball-stick model of KFFE in Fig. 4.2, the phenyl ring is almost free to rotate around the C_β-C_γ bond, while the torsion χ around the $C_\beta - C_\alpha$ bond is limited. The aromatic residues can also bend "out-of-plane" by an angle θ. In the case of KVVE peptides, the flexibility of the central valine side groups is possible only around the C_β-C_α bond.

Furthermore, the conformations adopted by these molecules on surface might crucially differ from those in the gas phase (see Fig. 4.2). This behavior can be explained by the constraints on the intramolecular arrangement and surface-molecule interaction

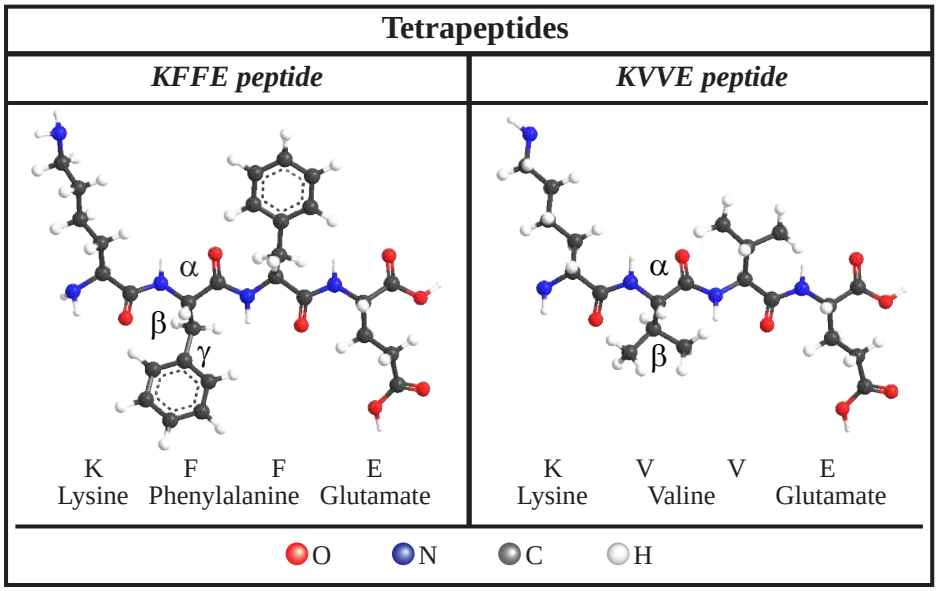

Figure 4.2: Molecular structures of KFFE and KVVE tetrapeptides in gas phase.

exerted by the presence of a substrate. Therefore, when the experimental data are interpreted it is necessary to account for the interplay between the intrinsic conformational preferences of the free molecule and molecule-surface interaction. This issue will be discussed in more details later on.

Experiments using chemically-related tetrapeptides, KFFE and KVVE, were performed to further elucidate the role of different side groups on the organization and STM imaging of single peptides. Both tetrapeptides were supplied as solid white powders at RT. The KFFE and KVVE molecules were sublimated in UHV from a thermal evaporation source at 426 K and 470K, respectively. After deposition of submonolayer quantities of KFFE onto a Au(111) surface kept at room temperature, well ordered structures were observed by STM imaging at 125-180 K. The imaging was performed in constant current mode ($I_t \sim 0.4$ nm) and bias voltage of $V_t = -1.25$ V with respect to the sample. Calculations assisted by experimental data have been performed with the XPLOR-NIH package.

4.2 Parallel row structure formed by KFFE and KVVE

One of the most intriguing findings in this study is that KFFE and KVVE tetrapeptides can form the same molecular motif on the surface. The Au(111) herringbone reconstruction can be unambiguously resolved underneath extended molecular islands indicating relatively weak peptide-substrate interaction.

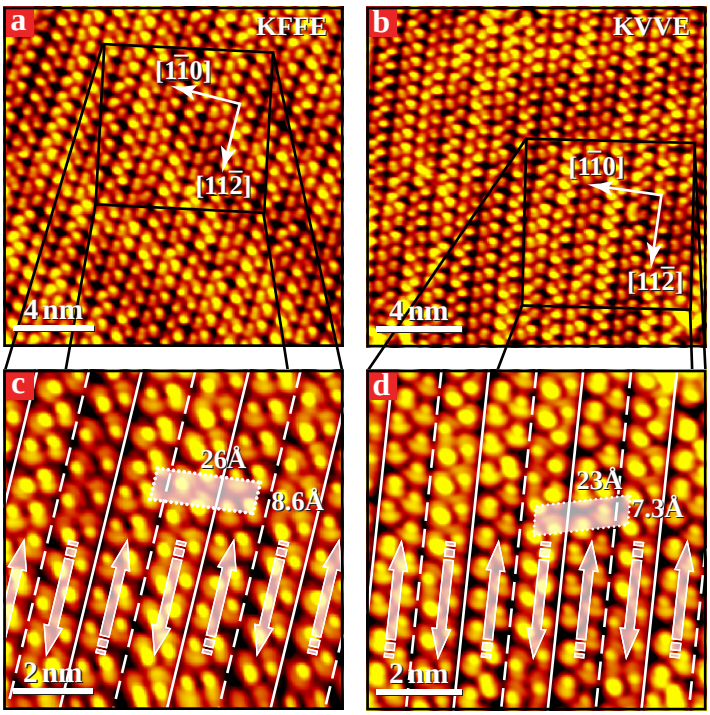

Figure 4.3: Parallel row structures of KFFE and KVVE tetrapeptides on Au(111) (row boundaries are underlined by solid and dashed lines): (a) and (b) Parallel rows of KFFE and KVVE, respectively; (c) and (d) Enhanced representations of the KFFE and KVVE structures in the regions marked in panels (a) and (b), respectively. Alternating orientations of molecules within rows are indicated by arrows.

4.2.1 STM results

As shown in Fig. 4.3a,b, the parallel row structure of both peptides is formed from characteristic double protrusions. However, the unit cell of the parallel row structure formed by KFFE (26Å$\times$8.6Å) is slightly larger than that observed for KVVE (23Å$\times$7.3Å) as evidenced in Fig. 4.3c,d. The higher packing density of the row structure formed by KVVE can be explained by the presence of middle VV residues which are smaller compared to the FF side groups of KFFE.

Unfortunately, it is difficult to determine from the molecular pattern of Fig. 4.3 which STM image features belong to single peptides. Instead, the individual peptide units have been identified from a careful examination of point defects and island perimeters which are seen in the STM images of Fig. 4.4a,b. The row-like ordered domains are terminated by dumbbell-like features, circled in white, which are clearly isolated from the surrounding disordered structure in the uppermost parts of the images. It is important to note that the long axis of the dumbbells (represented by black dashed lines in the figures) makes an acute angle with respect to row boundaries and that the size of this axis amounts to

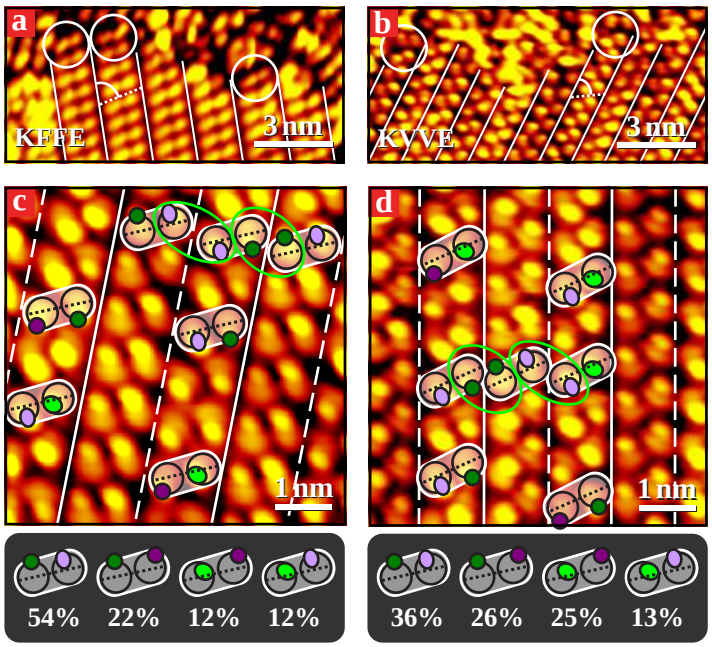

Figure 4.4: STM images of point defects and conformer orientations in the row parallel structures of KFFE and KVVE on Au(111). (a) Row defects of KFFE at molecular islands perimeters marked by white circles. (b) Row defects of KVVE at islands perimeters marked by white circles. (c) and (d) Submolecular-resolved patterns of different conformers of KFFE and KVVE, respectively. The molecules are located in white contours, while their conformers are oriented as indicated by the protrusions labeled in color. Mutual orientations are indicated by green ovals. Conformers of KFFE and KVVE are sketched by conformations 1 (left) to 4 (right) with their relative abundance beneath panels (c) and (d), respectively.

12Å, which is a distance corresponding well to the length of the extended backbones of KFFE and KVVE. One can conclude that each imaged dumbbell represents a single peptide and that the peptide molecules are parallelly stacked along the rows with their axis forming an accute angle with respect to the row boundaries. Therefore, it is now possible to identify the STM features belonging to a single tetrapetide as illustrated in Fig. 4.4c,d.

At submolecular resolution, the STM images show that each single peptide is composed of *2 double* protrusions which we have delimited by white contours. Each of these double protrusions contains a bright and a dim part. The brighter parts, highlighted in the figure by small disks of different colors, assume 4 different orientations with respect to the molecular axes. This means that 4 peptides conformers can be distinguished in the row structures. A statistics of the conformer occurrences was therefore derived by counting the number of conformers in a selection of 10 STM images taken from samples prepared in exactly the same experimental conditions. The results are summarized in the

bottom panels of Fig. 4.4. For both peptides conformation **1** is more often observed in the row motif than other conformations. In the case of KFFE this preponderance is significant while for KVVE the probability to see conformation **1** does not differ too much from the other ones (Fig. 4.4c,d, bottom). Conformation **4** is the most improbable.

The different orientations of the bright protrusions suggest they undergo a dynamical behavior. This assumption was confirmed by time-lapsed sequences of STM images taken each 10s showing that tetrapeptides can adopt four different conformations with respect to middle residues orientations. Moreover, previous theoretical studies suggested that phenylalanine side groups might exhibit substantial conformational flexibility around $C_\beta - C_\gamma$ and $C_\beta - C_\alpha$ bonds on the Au(111) surface. It appears reasonable to assign the bright protrusions to the electron rich phenyl or valine moieties and the dimmer protrusions to the peptide backbones. Thus the rare appearance of conformer **4** could be simply explained by the fact that the F or V side chains in this conformation are pointing towards each other, which may lead to steric hindrance.

Furthermore STM images with sub-molecular resolution clearly show that the bright protrusions within one particular row have the same orientation, whereas the same protrusions located in the adjacent neighbouring row point in opposite direction as illustrated by arrows in Fig. 4.3c,d.

A careful inspection of rows with opposite orientation reveals two different boundaries between them. The adjacent molecules across solid and dashed line boundaries are shifted in such a way that their aromatic side groups are pointing either towards each other or in opposite direction, respectively (see Fig. 4.4c,d). The orientations of the aromatic side groups within and between rows are strongly correlated, pointing towards directional intermolecular interactions.

The molecular islands show a preferential orientation with respect to the substrate (see Fig. 4.3a,b). The molecular rows of these islands are running along $[11\bar{2}]$ direction, while the main axis going through the two aromatic residues of single tetrapeptides within these rows makes an angle of 116° with respect to the close-packed $[1\bar{1}0]$ direction. However, it is impossible to distinguish where glutamate and lysine residues are located in this molecular motif. One can argue that a thermal decomposition of the tetrapeptides may occur during their evaporation but careful inspection of the surface did not reveal fragmented molecules.

4.2.2 Restrained MDFF structure-calculation

In this Section it is described how the XPLOR-NIH package has been used for obtaining tetrapeptide molecular structural models adsorbed on the Au(111) surface. The restrained MDFF calculations have been implemented and carried out by Jakob T. Nielsen, from the Chemistry Department of the University of Aarhus.

The MDFF approach is intensively used in the calculation of protein structures assisted by NMR data. The challenge of the present work is to use this theoretical tool and to transfer it for the calculation of peptides self-assembly on surfaces. It is the first time to our knowledge that the MDFF method is assisted by STM images whose experimental restraints are implemented in XPLOR-NIH calculations. The method involves the calculation of *800 different structural models* by introducing the force field, the symmetry restraints and the distance restraints extracted from the STM images. It should be

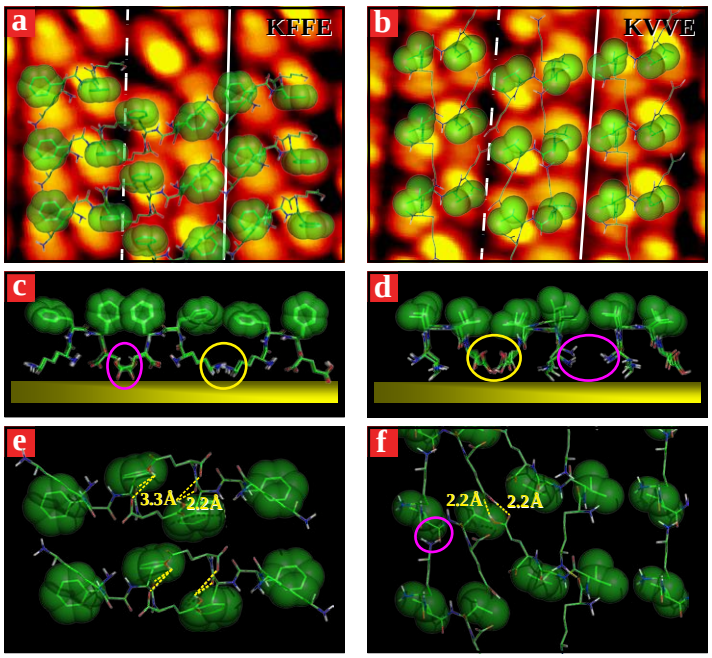

Figure 4.5: Best overlays of MDFF structural models to STM images for KFFE and KVVE parallel rows. (a-d) Top and side views of the MDFF structures. F and V side chains are represented by green balls. From the side views, it can be inferred that the molecules adsorb with an U-shaped geometry on the Au(111) surface. (e,f) Short contacts in pairs of KFFE and KVVE molecules.

emphasized that XPLOR calculations are assisted by the fact that STM images provide projected true distances of the peptide geometries adsorbed at the surface. *Symmetry restraints* take into account rotations and translations of the pattern and are therefore free of errors. *Unit cell distance restraints* depend essentially on the STM image calibration. The distances between protrusions representing identical parts of the molecule measured within several unit cells of the patterns (transparent frames in Fig. 4.3cd) are projected true distances and can yield errors of about 5%. The largest errors in the calculation (about 20%) come from the distance restraints between atoms related by a rotational symmetry and from 3D distances taken as projected 2D distances. These restraints are based on assignment of STM features to specific atoms or groups which can be superimposed to themselves by a rotation. In our case, these features can be the bright protrusions assigned to F or V side chains. A few subjective additional restraints are introduced. The "planarity" restraint assumes that all atoms lie within a 8 Å layer. This is introduced to mimic the presence of the surface but the molecule-substrate interaction is not taken in account. The "polarity" restraint constrains polar side chains (like $-$COOH) and terminal groups (like $-NH_2$) within a 1 Å layer.

A selection of *only 10 structures* presenting the best total energy is made. Among these 10 possibilities, the ones having the best visual overlay with the STM images are

chosen. In this way, the restrained MDFF structures are very plausible models whose restraints are derived from STM data assignment.

Fig 4.5a,b shows the calculated models presenting the best overlays to the experimental STM images of the parallel row patterns. The "bulky" groups in green color represent phenylalanine (F) and valine (V) groups. In the top views, the overlap of F and V residues with the bright protrusions of the STM images is very satisfactory.

The side views of the model in Fig 4.5c,d show that the molecular backbones are not fully extended but adopt distinctly an U-shaped conformation upon adsorption at the surface (Fig 4.6a,b): i.e. glutamate (E) and lysine (K) residues, as well as α-amino and α-carboxyl groups, are pointing towards the Au(111) surface while the F and V sidegroups point away from the surface. This could explain why K and E side chains are not visualized in the STM images.

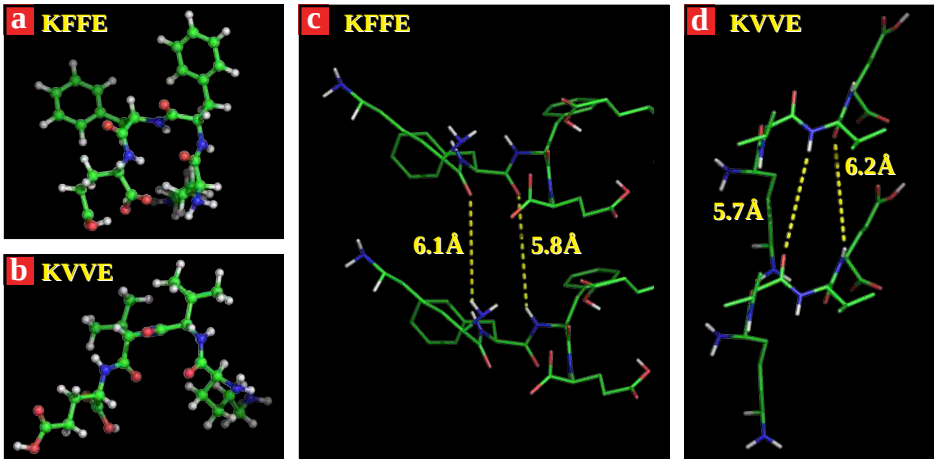

Figure 4.6: MDFF models of the KFFE and KVVE monomers in parallel rows. (a,b) KFFE and KVVE monomers. (c,d) KFFE and KVVE monomer contacts.

The calculated conformation of the single molecules is in good correspondence with previous theoretical studies, which stressed that the U-shaped conformation of KFFE peptides shown in Fig 4.6a,b can be relatively stable [106, 107]. These U-shaped molecules are not extended and have a tendency to align parallel within the rows. The average distance between two sideway molecular backbones is about 6 Å for KFFE and KVVE peptides (see Fig 4.6c,d). This distance is too large to enable H-bonding between the backbones of parallel tetrapeptides. Some other interaction might therefore be responsible for holding together the molecules into these row structures.

The $\pi - \pi$ interaction between phenylalanine side groups of KFFE can be an additional factor for stabilization of this row structure. As a consequence one can suggest that the parallel row structure formed by KVVE might be less stable than that observed for KFFE. This assumption can explain why this is the only structure observed after KFFE dosing. Indeed, in the case of KVVE molecules, we found many other molecular patterns coexisting with parallel row structures, which will be described later on.

More directional alignment of the bright protrusions corresponding to phenylalanine side chains in KFFE self-assembly (we recall that conformation 1 is predominant) can also result from $\pi - \pi$ interactions between aromatic rings, while smaller valine side chains in KVVE self-assembly are less restricted in conformational flexibility due to the absence of such interactions.

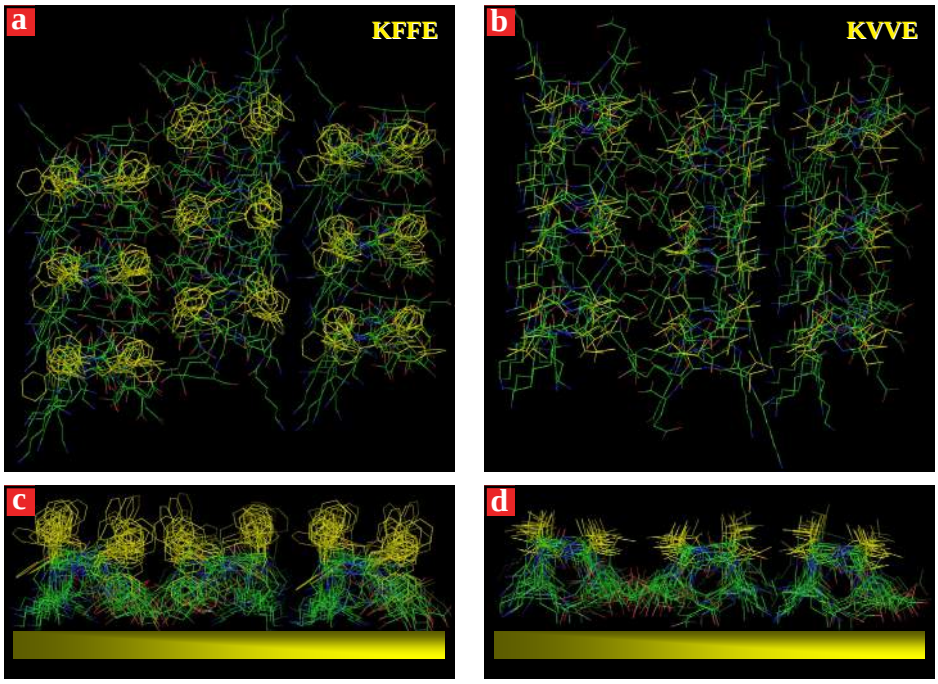

Figure 4.7: Overlay of the 10 lowest energy MDFF structures of KFFE and KVVE parallel row patterns on Au(111) calculated with XPLOR-NIH package. (a) and (c): top and side views of KFFE rows. (b) and (d): top and side views of KVVE rows.

The MDFF structural models show that neighbouring rows of peptides are separated by two types of boundaries illustrated by solid and dashed lines in Fig 4.5ab. For KFFE, these boundaries are defined by K$\cdots$K and E$\cdots$E "inter-row contacts" between peptide molecules located in adjacent rows. The contacts are sketchted by yellow and pink ovals, respectively, in Fig 4.5c. In the case of KVVE, E$\cdots$E inter-row contacts and inter-row amino termini contacts ($-NH_2$) delineate these inter-row boundaries. They are sketchted by yellow and pink ovals, respectively, in Fig 4.5d. From the top-views of these models which are depicted in Fig 4.5ab, one can anticipate that intra-row molecules are indeed aligned parallel, while inter-row molecules preserve a head-to-head arrangement (via E$\cdots$E, or amino$\cdots$amino contacts). The 2D parallel row structure of KFFE is likely stabilized also by H-bonding between glutamate side chains and α-carboxyl termini or backbone oxygen atoms of molecules in head-to-head contact across the inter-row boundaries as illustrated by yellow dashed lines in Fig 4.5e. For KVVE the

stabilization of the rows can be favored by double hydrogen bonding between glutamate side chains of neighbouring molecules across row boundaries. This type of bonding is illustrated by yellow dashed lines in Fig 4.5f). Inter-row H-bonding can therefore be an additional factor for the formation of the 2D parallel row structure of KFFE and KVVE self-assemblies. In the case of KVVE, K side chains can additionally form H-bonding with backbone oxygen atoms of neighbouring molecules belonging to the same rows. These bondings are shown by pink ovals Fig 4.5f). They may participate in the stabilization of the intra-row structure. Fig 4.7a-d presents overlays of the 10 lowest energy structures (TLES) calculated for KFFE and KVVE from the STM images of the parallel row structures described in Section 4.2.1. The above discussed two models apparently describe quite completely the general features which can be distinguished in the TLES ensembles. For both peptides, overlay of all models exhibit U-shaped conformation and parallel alignment of molecules, as well as head-to-head molecular interactions between the rows. From the TLES side views, the overlap of the molecular backbones and K and E side chains is better for KVVE than for KFFE. Additionally, it can be seen that F side chains are seemingly more flexible than V side chains since the latter overlap better. This could be explained by the additional degree of freedom of F groups around the $C_\beta - C_\gamma$ bond. Nevertheless, one should keep in mind that the apparent flexibility in these TLES ensembles might reflect a lack of restraints, which is inherent to the calculation against 2D STM images, rather than a true flexibility.

Since the monomers have an U-shaped backbone and since the distance between parallel molecules is too large for hydrogen bonding ($d = 6$Å) the parallel pattern is somewhat different from the amyloid fibril structure ($d \sim 4.5$ Å). It might nevertheless represent a structural onset before fibril formation.

In addition, the molecules in sideway contact along the rows are shifted in STM images by 3.5 Å and 3 Å for KFFE and KVVE, respectively. These values are approximately half those observed in a previous UHV STM study of di-phenylalanine self-assembly on Cu(110) pointed out that the latter peptides are only able to form isolated 1D rows [53]. Therefore, one can suspect that KFFE and KVVE rows merge into a 2D structure due to the presence of glutamate and lysine residues.

4.3 Antiparallel row structure formed by KVVE

Another interesting 2D molecular motif formed by KVVE peptides on Au(111) is an antiparallel row structure.

4.3.1 STM results

This structure has been observed in three different imaging modes attributed to different states of the STM tip (see Fig. 4.8). In the most frequent imaging mode are observed eight protrusions which are arranged in a four-blade rotor-like shape as seen from Fig. 4.8a. An examination of point defects and island perimeters was carried out for this structure by a reasoning analogous to that presented in Section 4.2.1. From this analysis it follows that the individual molecules are composed of four protrusions which are illustrated by L-shaped contours on the STM image (see middle panels Fig. 4.8a). Therefore, it is reasonable to assume that each single protrusion of this STM feature belongs to one residue of the tetrapeptide. Additionally, one can assume that peptides

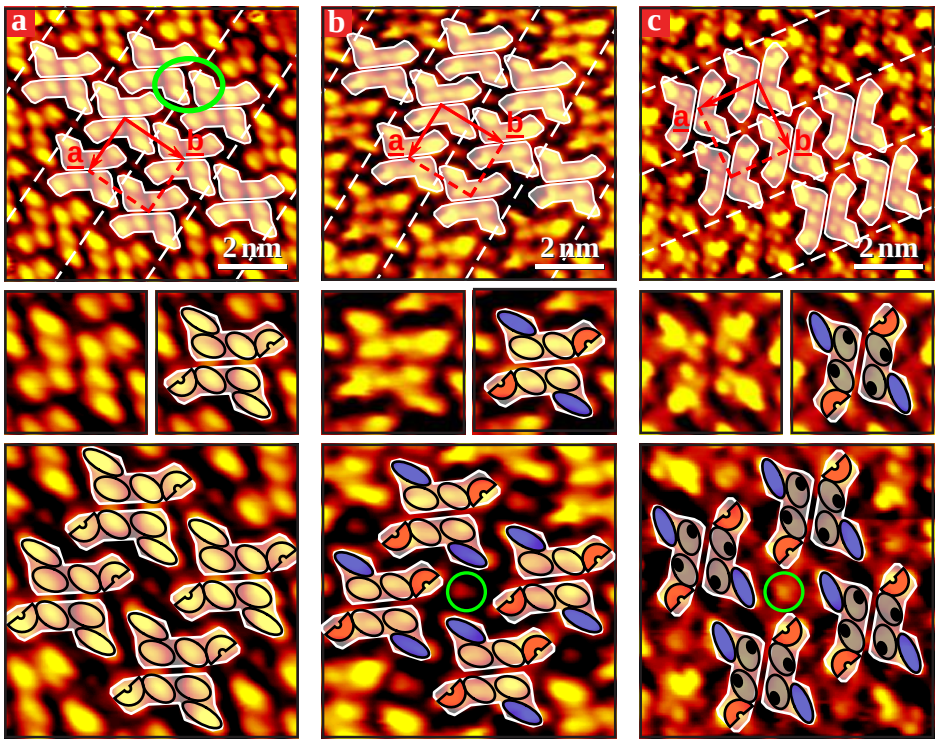

Figure 4.8: Antiparallel row structure of KVVE tetrapeptide on Au(111), registered under three STM imaging conditions (row boundaries are underlined by dashed lines): (a) Four-residue imaging mode; (b) Glutamate/Lysine and backbone imaging mode; (c) Glutamate/Valine/Lysine/ imaging mode. L-shaped molecules and residues are sketched by white contours and colored shapes in enhanced representations, respectively, while black dots indicate conformer orientations. Glutamate and lysine residues are marked by blue ovals and red contours, respectively. Additional periodically repeating dim protrusions not attributable to extraneous impurities are circled in green color along the boundary between adjacent rows.

forming this structure are adsorbed in a more flat conformation with respect to the surface since it is possible to visualize all four side groups of each single peptide.

The prominent rotor-like feature is formed by two such adjacent L-shaped contours rotated by 180° with respect to each other, as demonstrated in the middle panel of Fig. 4.8a. The extended surface structure is formed by translation of this peptide pair along two orthogonal directions resulting in a rectangular unit cell with parameters $|\mathbf{a}|$ and $|\mathbf{b}|$ of 18.3 Å and 21.4 Å, respectively. As can be seen from the top panel in Fig. 4.8a the L-shaped features agglomerate into a "top-to-tail" stacking within the rows. Furthermore, the peptide pairs in the rows are shifted by 10.7 Å along the main axis of single tetrapeptide. This results in a higher packing density of peptide pairs within rows, which might facilitate intermolecular interaction between KVVE molecules of neighbouring

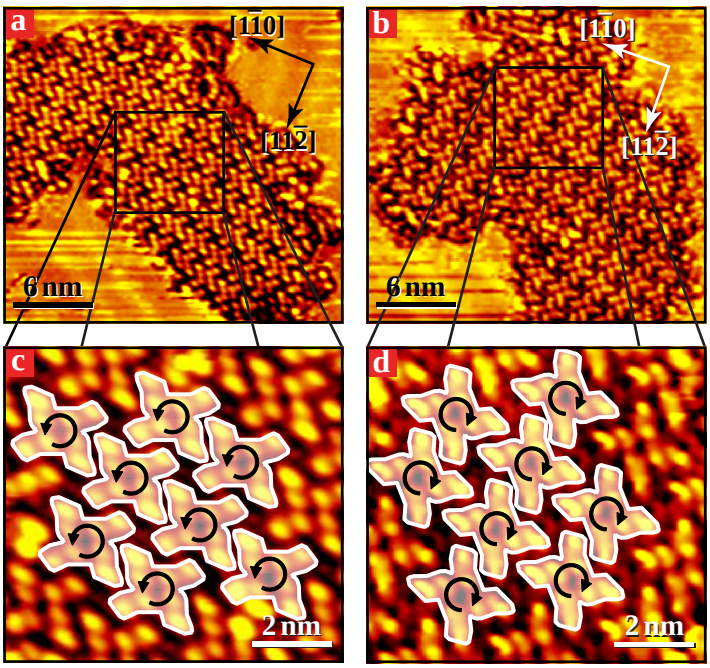

Figure 4.9: Antiparallel row structures of chiral KVVE molecular islands registered under specific STM imaging conditions: (a) Extended ordered molecular island with anti-clockwise chiral pattern; (b) Extended ordered molecular island with clockwise chiral pattern; (c) Enhanced representation of the black frame in panel (a) showing antiparallel arrangement of L-shaped KVVE molecules with anti-clockwise rotations; (d) Enhanced representation of the black frame in panel (b) showing antiparallel arrangement of L-shaped KVVE molecules with clockwise rotations.

rotor-like features.

Examination of neighbouring rows reveals that they are identical, but displaced along boundaries marked by dashed lines. As a consequence the packing density of rotor-like features transverse to the row direction is maximized as well. However, such a shift causes tail-to-tail arrangements of L-shaped contours across boundaries as illustrated by green ovals in the top panel of Fig. 4.8a.

Another imaging mode of this structure is presented in Fig. 4.8b. In this case, a single molecule is imaged as two bright elongated protrusions interconnected by a slightly bent dimmer part. The image contrast is caused mainly by aliphatic residues (K and E) and by the main chain. The length of the elongated bright protrusion (blue oval) is 6.9 Å which corresponds to the dimension of a fully stretched lysine chain, and is significantly larger than a stretched glutamate side group in the free-peptide model presented in Fig. 4.2. Thus, one can suggest that the large (blue oval) and small (red contour) bright protrusions can be attributed to the lysine and glutamate residues, respectively. This image allows to distinguish between lysine and glutamate side groups.

Consequently, the direct observation of glutamate and lysine residues yields strong

evidence of an antiparallel alignment of the peptides within the rows. The enhanced representation of four nearest rotor-like features forming this pattern displays the presence of additional periodically repeating round dim protrusions along the boundary between adjacent rows. As illustrated by green circles in the bottom panel of Fig. 4.8b these dim protrusions affiliate two glutamate and two lysine side chains from the nearest antiparallel peptides. Thorough examination of the surface suggests that these features cannot be attributed to impurities since they would be expected to decorate step edges and molecular islands which is not the case. We speculate that these protrusions might be caused by some specific intermolecular interaction or electronic effect occurring on the surface rather than by the presence of extraneous inclusions.

The final imaging mode of the antiparallel row structure is depicted in Fig. 4.8c. From this image it is difficult, but still possible to distinguish between glutamate and lysine residues. Additionally, the middle residues appear in STM imaging as double protrusions composed of bright and dimmer parts. Analogous to the parallel row structure, the bright protrusions are assigned to the valine side chains. From the enhanced representation of a single rotor-like STM feature it is clear that valine residues for each individual peptide are oriented in the direction opposite to the lysine side group. As expected the valine residues of adjacent peptides within rows point in opposite direction confirming the previous finding (Fig. 4.8b) of antiparallel peptide arrangement in this molecular pattern. Contrary to the parallel row structure, V residues do not show flexibility.

A study of several molecular islands shows that the antiparallel row structure is represented by two chiral forms, viz. rotor-like features forming this pattern exhibit clockwise or anticlockwise rotation (see Fig. 4.9). The rows of antiparallel peptides for both chiral motifs are rotated by an angle of 12° with respect to the $[11\overline{2}]$ direction of the Au(111) surface. It implies a strong preferential orientation of molecular rows with respect to the surface. Additionally, the peptide backbones within rows form an angle 53° and -53° (see Fig. 4.8b,c) with the boundary between two adjacent rows for clockwise and anticlockwise structures, respectively. By combining the information given by each imaging mode it is possible to get a complete and convincing picture of peptide conformation and alignment in this structure.

4.3.2 Restrained MDFF structure-calculation

Restrained MDFF structural models of the antiparallel row pattern of KVVE were calculated using a somewhat different procedure than that described in Section 4.3.1. There was no polarity restraints since we observed E and K side chains and did not observe flexibility of V side chains. Fig. 4.10a,b presents an overlay of the 10 lowest energy structures (TLES) of KVVE antiparallel row self-assembly derived STM images of Section 4.3.1. Here, the TLES ensemble seems to be less flexible than those calculated for the parallel row structure. The TLES ensemble is able to render rather well the observed rotor-like features. This fact is well exemplified in the top view arrangement of Fig. 4.10a reproducing a clockwise pattern presenting an extremeky good match to the experimental STM motif. In Fig. 4.10c the best structure is overlaid to the experimental STM image with anticlockwise pattern. This MDFF structural model is in agreement with the previously discussed assignment of the experimental STM features. In

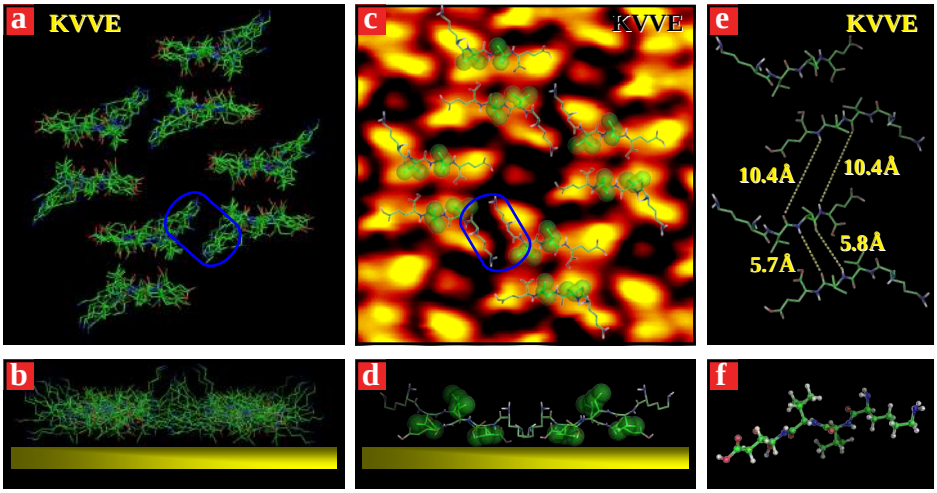

Figure 4.10: The MDFF structural model of the KVVE antiparallel row pattern on Au(111) calculated with XPLOR-NIH package. (a) and (c): top and side views overlay of the 10 lowest energy structures KVVE (clockwise pattern). (b) Best overlay of the model to the high resolution STM image (anticlockwise pattern). (d) Side view of the molecular structure of panel (b). The valine groups are sketched by green balls in panels (b) and (d). Contacts between KVVE (e) and KVVE monomers (f).

particular, close examination of single molecular features corroborates that elongated protrusions forming the short arms in the L-shaped contours discussed in Section 4.3.1 originate effectively from long lysine side chains. Furthermore, lysine side chains (K) belonging to 2 neighbouring molecules across a row boundary highlighted by blue circles are aligned parallel and point in opposite directions, a configuration similar to that described in previous studies of aliphatic chains (Fig. 4.10c). The side view of this stick model (Fig. 4.10d) shows that the molecules are adsorbed flat on the surface. The molecular backbones are closer to the surface than for the parallel row structure. Molecular monomers are distinctly S-shaped (Fig. 4.10e,f). The side chains lysine, valine, glutamate, point alternately upwards or downwards the surface. The α-carboxyl groups are oriented towards the substrate (Fig. 4.10d). The MDFF structural model shows that the distances between two antiparallel KVVE inward and between rotor-like features within a single row are too large (5.8 Å and 10.4 Å) for H-bonding (see Fig. 4.10e). As already assumed from the STM image analysis, the overlap of the model on the experimental STM image testifies that the tetrapeptides are stacked along the rows sideway with antiparallel alignment (Fig. 4.10b). The MDFF structural model has some similarity with a fibrillar structure since KVVE monomers have extended S shape conformation and are aligned antiparallel, but cannot be correlated to a fibrillization process since there is no H-bonding between molecular backbones.

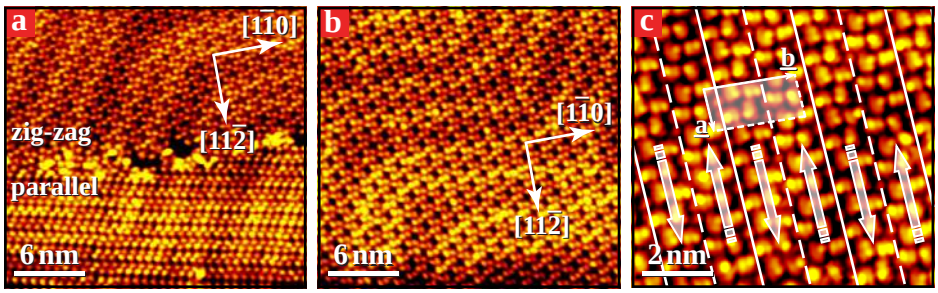

Figure 4.11: zig-zag row structure of KVVE tetrapeptide on Au(111). (a) STM image of a molecular island showing two coexisting extended ordered domains with zig-zag (uppermost part) and parallel (bottommost part) row structures. The two domains are separated by regions with defects. (b) The KVVE zig-zag row structure of a molecular island showing the herringbone reconstruction pattern of Au(111) beneath the molecular layer. (c) STM image displaying molecular rows of two kinds separated by solid and dashed lines with alternating orientations indicated by the arrows.

4.4 Other structures formed by KVVE or KFFE

4.4.1 Zig-zag like structure of KVVE

As shown on the STM image in Fig. 4.11a submonolayer coverage of KVVE on Au(111) results in an additional highly ordered molecular motif coexisting with the parallel row structure. The herringbone reconstruction of the Au(111) is extremely well-resolved beneath the molecular layers (Fig. 4.11b). Peptides molecules are therefore expected to interact weakly with the underlying substrate as in the previously discussed structures. The high magnification STM image in Fig. 4.11c shows that molecules are arranged in rows significantly different from those observed in the parallel and antiparallel row structures. The rows of this structure are rotated by an angle of 15° with respect to the close-packed [11$\bar{2}$] direction of the Au(111) surface.

The molecular motif has an oblique unit cell defined by vectors **a** and **b** parallel and almost transverse to the row direction, respectively. The unit cell has dimensions $|\mathbf{a}|$ = 12.4Å and $|\mathbf{b}|$ = 26.5Å, with an angle $\angle\mathbf{ab}$= 85°, and contains 8 elongated protrusions ascribed to 4 peptide molecules. As for parallel row structures, each molecule is imaged by two elongated protrusions decorated with small brighter protuberances attributed valine side chains (see Fig. 4.12a). As illustrated by the arrows in Fig. 4.11c and by the contours in Fig. 4.12b, double bright protrusions within a single row point upwards while in the adjacent rows they point downwards. Therefore, the structure consists of parallel equidistant rows (13 Å) revealing directional molecular orientation similar to the case of the parallel row structure described above.

At submolecular resolution in Fig. 4.12b, a subtle and complex ordering pattern appears. Within rows one can distinguish alternating peptides with two orientations: the first one is orthogonal to the row direction (white contours) while the second one is skewed with respect to that direction (green contours). The angle between two adjacent molecules is 22.4°. As a result, the stacking molecular arrangement within rows is zigzag-like.

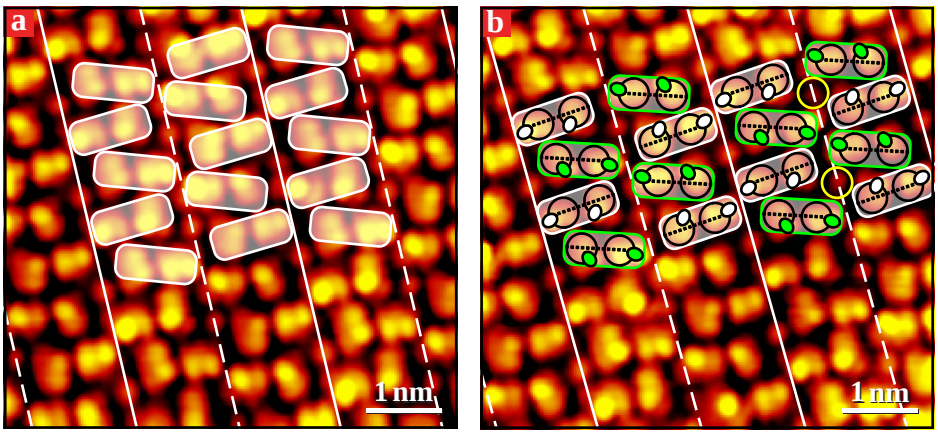

Figure 4.12: Submolecular-resolved patterns of different conformers of KVVE. (a) Alternating zig-zag row structure with single peptide molecules located in white contours. (b) Sketch of molecular conformers pointing towards each other across boundary lines as indicated by the protrusions labeled in color. Additional periodically repeating dim protrusions not attributable to extraneous impurities are circled in white color along the boundary between adjacent rows.

Careful comparison of the orientation of bright protrusions (green and white contours) reveals that they point in opposite directions with the same tilt angle relatively to the molecular axes (black dashed lines). Furthermore, all molecules in each row can be superimposed to those of the adjacent rows by a 180° rotation. As a result, the rows are separated by two different boundaries: across the solid and dashed lines, peptides labeled by white and green contour are pointing towards each other, respectively, and might arrange head-to-head.

Interestingly, additional periodically repeating round dim protrusions are observed along the boundary between adjacent rows similarly to the case of the antiparallel row structure. Again, these dim protrusions are surrounded by two pairs of peptides (outlined in white and green colors).

4.4.2 Cross-linked row structure of KVVE

The most complex molecular pattern formed by the KVVE peptide on the Au(111) surface is a cross-linked row structure shown in Fig. 4.13a. Even at low imaging resolution, it is clear that the structure consists of alternating parallel molecular rows of two different widths. The molecular motif shown in Fig. 4.13c has an oblique unit cell defined by vectors **a** and **b** parallel and inclined by an angle of 118° with respect to the row direction, respectively. The unit cell has rather big dimension ($|\mathbf{a}|$= 14.3Å, $|\mathbf{b}|$ = 26.1Å) with respect to the simple parallel row structure and comprises 8 protrusions. From island-edge analysis a single peptide molecule can be ascribed to two protrusions as shown by white contours in Fig. 4.13c.

Interestingly, the narrower rows have a width (10.9 Å) equal to that of the parallel row structure. One can distinguish *molecule pairs* lying roughly orthogonally to the

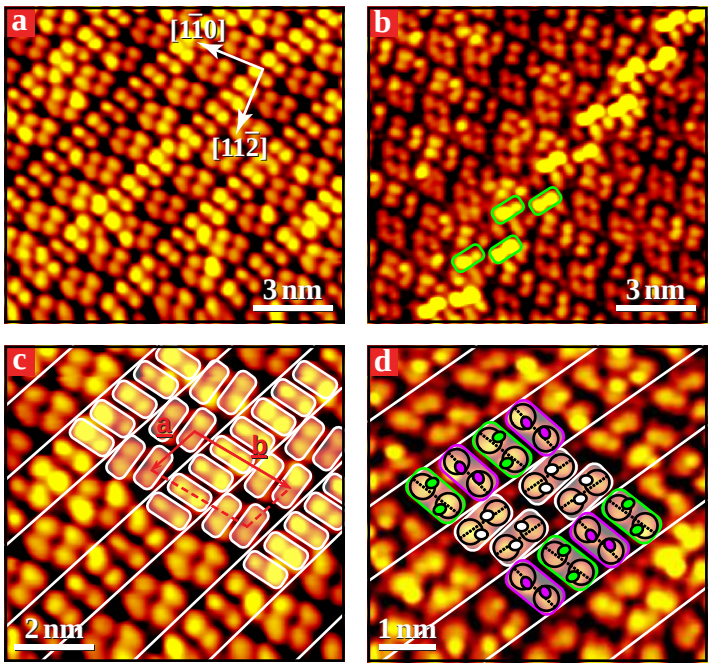

Figure 4.13: Formation of the cross-linked row structure by KVVE peptide on Au(111). (a) STM image of the cross-linked row structure at monolayer coverage of KVVE peptide. (b) Growth of a second monolayer of KVVE peptide on the first one. (c) The two different molecular arrangement in the alternating rows. (d) Molecular conformation analysis.

row direction. Herein, molecules stack side-by-side readily upon each other to produce a densely packed row. This arrangement is similar to that observed for the parallel row structure described above, but here the average distance between the molecules within the rows is larger (about 8 Å against 6.2 Å). Significantly different molecular arrangement occurs in the broader rows (12.3 Å width). The pairs align head-to-tail along the rows with periodicity of 14 Å .

At higher resolution (see Fig. 4.13d), each molecule is imaged as two protrusions decorated by small brighter protuberances, stemming probably from valine residues in agreement with the previous structures described above. This vividly demonstrates that the narrow rows comprise two different alternating molecular conformers. In the first conformer bright protrusions (in green) are pointing to opposite sides along the row axis, while in the second conformer they are pointing toward each other along the molecular axis. From the presence of two alternating different conformers within narrow rows, it appears that the molecules could be aligned antiparallel. This conclusion is also supported by an intermolecular distance larger than that observed for the parallel row structure. Broader rows contain only one type of molecular conformer (white contours). In each pair the molecules are superimposable by a rotation of 180° which might indicate an antiparallel alignment.

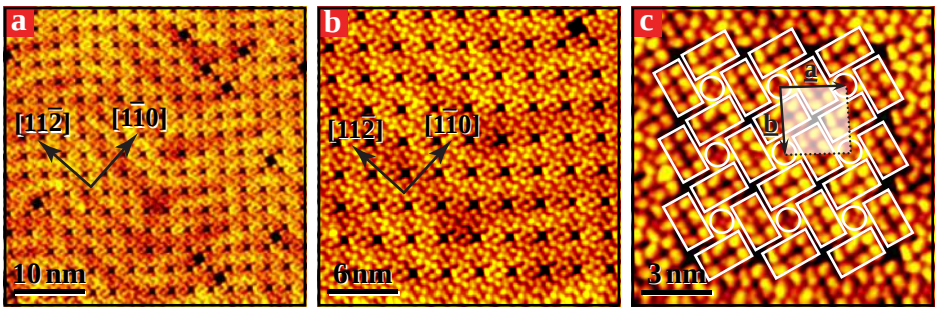

Figure 4.14: Formation of the porous windmill structure by KVVE peptide on Au(111). (a) KFFE well-ordered porous network of a molecular island showing the herringbone reconstruction pattern of Au(111) beneath the molecular layer. (b) Enhanced representation of the island shown in panel (a). (c) Zoom-in image into the structure showing a characteristic four-bladed windmill pattern.

The strongly correlated orientations of the valine side chains between narrow and broad rows suggest that particular intermolecular interactions take place between these 2 types of rows. Fig. 4.13d exemplifies that each peptide in pairs forming the broad rows could interact with both molecular conformers - illustrated by green and violet features - in narrow rows. It is seen that upon 180° rotation the molecules in broad rows keep the same kind of interactions with adjacent molecules belonging to narrow rows.

Time-lapsed sequence of STM images shows that the bright protrusions can change orientations with respect to their initial preferable orientations. From the high flexibility of these protrusions assigned to valine groups, one can suggest that these residues are pointing upwards from the surface and are not strongly bonded to it.

4.4.3 Windmill structure of KFFE

When the initial parallel row structure formed by KFFE molecules is annealed at T=315K, an additional structure is found on Au(111) (see Fig. 4.14). A well-resolved herringbone reconstruction of the Au(111) surface is observed beneath the molecular layers. In this molecular island, KFFE peptides self-assemble in a well-ordered porous network (Fig. 4.14b). The enhanced representation in Fig. 4.14c shows that this pattern is defined by an oblique unit cell with parameters $|\mathbf{a}| = 29$Å and $|\mathbf{b}| = 30$Å. The highly ordered structure can be defined as 4 short subunits composed of 6 protrusions joining at a common node consisting of 4 protrusions, as shown by the rectangular and circular frames of Fig. 4.14c. This self-assembly can therefore be termed as a four-bladed windmill structure.

From the ideal structure it is not possible to discern which protrusion belongs to a single peptide. A close look at another molecular island (Fig. 4.15a) acquired under the same conditions reveals vacancies in this ordered structure. The vacancies shown by green circles clearly correspond to missing nodes. Therefore, the 4 missing protrusions are ascribed to 2 KFFE tetrapeptides.

In some instances it was possible to find additional protrusion pairs shown by violet contours in Fig. 4.15b which are adsorbed parallel to short sides of rectangular subunits

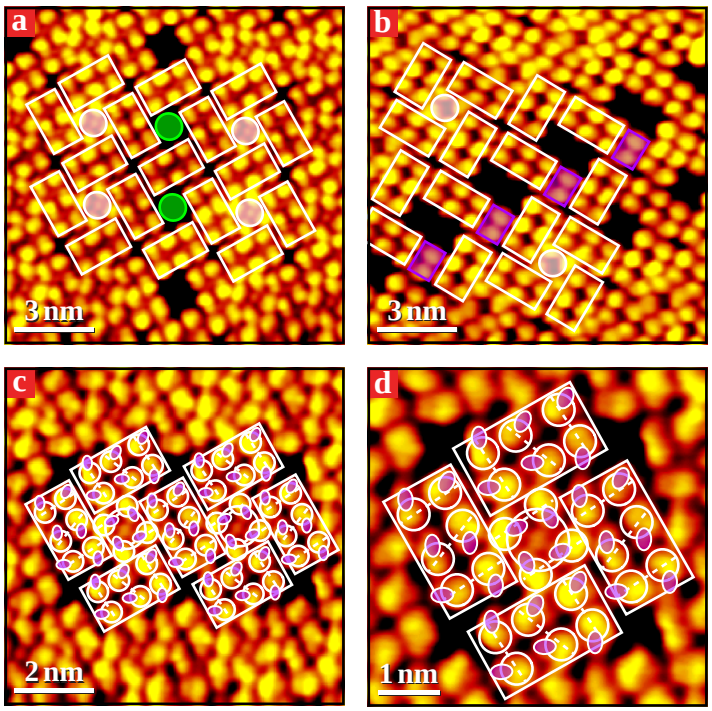

Figure 4.15: High-resolution STM images of the porous windmill pattern formed by KFFE. (a) General arrangement of the tetrapeptides. Each rectangle and circle (node) contains 3 and 2 molecules, respectively. Green disks underline the pores. (b) Defect region in the KFFE windmill network. (c) Submolecular-resolved patterns of different conformers of KFFE. (d) Enhanced representation of the leftmost part of panel (c). Molecular conformers are oriented as indicated by the protrusions labeled in color. KFFE tetrapeptides align antiparallel along dashed lines corresponding to the molecular axes.

formed by 6 protrusions. This indicates that these rectangular blades are built from 3 stacked KFFE peptides. At submolecular resolution in Fig. 4.15c,d it is possible to distinguish the orientation of phenylalanine side chains (in violet). The enhanced representation shows that the F residues located at the nodes are oriented in a clockwise manner with an angle of $\sim 90^\circ$ with respect to each other. In each rectangular frame, the protrusions are also clockwise oriented. Overall, the orientation of protrusions defines a characteristic molecular chiral pattern.

Additionally, for each blade, the backbones of the lowermost (or leftmost) and uppermost (or rightmost) tetrapeptides are almost parallel to each other, while the molecule placed in between has its molecular axis tilted by an angle of 19° with respect to them. A close-up examination of the molecular doublet features forming the nodal pattern reveals the presence of additional periodically repeating circular dimmer protrusions right in the centre of the nodes which are absent in the defect regions. It is unlikely that

they stem from impurities, rather they might originate from an intermolecular interaction occurring at node locations. Furthermore, the two molecules constituting the node structure are images of each other by a 180° rotation. This indicates here a tendency for antiparallel alignment of the two tetrapeptides. On the other hand, it is difficult to tell if peptides are aligned either parallel or antiparallel in the rectangular subunits.

4.5 Conclusion

It was beyond the scope of this chapter to describe the current understanding of all the questions which are related to peptide aggregation and fibrillization. However, substantial progress has been made through this study towards this aim. In the first place, it was shown that tetrapeptides can be deposited onto Au(111) by thermal evaporation conditions without affecting their molecular integrity. Also several outstanding issues have been addressed here using a combination of experimental and computational techniques. Other questions are pending, notably the exact nature of the interpeptide interactions at the surface, but there is strong hope that this work will be soon be followed by other investigations dealing with this issue.

What can be rationalized from this study is that aggregation-preventing mechanisms like conditions of deposition, environment (UHV), molecule-substrate interactions, molecular flexibility, or repulsive interactions between residues, do not impede self-organization of the tetrapeptides at surfaces. This is a very important point in view of the variety of ordered structures that have been described in this chapter. Delimiting the suitable temperature range to succeed self-assembly of tetrapeptides on Au(111) was somewhat difficult. We have endeavoured to do cautious assays in order to avoid degrading the molecules in the harsh UHV STM environment. Once an ideal protocol for evaporation of molecules was assessed the KFFE and KVVE molecules self-organized into extended 2D structures on the Au(111) surface. Respectively two and four motifs were found at monolayer coverage for KFFE and KVVE, and there exists certainly more.

The identification of the tetrapeptide molecules in STM images depends crucially on the tip condition. The STM tip states gave three imaging modes permitting with high confidence to ascribe protrusions to specific residues and to the chain backbone. To single out the individual molecules, we analyzed island edges and structural defects in the images. Molecular orientation could be ascertained from this approach, which led to assignment of bright protrusions to side chains or molecular board. The molecules seem to adsorb preferentially on Au terraces since we did not observe them anchored at steps edges. This has greatly facilitated the determination of the MDFF structure of the peptides. Despite experimental distance restraints are projections of 3D objects onto a 2D surface, molecular assessment of peptides by STM imaging proved to be reliable.

In most cases the Au(111) herringbone reconstruction is resolved underneath extended molecular islands indicating relatively weak peptide-substrate interaction. This indicates that 2D self-assembly of tetrapeptides is mainly stabilized by interpeptide interactions. Restrained MDFF structures of patterns have provided a better understanding of intermolecular interactions. MDFF structural determination with XPLOR software has proven to be very efficient in solving complex protein structures to a good accuracy with faster computation time than ab initio methods. There are some limitations, how-

ever, when applying this technique to STM imaging. For instance molecule-substrate and tip-molecule interaction cannot be implemented. Since the MDFF structure is based on restraints derived from 2D images, subjective restraints relative to the thickness of peptide layers should be arbitrarily introduced.

The restrained MDFF structures reproduce well the so-called parallel and antiparallel row structures of KFFE and KVVE. In the parallel row ordering, analysis indicates that interpeptide H-bonding between parallel molecular backbones is unlikely because of a large interpeptide distance. For KFFE $\pi - \pi$ interaction between F side groups should participate to structural stabilization within rows. The two tetrapeptides yield the same structural motif. Therefore, it can be assumed that glutamate side chains can form H-bonds via head-to-head contacts across the inter-row boundaries. Another interesting result from the structural calculation is the U-shape of KFFE and KVVE monomers at the surface.

MDFF structure of the antiparallel row motif formed by KVVE reveals that peptides adsorb more flat on the surface than KFFE. Inter-row correlations seem strong, enabling H-bonding between oppositely oriented lysine groups of adjacent molecules. Intra-row stacking discloses seemingly an antiparallel alignment of the backbones not due to H-bonding. The adsorption geometry of the KVVE monomer at the surface is distinctly S-shaped.

In summary, a number of inferences concerning interpeptide interactions can be gathered from the experimental and MDFF structural analysis of the tetrapeptide self-assembly at metallic surfaces. H-bonding is supposed to play an important role in the stabilization of the 2D structures. Tetrapeptide self-assembly can form also chiral patterns which may be of interest for biochemistry and pharmacology. It will be relevant in a wider context to figure out how proteins, under physiological conditions, avoid aggregation. To this end, it will be necessary in the future to develop experimental protocols mimicking biological environment for studying peptide aggregation by SPM tools, which have demonstrated here their effectiveness at the atomic scale.

CHAPTER 5

Molecular Self-Assembly on a Thin Insulating Film

Self-assembly of organized molecular structures on insulators is technologically very relevant, but in general rather challenging to achieve due to the comparatively weak molecule-substrate interactions. Here we report on the self-assembly of a bimolecular hydrogen-bonded network formed by Melamine (M) and Cyanuric Acid (CA) on ultra thin NaCl films grown on a Au(111) surface.

5.1 Introduction

Supramolecular structures grown on metallic surfaces have been studied intensely over the last decade, and by means of Scanning Tunneling Microscopy (STM) considerable insight has been gained into mechanisms guiding the self-assembly of molecular nanostructures on surfaces [2, 5, 15]. For certain emerging nanotechnological application areas, such as organic electronics or molecule-based sensing devices, it is however not very desirable to have functional molecular nanostructures adsorbed on highly conductive substrates since the substrate conductivity may often dominate over that of the adsorbed molecules and/or the molecular excitations may be quenched by electronic coupling to the underlying metal substrate. Adsorption of organic molecules on non-conducting substrates is therefore a topic of considerable current interest [68, 69, 123–130]. Surfaces of bulk insulators are challenging to characterize at a microscopic level [131], although recently significant advances in our atomic-scale understanding of these surfaces have been obtained by means of non-contact Atomic Force Microscopy (AFM) [132, 133]. Ultra thin films of insulators on conducting substrates, such as metal oxide or alkali halide films with a thickness of a few atomic layers only, have therefore emerged as an attractive intermediate case that may retain many of the insulators surface characteristics while still allowing flow of sufficient current to enable STM measurements.[66, 70, 130, 134] The growth of NaCl on metallic substrates has thus been reported upon in a number of systems, including Al(111) and Al(100) [66, 135], Ag(100) [136], Cu(100) and Cu(111) [137–141]. For individual pentacene molecules adsorbed on ultrathin films of NaCl it was recently shown that the dielectric spacer layer was sufficient to decouple the molecular electronic structure from the states of the underlying metallic substrate [68, 137]. A very low substrate temperature (~ 5 K) was required in this and related studies [129, 142] to prevent surface diffusion and thus allow STM imaging of individual molecular adsorbates.

Self-assembly of organized molecular structures on insulators is in general rather challenging due to the comparatively weak molecule-substrate interactions, which leads to a high molecular mobility, difficulties in stabilizing 2D molecular nanostructures at moderate temperatures, or formation of 3D clusters even at low coverage of organic molecules [124, 128, 143]. Molecular self-assembly on NaCl has only been studied in a few cases, focusing primarily on adsorption and growth of metal-organic complexes [69, 125–127]. On ultra thin NaCl films, a high surface mobility of molecular adsorbates was observed at low coverage, and stable molecular structures have only been obtained at local coverages close to saturation [69]. Molecular adsorption was found to occur in a hierarchical way where the molecules adsorbed first on the metal substrate, and then on the first, second, and third insulating monolayers of the thin NaCl film, respectively. This directly signals corresponding differences in the molecule-substrate interaction strength for the different substrate layers. On the bulk NaCl surface, it has been shown that defects such as monoatomically deep pits may trap adsorbed molecules [125, 126].

This chapter demonstrates that using STM under UHV conditions it is possible to exploit strong intermolecular forces in the M-CA system, resulting from complementary triple hydrogen bonds, to grow 2D bimolecular networks on an ultrathin NaCl film that are stable at a relatively high temperature of ~ 160 K, and at a coverage below satura-

tion of the first molecular monolayer. In addition, molecular islands formed from CA molecules alone are observed. These hydrogen bonded structures on NaCl are identical to the self-assembled structures observed for the M-CA system on Au(111), which indicates that the molecular self-assembly is not significantly affected by the isolating NaCl substrate.

5.2 Experimental procedure

NaCl was evaporated from a tantalum crucible, wound with a THERMOCOAX heating element and resistively heated to at a temperature of 725 K. The cleaned Au(111) substrate was maintained at a temperature of 300-350 K during NaCl deposition. CA and M molecules were sublimated from separate glass crucibles heated to 355 and 337 K, respectively. Thorough degassing of the NaCl and molecular powders was performed prior to evaporation. The M and CA crucibles were both oriented with their molecular beams focused towards the substrate position, enabling simultaneous or individual deposition of the two molecular species. Some cross-contamination between the two crucibles was observed in the later experimental runs. The NaCl/Au(111) substrate was held at room temperature (300 K) during molecular evaporation. In order to achieve further thermal stabilization of the molecular adsorption structures the sample was subsequently transferred into the cooled STM. Imaging occurred at sample temperatures ranging from 140 to 180 K in the constant current mode ($I_t \sim 0.3$ nA). Bias voltages ($V_t \sim -1.45$ V) are given with respect to the sample. Temperatures were monitored with NiCr/Ni thermocouple pairs. The STM images were calibrated from images of the clean Au(111) surface. In particular, for the step height analysis, the z-piezo scanner was calibrated from analysis of monoatomically high steps of the Au(111) substrate with a nominal height of 2.35 Å. All quoted step heights were determined from STM images recorded in the constant current mode.

5.3 Growth of NaCl on Au(111) substrate

Au(111) is often used as substrate for molecular self-assembly studies, but the growth of NaCl on this surface has not been thoroughly characterized before [144]. An overview of the surface subsequent to growth of the NaCl thin film on the Au(111) surface is depicted in the STM image in Fig. 5.1a where different exposed layers of NaCl are indicated. The thin NaCl islands/films grow with their (001)-surface parallel to the Au(111) surface plane in agreement with previous studies [66, 135–141]. The characteristic height modulation of the Au(111) herringbone reconstruction is visible in STM images of the ultrathin NaCl film indicating that the reconstruction is preserved underneath the film. This suggests that the interaction of the NaCl overlayer with the metallic substrate is relatively weak. The characteristic herringbone reconstruction line structure does not perturb the crystallinity of the NaCl film which is regular as confirmed by the atomic resolution images depicted in Fig. 5.1b. The bright protrusions in the atomically resolved STM images are attributed to chlorine ions in accordance with previous studies[66, 145]. The observed growth of a regular, crystalline NaCl thin film on the corrugated Au(111) surface is not surprising as it is known that NaCl can even cover step edges of an underlying substrate in a carpet-like mode[146] (see Fig. 5.2a). The surface lattice constant of the NaCl film $|\mathbf{a}| = |\mathbf{b}|$ is determined to be (3.83 ± 0.06) Å,

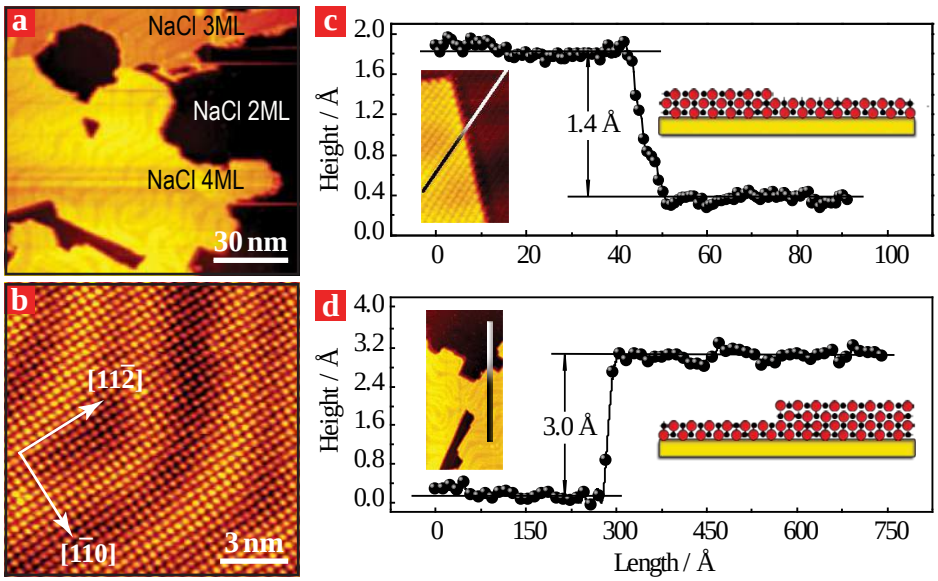

Figure 5.1: Growth of NaCl thin films on Au(111). (a) STM image showing third (3ML) and fourth (4ML) NaCl layers on top of the initial NaCl double-layer (2ML). ($I_t = -0.21$ nA, $V_t = -1.4$ V). (b) Atomically resolved STM image of the NaCl double-layer modulated by the underlying Au(111) herringbone reconstruction ($I_t = -0.26$ nA, $V_t = -1.9$ V). (c) Height profile from the second to the third NaCl layer ($I_t = -0.3$ nA, $V_t = -1.4$ V); (d) Height profile from the second to the fourth NaCl layer ($I_t = -0.22$ nA, $V_t = -1.4$ V).

close to the corresponding bulk value of 3.99 Å [147]. Thus, we conclude that NaCl grows incommensurably on the underlying Au(111) substrate. We observe however that the [100] and [010] directions of the thin film NaCl overlayer are aligned within a few degrees parallel to the [1$\bar{1}$0] and [11$\bar{2}$] directions of the Au(111) surface. A model of the surface unit cell of the NaCl overlayer along with the orientation of the underlying Au(111) substrate is sketched in Fig. 5.2b. The step edges of the NaCl film are preferentially straight and non-polar, i.e. with alternating Na^+ and Cl^- ions, which often leads to rectangular NaCl islands.

Height profiles across various kinds of step edges of the NaCl-covered Au(111) substrate were thoroughly analyzed, and are shown in Figs. 5.1c-d and 5.2c along with schematic models illustrating the proposed step configurations. A portion of the surface exposing both Au and NaCl terrace regions is shown in Fig. 5.2a, and the corresponding height profiles are depicted in Fig. 5.2c. The line scan marked *A* runs over three steps on the surface. The middlemost step is between two terraces of the Au(111) substrate and the measured height of 2.3 ± 0.2 Å agrees with the nominal Au(111) step height of 2.35 Å. For the two adjacent steps, apparent heights of 3.5 ± 0.2 Å were determined. We attribute these steps to double-layers of NaCl on the Au(111) surface in agreement with previous studies [67]. The geometrical height of a NaCl double layer is 5.64 Å, but

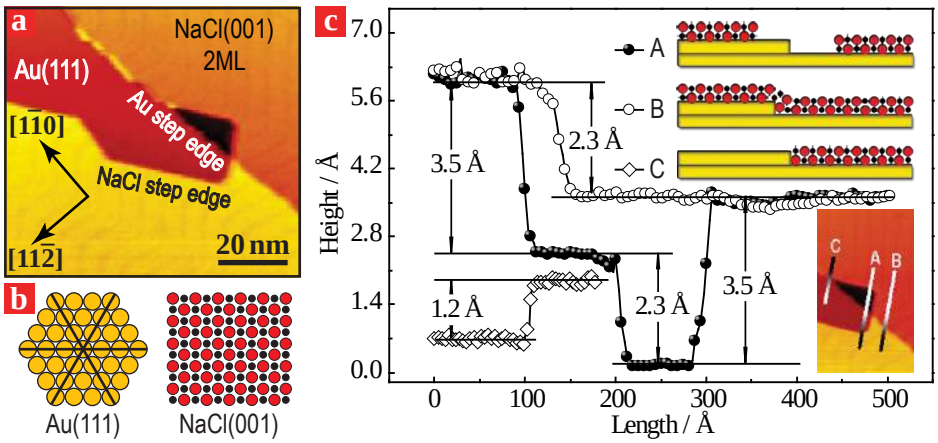

Figure 5.2: Growth of NaCl thin films on Au(111).: (a) STM image of the initial NaCl double-layer on Au(111) ($I_t = -0.2$ nA, $V_t = -1.4$ V). (b) Schematic drawing of the Au(111) and NaCl(001) structures; (c) Height profiles taken over a monoatomic step on Au(111) covered to various degrees by a NaCl double layer as illustrated in the models (see inset for position of line scans).

this geometric height is not expected to be measured in the apparent step height in the STM images due to the different chemical nature and work function of the two adjacent surfaces. (A discussion of chemical versus topographical contrast in STM images can be found in ref.[134]). In particular, due to the insulating property of NaCl, the apparent height measured by STM may be expected to be reduced compared to the geometrical height [66, 67]. Steps of lower apparent height between Au surface and NaCl regions, which could be indicative of monoatomically thick NaCl layers, were not observed. The NaCl islands on Au(111) thus appears to nucleate as a double-layer in the reported temperature regime as was also observed for other metallic substrates [67, 141]. Line scan *B* runs over the NaCl double layer at a position where it crosses a step of the underlying Au(111) substrate, and the measured corresponding step height is 2.3 ± 0.2 Å, in agreement with the height for the monoatomic Au(111) step as determined from line scan *A*. Finally, line scan *C* runs from a Au(111) terrace to a portion of the NaCl film which rests on a lower, adjacent Au terrace, and the apparent height measured for this configuration is 1.2 ± 0.2 Å. In Fig. 5.1c the apparent step height for a 3rd layer NaCl on top of a NaCl double layer island is determined to be 1.4 ± 0.2 Å. Occasionally, we also observed double-layer steps of NaCl on top of double-layer islands, as depicted in Fig. 5.1d, with an apparent step height of 3.0 ± 0.2 Å [141].

5.4 Self-assembly of M and CA on NaCl/Au(111)

Co-deposition of CA and M molecules was performed on the Au(111) surface partially covered with ultra thin NaCl islands/films as described above. This typically resulted in molecular adsorption structures on the Au(111) surface (Fig. 5.3a), which were identical to the self-assembled molecular rosette patterns reported upon previously for the

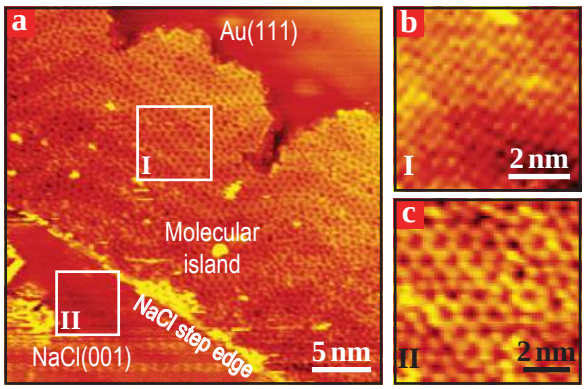

Figure 5.3: Molecular islands on partially NaCl-covered Au(111) surface. (a) Nucleation of the molecular CA_1M_1 layer from the NaCl-covered Au(111) step edges with subsequent growth on Au(111) substrate. Panels (b) and (c) show enhanced representations of the molecular structure on Au(111) indicated by frame I and the NaCl-covered region marked II, respectively.

M-CA system on Au(111) [25]. Nucleation of these molecular nanostructures occur preferentially at ascending step edges of Au(111) and in particular at NaCl island edges, and is followed by growth of molecular islands on top of Au(111) terraces next to the Au(111)/NaCl step edges. Adsorption of molecules on metallic Au(111) is thus favored compared to adsorption on regions of NaCl thin film (Fig. 5.3b and c), in agreement with the hierarchical adsorption behavior observed previously in another molecule-insulator-metal system [69].

Self-assembled CA-M adsorption structures were however also successfully stabilized on top of the ultrathin insulating NaCl film. Fig. 5.4a displays an area of the surface with three NaCl terraces of different heights exposed. Atomic resolution in the upper-left and lower-right parts of the image clearly identifies these regions as NaCl. Adjusting the colour scale in the central part of the STM image allows the square symmetry characteristic of the NaCl(001) surface to be observed also here (see Fig. 5.4b). The line scan marked *A* running across the terraces reveals step heights of 1.3 ± 0.2 Å and 3.2 ± 0.2 Å (see Fig. 5.4c) which are in good agreement with those reported in Fig. 5.1c and d for step heights of a monatomic and a two-atomic NaCl step on a double-layer of NaCl, respectively. We therefore conclude that this is an area of the surface which was entirely covered by NaCl prior to molecular deposition and we propose a schematic model of the different exposed layers as illustrated in Fig. 5.4c. Co-deposition of M and CA molecules on this substrate led to formation of the molecular nano-structure visible in the bottom part of Fig. 5.4a, which grows from the double-layer step edge of the NaCl film and terminates on the NaCl terrace. The apparent height of the molecular layer on top of a double-layer NaCl thin film is 1.4 ± 0.2 Å as determined from the line scan *B*. High resolution STM images of the molecular adsorption structures are shown in Fig. 5.5a. The left part of this STM image shows a terrace covered by a NaCl thin film, as evidenced by the enhanced representation of the region I shown in Fig. 5.5b. To the

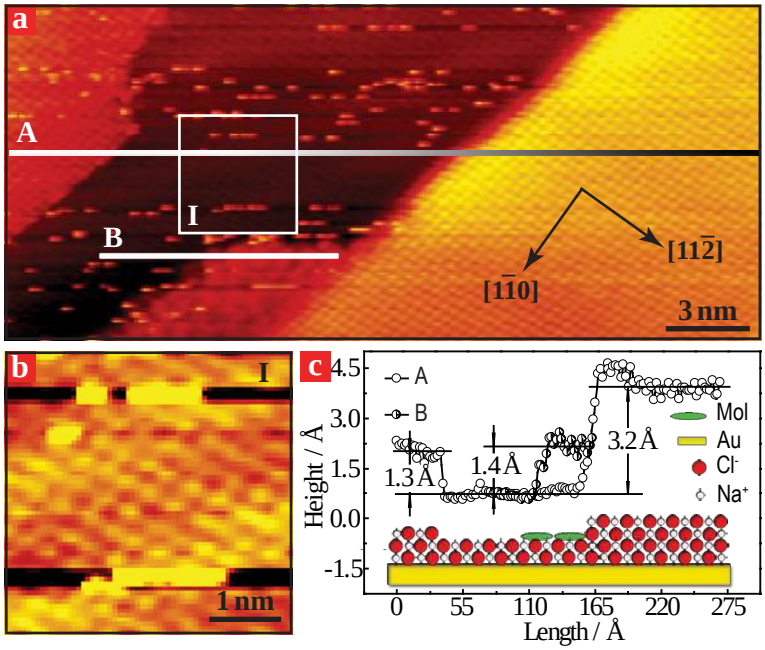

Figure 5.4: Molecular island on top of a NaCl thin film. (a) STM image showing three exposed layers of NaCl and a M-CA molecular island in the bottom portion of the central terrace. ($I_t = -0.35$ nA, $V_t = -1.49$ V). (b) Enhanced representation of the region of the NaCl substrate indicated by frame I. (c) Height profile across the NaCl terraces (line *A*) and the molecular island (line *B*) along with a schematic model of the structure.

right side of the image the surface is covered by a molecular adsorption structure. In the region marked II, which is shown enhanced in Fig. 5.5c, the structure is regular and similar to the characteristic rosette pattern obtained for CA and M at 1:1 stoichiometry on pure Au(111)[25] (see also Fig. **??**b, c). Other parts of the structure are less regular but display local order in the molecular arrangements. A height profile taken along the line indicated in Fig. 5.5a is shown in Fig. 5.5d. The apparent height of 1.5 ± 0.2 Å for the leftmost step is equal to the height difference between a NaCl surface and a molecular adlayer located on top of it as determined from Fig. 5.4. The rightmost step has an apparent height of 2.4 ± 0.2 Å which corresponds well to the height of a step on the Au(111) surface, but differs significantly from the observed heights of single and double layer steps of NaCl (see Fig. 5.1). These observations are consistent with the model displayed in Fig. 5.5d in which molecular structures are stabilized on NaCl covered terraces and grow from both sides of a NaCl-covered monatomic Au(111) step edge.

Direct evidence for adsorption of CA and M molecules on top of the ultrathin insulating NaCl film is provided by Fig. 5.6a. This STM image, which was scanned from bottom to top, exhibits three distinct regions, marked α, β and γ, respectively. The bottommost α region displays a well-resolved NaCl structure. In the central region

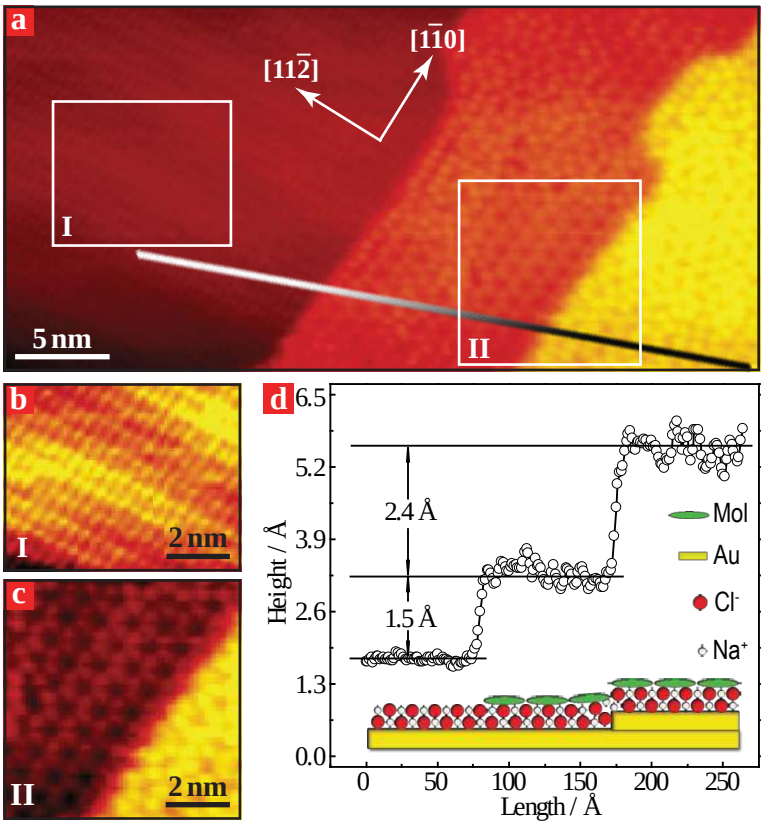

Figure 5.5: Highly resolved M-CA structures on NaCl/Au(111) thin films. (a) STM image showing both NaCl and M-CA regions ($I_t = -0.4$ nA, $V_t = -1.44$ V). (b) Enhanced representation of the NaCl-covered region marked I. (c) Enhanced representation of the molecular structures in the region marked II which also contains a step edge. (d) Height profile taken along the line indicated in panel (a) with corresponding schematic model of the structure.

(β), the resolution is somewhat limited, but a square symmetry similar to the one observed for atomic resolution of NaCl is still clearly apparent. However, between the β and γ regions a sudden change in the imaging conditions occurs such that a molecular structure is clearly resolved in the uppermost γ region. This structure is identical to the rosette pattern observed previously for a 1:1 stoichiometry of CA and M on pure Au(111)[25] and consists of molecular entities with near-circular and 3-fold symmetric appearance, which are attributed to CA and M molecules, respectively. For comparison, an hydrogen-bonding model of the adsorption structure formed on Au(111) and STM image is shown in Fig. **??**b and c. As the molecules in the γ region are revealed by a sudden change in the tip state, we conclude that also in the β region there are molecules adsorbed on the substrate, but they are not visible in the STM images due to a particular state of the STM tip which instead probes the underlying substrate, allowing it to be

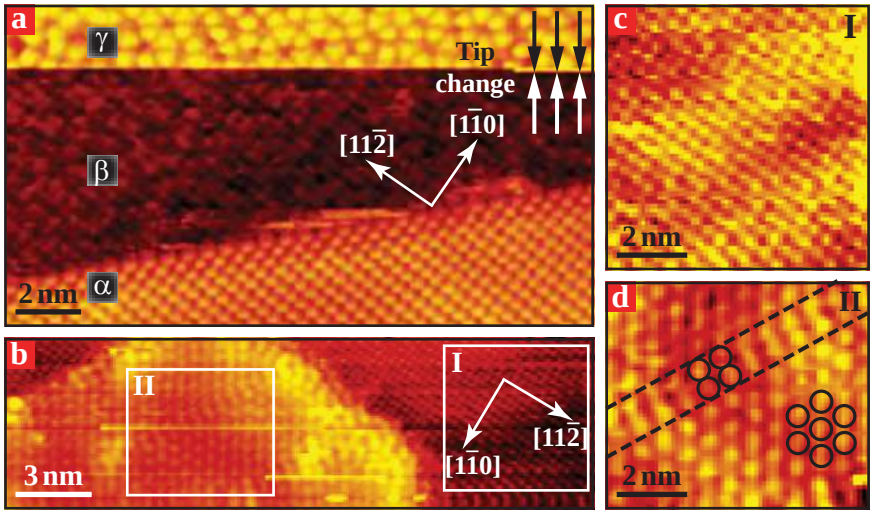

Figure 5.6: Direct evidence of a M-CA rosette structure formed on a NaCl/Au(111) thin film. (a) STM image showing both NaCl (α) and M-CA (β and γ) regions. A spontaneous change in the state of the STM tip allows the molecules to be imaged at high resolution in the region. ($I_t = -0.37$ nA, $V_t = -1.4$ V). (b) STM image of an island formed from CA molecules ($I_t = -0.32$ nA, $V_t = -1.49$ V). (c) enhanced representation of the portion of the NaCl surface marked I. (d) enhanced representation of the region marked II with circles drawn to indicate positions of individual CA molecules.

identified as NaCl. The nature of the tip change providing molecular resolution is unknown, but we speculate that it may be caused by the attachment of a molecule to the tip apex, which has previously been shown to significantly enhance the resolution of molecules adsorbed on thin insulating films [68]. The transition from the α to the β region is attributed to a step of the underlying substrate either from 3rd layer NaCl to an adjacent double-layer region or over a step of the Au substrate covered by a double-layer NaCl in the carpet-like mode. The measured apparent height of the step between the α and β regions is approximately 1.8 Å but is difficult to interpret due to the particular tunneling conditions and different surface chemistries at the two sides of the step. A slight shift in the registry of the protrusions attributed to Cl^- ions between the two terraces suggests however, that the step consists of a single layer of NaCl.

In situations with a stoichiometric excess of CA molecules, we observed an additional structure as illustrated in Fig. 5.6b. Here, the molecular features form a close-packed hexagonal structure with a lattice vector of 7.1 ± 0.1 Å. In the region between the dashed lines on Fig. 5.6d a domain wall leads to a square molecular arrangement. These molecular structures are identical to those observed previously for CA molecules adsorbed on the Au(111) surface [25] and are therefore attributed to this compound alone. Interestingly, the hexagonal CA structure stabilized by NH$\cdots$O hydrogen bonds is expected to be less strongly bound than the M-CA rosette structure [25] but the intermolecular interaction is nevertheless sufficient to stabilize it also on the NaCl substrate.

5.5 Conclusion

In summary we have investigated the growth of supramolecular structures on an ultrathin film of NaCl grown on Au(111). The comparatively strong intermolecular interactions in the M-CA co-adsorption system, resulting from complementary triple hydrogen bonds, is found to be sufficient to stabilize organized, 2D molecular structures at relatively high temperatures of 160 K and at sub-saturation coverages. The characteristic M-CA rosette structure observed previously on Au(111) is found also on the NaCl substrate, signaling a minor influence of the insulating substrate on the molecular assembly. The ability to grow and stabilize organized molecular structures on insulators or thin insulating films is important for future efforts towards characterizing and utilizing the electronic properties of functional supramolecular assemblies.

CHAPTER 6

Hydrogen bond induced structures of Lander molecules

Molecular Landers are a class of organic compounds in which a central aromatic board is lifted up and then decoupled from the underlying substrate via bulky spacer groups. They have attracted considerable attention due to their ability of trapping and "moulding" metal atoms into metallic nanostructures in the cavity beneath the aromatic board. However, except poorly ordered short Lander chains, attempt to form 1D assembly of the Lander moulds has only succeeded when applying special templates which unfortunately limits future applications. This chapter presents several STM studies concerning the deposition and codeposition of two Lander molecules specially designed and synthesized with groups enabling specific H-bond interaction. It is shown that the compounds can form extended 1D or 2D self-assembled structures not only on their own but also together when codeposited on Au(111). These intriguing findings are explained by strong H-bonding interactions between the functionalized groups of molecules.

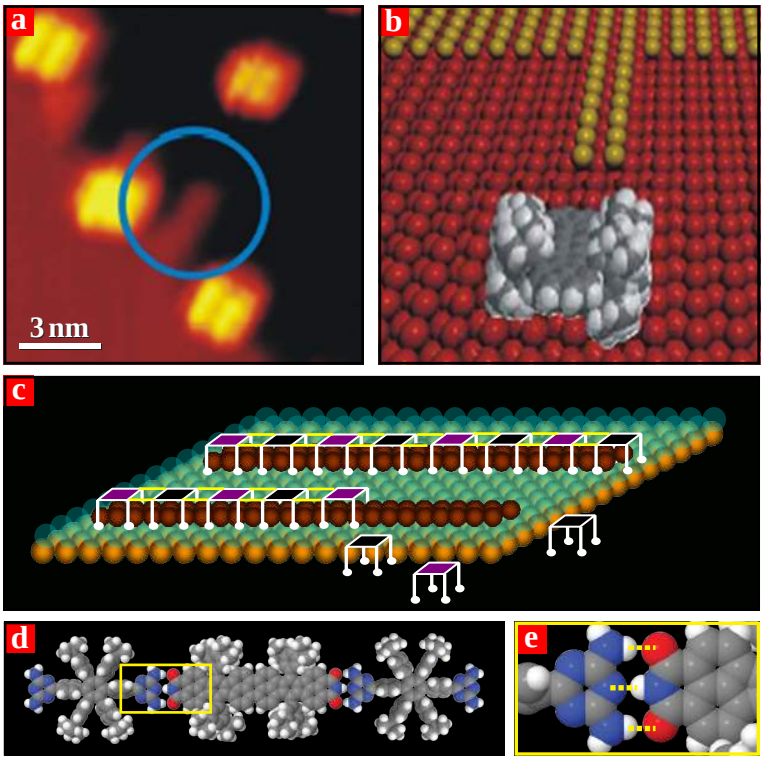

Figure 6.1: Self-assembly of molecular moulds. (a) STM image of an atomic wire (blue circle) grown by a Lander molecule (upper right). (b) Artistic view of this image, adapted from Ref. [155]. (c) Sketch of 1D metallic wires (dark brown) grown by alternating A-B-A-B molecular Lander chains (black and purple) with lifting legs through H-bonding (yellow lines).(d,e) Tentative models of the chains formed by complementary triple hydrogen bonds.

6.1 Introduction

The need to overcome the barriers in the miniaturization of electronic devices has led to the development of new alternatives to conventional semiconductor techniques [4]. One of the most promising approaches to build highly-ordered nanoarchitectures on a large scale is self-assembly of atoms and molecules adsorbed on surfaces [148]. This approach largely contributes to all fields of the rapidly growing area of nanotechnology such as sensors, molecular electronics, solar cells, etc.

Applications in molecular electronics require the synthesis of sufficiently rigid molecules capable to maintain the desired nanoarchitecture. Additionally, the functionalised part of these molecules should be planar to promote formation of long-range ordered structures on surfaces while the backbone should be electronically decoupled from the underlying metal substrate. These requirements are fulfilled by the so-called Lander family, also known as molecular wires [149–151]. Lander molecules consist of a rigid

polyaromatic board which is separated from the metal surface by bulky spacer groups acting as legs. UHV STM has given opportunity to study various properties of single Lander molecules adsorbed both at step edges and terraces like for instance conformational changes, conductance, electronic contacts with metallic nanopad, diffusion, and tip manipulations [152–154].

A particular fascinating property of single Lander molecules adsorbed at step edges or to a lesser extent on terraces is their ability to induce reconstruction of the underlying metal substrate (see Fig. 6.1a,b) which is commonly referred to as the "molecular moulding" effect [155, 156]. It was recently shown that four- and six-legged Lander molecules are capable of forming well-defined metallic nanostructures either spontaneously by trapping diffusive adatoms in the cavity underneath the aromatic board or deliberately by STM manipulation of the molecular mould [155, 157]. The controlled self-assembly of Lander molecules on surfaces is therefore attractive for fabricating conductive metallic nanowires or nanoarrays which might be applied for nanoelectronic circuitry.

There have been few reports concerning STM investigations of extended ordered nanostructures of Lander molecules at metallic surfaces [158–163]. Formation of extended 1D Lander molecular chains on terraces was observed only on special surfaces such as alternating Cu-O/Cu templates, while small 1D segments were found on the Cu(100) substrate [159, 160]. Similar structures were detected on the terraces of Cu(111) substrate and at steps of both Au(111) and Ag(111) surfaces but they were not thoroughly characterized [158]. Observations of 2D ordered structures of Lander molecules on metal substrates are also scarce and concern the formation of molecular domains on Cu(110) and Cu(111) surfaces [162, 163]. The intermolecular interactions responsible for these 1D and 2D structures was assigned mainly to van der Waals forces. Since the formation of these structures relies on either a very special choice of substrate or intermolecular interaction it is desirable to explore the self-assembly governed by more versatile noncovalent bonding such as the H-bond.

Intermolecular hydrogen bonding plays an essential role in molecular self-assembly because of strong spatial selectivity and directionality. H-bonded architectures formed by small molecules adsorbed directly on metal surfaces have been extensively studied in the past years. However, there is a lack of data concerning the fabrication of extended Lander molecular nanostructures stabilized by hydrogen bonding onto surfaces [13].

The main goal of the present work will therefore to form self-assembled structures of molecular moulds by optimizing the molecule-molecule interaction. To this end, two new Lander-type species bearing complementary di-carboxylic imide (DCI) and diamino-triazine (DAT) functional end-groups have been synthesized [164] which will be hereinafter referred to as Lander-DCI and Lander-DAT molecules (see Figs.62a and 63a). It has recently been shown that melamine and cyanuric acid molecules can form self-assembled networks through triple hydrogen bonding provided by these functional groups [25]. Guided by this, it is expected that with these novel Landers it will be possible to grow one-dimensional wires of alternating DAT-DCI-DAT-DCI molecules which interact through complementary triple H-bonding. If so, the known moulding property of the Lander family of molecules is envisioned to be used for fabrication of long 1D metallic nanowires on the metal substrate by trapping diffusing metal adatoms

under the molecules, eventually realising structures of the type schematically shown in Fig. 6.1c. Once the metallic nanostructures can be grown with confidence, it will be possible to extend the ongoing studies to insulating films which are more relevant substrates for molecular moulding of metallic wires.

The results presented in this chapter constitute the first step towards this challenging project. The two Lander species were deposited onto the Au(111) *metallic* surface. A stimulating observation is that each compound can self-assemble into long 1D chains. Lander-DAT additionally forms a number of 2D structures. Finally the codeposition of Lander-DCI and Lander-DAT has been carried out onto the same surface, and results into 1D and 2D hetero-molecular structures.

6.2 Molecular systems

6.2.1 Lander-DCI molecules

Lander-DCI ($C_{112}H_{102}N_2O_4$) is a derivative of the violet Lander (VL) $C_{108}H_{104}$ and, as a consequence, consists of a central polyaromatic π-system equipped with four σ-bonded 3,5-di-*tert*-butyl-phenyl (DTP) substituents which serve also as spacer legs. To enhance intermolecular interaction the molecular core was functionalized by adding dicarboxylic imide (DCI) terminations enabling hydrogen bonding (Fig. 6.2a,b). A high-resolution STM image of a single Lander-DCI on Au(111) shown in Fig. 6.2c reveals four bright lobes disposed in a $\sim$12.5 Å$\times$11.5 Å rectangular arrangement. This STM feature is similar to that reported for other Lander molecules [154, 155, 165]. Fig. 6.2d shows a calculated STM image of an adsorbed Lander-DCI molecule in the optimized configuration illustrated in Fig. 6.2e,f. From the calculated image, the four bright protrusions can be ascribed to the tunnelling through the DTP groups. The central molecular board is not directly visualized in either the experimental or calculated STM images. This is because the tail of the tunnel resonance spanned at the used bias voltage is coming from molecular orbital states with a large weight located on the four DTP legs. Furthermore, the width of those resonances is enlarged by the fact that at a given tip height, the tip apex end atom is better electronically coupled to the top part of the legs than to the DCI central board.

Due to the flexible σ-bonds of DTP groups and to the strong interaction between the aromatic backbone and the metal, the molecule adopts several conformations on the surface. The molecule can stand with legs either parallel or crossed.Simulations of the Lander-DCI in these different configurations demonstrate that the parallel-legs conformation accounts better for the experimental data (Fig. 6.2e). According to the side-view of this simulation the central board is lowered to a height of 3.8 Å above the surface resulting in a bending of the σ-bonds (Fig. 6.2f).

Thermal sublimation of organic compounds of this size, in particular with directional intermolecular interactions, is highly challenging and entails a risk to fragment the compound. However, the good agreement between calculated and experimental STM images strongly support that the observed Lander-DCI molecules are adsorbed intact on the surface.

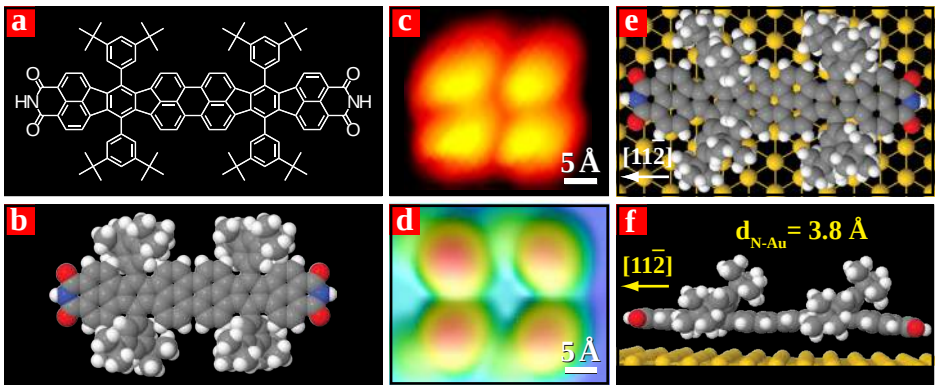

Figure 6.2: (a) Chemical structure of Lander-DCI ($C_{112}H_{102}N_2O_4$). (b) Corresponding space-filling model where C, H and N atoms are represented in gray, white and blue, respectively. (c,d) High-resolution STM image of a single Lander-DCI on Au(111) and corresponding EHMO-ESQC calculated image, respectively ($I_t = 0.26$ nA, $V_t = 1239$ mV). (e,f) Space-filling models of Lander-DCI on Au(111) substrate with molecular board long axis oriented along the [11$\bar{2}$] direction (top and side views)

6.2.2 Lander-DAT and ND molecules

Lander-DAT ($C_{64}H_{68}N_{10}$) is derived from hexa-*tert*-butyl-hexaphenylbenzene (HB-HPB) molecule, and consists of a hexaphenyl benzene (HPB) core terminated at both ends by a diamino-triazine (DAT) functional groups to foster intermolecular hydrogen bonding interaction. In order to lift the molecular board above the surface four σ-bonded *tert*-butyl groups are laterally attached (Fig. 6.3a,b). This molecule is revealed in high-resolution STM image (Fig. 6.3c) as four bright protrusions surrounding a dim central part corresponding to the HPB core. The four bright lobes arranged in a rectangular manner (11.6 Å$\times$6.7Å) are assigned to the *tert*-butyl groups due to a high electron tunnelling probability through the spacer legs into the metal substrate. The dimmer sub-protrusions in the centre can be attributed to the hexaphenyl benzene (HPB) core, similar to that observed earlier for HB-HPB molecule [157, 163]. Strikingly, there is no signature of the two DAT groups in STM image. Notice that the evaporation of large and complex compounds involves a risk of thermal decomposition of the molecular building blocks if the intermolecular cohesive strength in the molecular source material exceeds the intramolecular binding energy. Therefore, the absence of DAT contribution into the STM image could basically lead to the conclusion that the functional groups have been lost during the thermal sublimation of the compound onto the surface.

In view of this, EHMO-ESQC calculation method was used to confirm the image interpretation and demonstrate whether the molecules adsorb intact on the surface. Firstly, molecular mechanics calculations have been performed to ascertain the conformation of the Lander-DAT molecule in Fig. 6.3c. They revealed that Lander-DAT has high conformational flexibility with respect to most planar compounds adsorbed directly onto the surfaces so far. Indeed, the bulky *tert*-butyl spacer legs induce a lift-up of the central

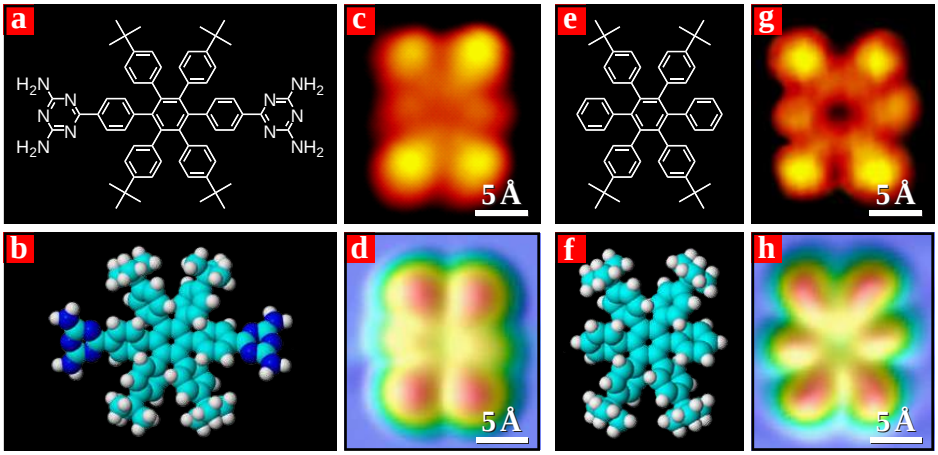

Figure 6.3: (a,e) Chemical structure of Lander-DAT ($C_{64}H_{68}N_{10}$) and Lander-ND ($C_{58}H_{62}$) molecules. (b,f) Space-filling models, where C, H and N atoms are represented in cyan, white and blue, respectively. (c,g) A high-resolution STM image of a single Lander-DAT ($I_t = 0.32$ nA, $V_t = 1487$ mV) and Lander-ND ($I_t = 0.31$ nA, $V_t = 1250$ mV) on Au(111). (d,h) EHMO-ESQC simulated images of Lander-DAT and Lander-ND on Au(111) under the same tunneling conditions as in panel (c) and (g), respectively.

Lander board to an adsorption height of 4.5 Å while the two DAT functional groups are not parallel to the surface plane but slightly tilted with an angle of about 30°. Thus, the closest and the furthest amino-groups nitrogen atoms are at 3.1 Å and 5.2 Å above the surface plane respectively. Using the optimized Lander-DAT adsorption conformation and at a bias voltage lower than the HOMO-LUMO gap of the molecule, a calculated STM image (Fig. 6.3d) under the same tunneling conditions as in Fig. 6.3c was obtained. This calculated image shows that the peripheral DAT groups contribute weakly to the STM image while the four legs are highly transparent to the tunneling electrons. This is consistent with the experimental result. However, under some special tip conditions it is possible to capture in the STM images some features associated with the DAT groups.

To experimentally address the issue of possible fragmentation of the Lander-DAT during thermal sublimation, the Lander-ND ($C_{58}H_{62}$) has synthesized and investigated for comparison. From chemical structure and the space-filling model of Lander-ND shown in Figs. 6.3e and 6.3f, it has the same structure as Lander-DAT except that the DAT end-groups have been removed. A high-resolution STM image of an individual Lander-ND molecule on Au(111) is displayed in Fig. 6.3g, showing a morphology similar to that of Lander-DAT in Fig. 6.3c. By using the ESQC approach, a calculated STM image of a fully relaxed molecule on the surface is shown in Fig. 6.3h, which is consistent with the experimental results. Similarly to the case of Lander-DAT, the four bright lobes arranged in the rectangular shape (11.0 Å × 6.5 Å) were attributed to the four *tert*-butyl groups, and the sub-protrusions in the centre to the HPB core.

6.3 Experimental procedure

The Lander-DCI and Lander-DAT molecules were synthesized by the methods described elsewhere [164]. Thorough degassing of molecular powders was performed prior to evaporation. Thermal sublimation of the DCI and DAT Landers onto the Au(111) surface was carried out under ultrahigh vacuum conditions from the glass crucible resistively heated to 690-710 K and 530-540 K, respectively. The Lander-ND molecules, used for comprison purpose, were evaporated on the same substrate at 465 K. The self-assembly is achieved by depositing the compound onto a substrate kept at 170-220 K, followed by annealing at 400 K for 10 min to allow molecular mobility and then cooling to 170 K to stabilize the resulting structures. All presented STM images were recorded in the constant current mode in a temperature range of 110-170 K, and calibrated from images of the clean Au(111) surface. Attentive survey of the surface did not disclose any hint for molecular fragments. Simulations of STM images were performed using extended Hückel molecular orbital-elastic-scattering quantum chemistry (EHMO-ESQC) [75] after having relaxed the molecule on the surface with the molecular mechanics MM4 (2003) code [166].

The sample preparation procedure for codeposition of Lander-DCI and Lander-DAT was the same. The cleaned Au(111) substrate was maintained at a temperature of 220 K during deposition of molecules. Lander-DAT and DCI molecules were thermally sublimated from separate glass crucibles resistively heated to 543 and 700K, respectively. The codeposition of these molecules was followed by immediate annealing at 400K for 10 min. The molecular coverage of the surface was controlled by evaporation times in the range 2-5 min and 10-20 min for Lander-DAT and Lander-DCI, respectively. STM imaging occurred at sample temperatures ranging from 110K to 160 K. Attentive survey of the surface did not disclose any hint for molecular fragments.

6.4 Self-assembly of Lander-DCI

In this section, the self-assembly of Lander-DCI on the inert Au(111) surface is described. It is shown that Lander-DCI sparsely adsorbed on surface can form highly ordered 1D and 2D nanoarchitectures. The structural analysis reveals that the growth of 1D chains of such large molecules with spacer legs on a metallic surface is directed by specific intermolecular coupling such as H-bonding, while the alignment of the molecular chains is guided by the molecule-substrate interaction.

STM images of 1D chains formed from Lander-DCI molecules at low coverage are presented in Fig. 6.4. These chains can extend to more than 70 nm as revealed from the large-scale image in Fig. 6.4a. The enhanced representations of a single chain shown in Fig. 6.4b disclose that adjacent molecules are arranged in head-to-tail fashion with their long axis essentially along the chain direction. Besides the shown molecular chains formed on terraces, there are also long chains aligned at the step edges as depicted in the high-resolution image in Fig. 6.4e. A model of the Lander-DCI chains adsorbed both on terraces and at step edges is proposed in Fig. 6.4c. The DCI groups on adjacent molecules interact through formation of double N-H$\cdots$O hydrogen bonds as indicated by the yellow dashed lines in Fig. 6.4d. The measured periodicity along the chains is 31.3$\pm$2.0 Å, which is consistent with a reasonable N-H$\cdots$O bond length of $\sim$3 Å given

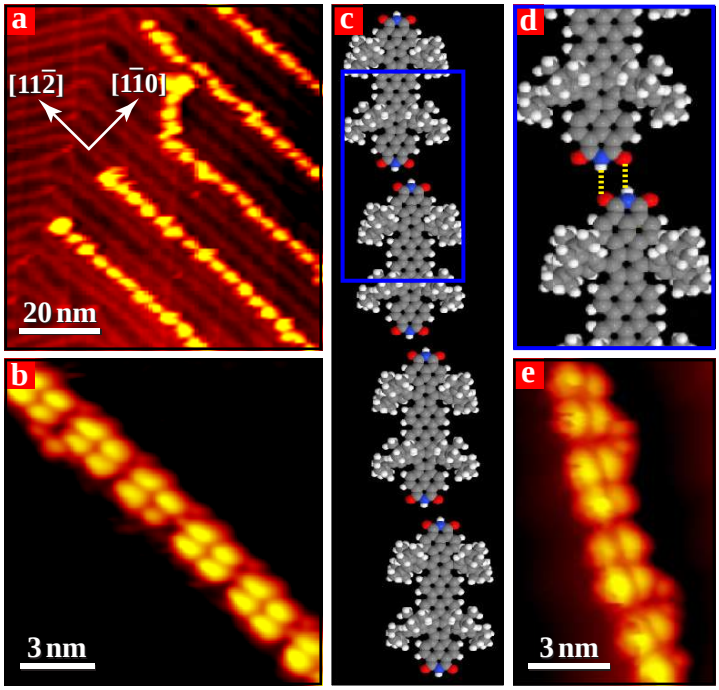

Figure 6.4: Lander-DCI 1D chains. (a) Large scale STM image of 1D chains aligned on reconstructed Au(111) terraces ($I_t = 0.55$ nA, $V_t = 1250$ mV). (b) Enhanced representation of a single chain on Au(111) terraces ($I_t = 0.26$ nA, $V_t = 1239$ mV). (c) Chain model, showing a double N-H$\cdots$O hydrogen bonding between neighbouring Lander-DCI. (d) Zoom-in of the blue frame in panel (c), where the N-H$\cdots$O hydrogen bonds are indicated by the dashed yellow lines. (e) An STM image of a chain at the step edges of the Au substrate ($I_t = 0.43$ nA, $V_t = 1250$ mV).

the distance of $\sim$29.0 Å between the two N-H groups of a Lander-DCI molecule. The same hydrogen bonding motif as shown in Fig. 6.4d has been reported for 2D surface assemblies of the planar aromatic compound perylene-3,4,9,10-tetra-carboxylic-diimide (PTCDI) where the conjugated board is adsorbed directly on a Au substrate [167]. Recent theoretical calculation for a gas-phase dimer of cyanuric acid reported that the stabilization energy of such double N-H$\cdots$O hydrogen bonds has a relatively high value of approximately 0.54 eV [25].

As shown in Fig. 6.4a the chains are oriented along the $\langle 11\bar{2} \rangle$ directions and typically follow the ridges of the herringbone reconstructed Au(111) substrate. In the present STM experiments, chain distortions and motions can be observed when scanning at a higher temperature of $\sim$220 K, under which condition the Lander-DCI molecules have a relative high mobility on the Au(111) substrate, as illustrated in Fig. 6.5. The lower right end of the shown chain is anchored to a step edge and remains oriented along the $\langle 11\bar{2} \rangle$ direction. In contrast, the opposite end of the chain, which resides on a terrace, is free and can move to either side of the original chain direction while the chain

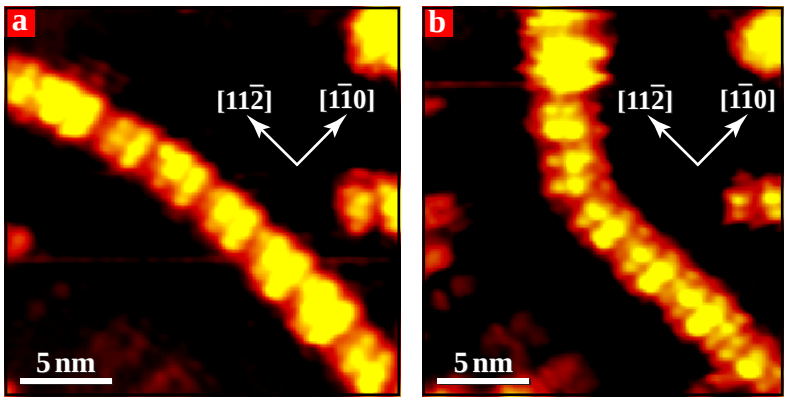

Figure 6.5: Consecutive STM images showing the dynamic behavior of the 1D chains of Lander-DCI at 220 K ($I_t = 0.56$ nA, $V_t = 1250$ mV, with a time lapse between images of 10 seconds). (a) The lower right end of a Lander-DCI chain attached to the step edge of Au(111) substrate keeps a [11$\bar{2}$] orientation, while the left end is slightly bent down.(b) The left end has moved considerably upwards in the image, while the chain remains intact.

remains intact, as shown by the consecutive STM images in Fig. 6.5a and Fig. 6.5b. This demonstrates that the intermolecular hydrogen bonds dominate the formation of the Lander-DCI chains while the molecule-substrate interaction primarily contributes to alignment of the resulting chains on the surface, mainly through direct contact of the DTP groups with the substrate.

At higher coverage, the 1D chains are observed to pack sideways into belt-like structures as shown in Fig. 6.6a. With increasing coverage, these belts further broaden into extended 2D domains, which are most likely stabilized by intermolecular van der Waals forces (see Fig. 6.6b,c).

6.5 Self-assembly of Landers DAT and ND

This section is devoted to the self-assembly of newly designed Lander-DAT molecules into nanostructured architectures on Au(111) surface. By tuning the deposition conditions, both one-dimensional and two-dimensional assemblies of these molecular building blocks have been formed on Au(111) substrate under UHV conditions, and characterized by the variable-temperature Aarhus STM at sub-molecular resolution. For the first time, extended 2D supramolecular networks with molecular board maintained above the metal substrate by organic spacer legs are realized. The formation of four distinct long-range ordered 2D molecular structures are governed by intermolecular N-H$\cdots$N hydrogen bonding. Both experimental results and theoretical calculations demonstrate that the conformational flexibility of the compound bestowed by the high degree of freedom of the DAT groups offer opportunity to optimize this hydrogen bonding in three-dimensions. In addition, the self-assembly of Lander-ND molecules, i.e. Lander-DAT without diamino-triazine functional end-groups, has been investigated for comparison.

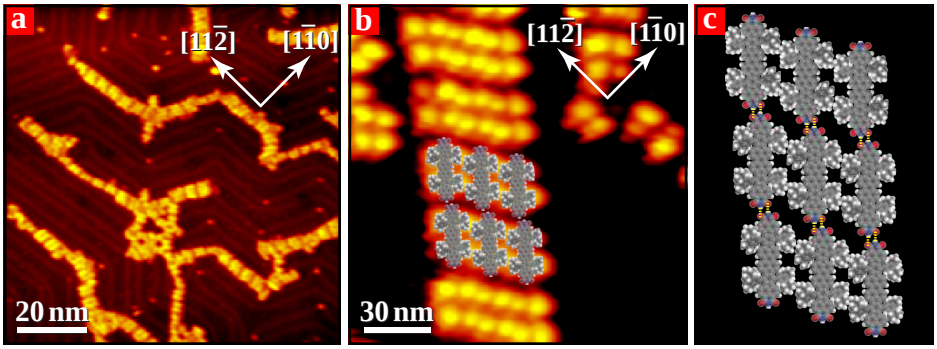

Figure 6.6: (a) An STM image of belt-like structures of Lander-DCI at high coverage ($I_t = 0.52$ nA, $V_t = 1250$ mV). (b,c) 2D domain formed by 3 belts with corresponding space-filling model.

6.5.1 Anticipated interaction of Lander-DAT

According to the knowledge of hydrogen-bonded networks of melamine molecules [25, 168–170] and molecules with DAT functional groups [171] two possible arrangements of Lander-DAT building blocks are anticipated and referred to as "*sideways*" (Fig. 6.7a) and "*head-to-tail*" (Fig. 6.7b) couplings. In both cases, the molecules are not aligned on a straight line but adopt a zig-zag stripe arrangement with each molecule tilted away from the stripe axis to facilitate the intermolecular double N-H$\cdots$N hydrogen bonds indicated by yellow dashed lines in Figs. 6.7a,b. Using the MM4 (2003) code25 two optimized hydrogen-bonded couplings of Lander-DAT have been obtained after molecular system relaxation. The first configuration shown in Fig. 6.7c is in accordance with anticipated "*sideways*" coupling. The detailed hydrogen bonding interaction is depicted in the enlarged section in Fig. 6.7e by two dashed yellow lines. The MM4 relaxed results indicate that the N-H$\cdots$N hydrogen-bond length and angle are 2.89 Å and 146°, respectively. The periodicity of a stripe in the "*sideways*" coupling is 17.0 Å, with the molecular axis (the line across the centers of both DAT end-groups and the molecular core) tilted 19° away from the stripe orientation. The second arrangement is a nearly straight-row configuration referred to as "*head-on*" coupling (see Fig. 6.7d), which differs from the zig-zag "*head-to-tail*" interaction in Fig. 6.7b. The intermolecular distance in the second case is 20.1 Å with the molecular axis tilted by 5° relatively to the row. Therefore, compared to this "*head-on*" coupling, the "*sideways*" configuration is more condensed, with a shorter periodicity (17.0 Å vs 20.1 Å) and a larger rotation angle of each molecule relatively to the stripe axis (19° vs 5°).

For both molecular arrangements, the neighbouring DAT groups are not planar but rotated by a certain angle respectively to each other. In the "*sideways*" configuration, the angle between the two interacting DAT groups is about 139° as shown in Fig. 6.7f. This rotation effect of DAT groups is more pronounced in the "*head-on*" coupling since neighbouring DAT groups form an angle of 75° with respect to each other. The rotation allows forming four N-H$\cdots$N hydrogen bonds by sharing N atom of one DAT group with two NH moieties of contiguous/adjacent DAT group, as demonstrated in

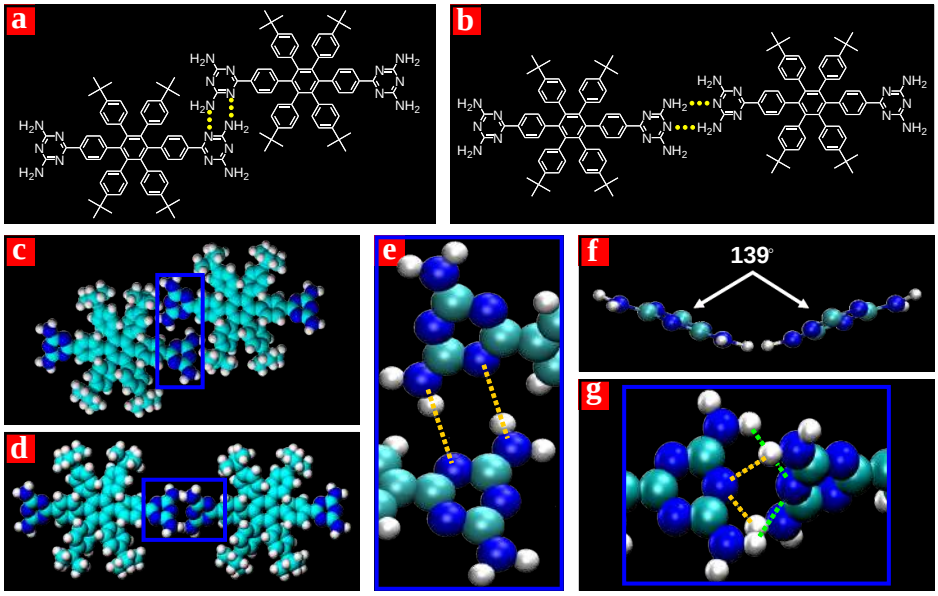

Figure 6.7: Two possible arrangements of Lander-DAT. (a) "*sideways*" coupling and (b) "*Head-to-tail*" coupling, showing hypothetical zig-zag stripes formed by hydrogen bonding between the adjacent diamino-triazine groups of the nearest neighbouring Lander-DAT along the stripes. Two theoretical arrangements of Lander-DAT after full relaxation by ASED approach. (c) "*sideways*" coupling, same as the anticipated model. (d) "*head-on*" coupling, showing a straight-row configuration rather than the zig-zag stripe of the "*Head-to-tail*" arrangement. (e) The close top-view of "*sideways*" coupling, where double N-H···N hydrogen bonds between the adjacent non-planar DAT groups of Lander-DAT are marked by yellow dashed lines. (f) The side-view of the "*sideways*" coupling, showing the rotation effect of the neighbouring DAT groups with a relative angle of 139°. (g) The close top-view of "*head-on*" coupling, where the rotation effect of the adjacent DAT groups are more notable and the two pairs of N-H···N hydrogen bonds are marked by dashed yellow and green lines respectively.

the Fig. 6.7g by yellow and green dashed lines for each pair of hydrogen bonds. The average N-H···N bond length and angle are 2.92 Å and 121°, respectively. The total intermolecular interaction for the "*sideways*" configuration is 0.682 eV: the strength of the hydrogen bonding is 0.486 eV (0.243 eV per hydrogen bond) and the contribution of vdW interaction is 0.196 eV. The interaction between the two neighbouring molecules in "*head-on*" coupling relaxed on the surface is 0.821 eV of which 0.092 eV comes from vdW energy and 0.729 eV from hydrogen bonding (0.182 eV per hydrogen bond).

In fact, the melamine molecule also adopts a non-planar configuration in bulk and gas phase [172]. Recent calculations using *ab initio* density functional theory (DFT) indicated that the non-planar configuration of melamine dimers is slightly more favorable with a higher stabilization energy (0.24 eV per hydrogen bond) than the planar one (0.22 eV per hydrogen bond), with a calculated N-H···N bond length of 2.89 Å [170]. This

is in good agreement with our calculations. In the case of Lander-DAT, the spacer legs lift-up the molecular board and the DAT functional end-groups, which are σ-bonded to the phenyl rings and further to the central board. Consequently, the high degree of conformational flexibility of Lander-DAT allows the DAT groups to tilt and rotate, hence offering the possibility to optimize the hydrogen bonding in three dimensions. This is distinct from 2D melamine networks and from the commonly studied compounds adsorbed flat on surfaces and assembled via intermolecular hydrogen-bonding interaction.

Table 6.1: Structural parameters of unit cells for different phases of Lander-DAT on Au(111). Vector lengths a, b in Å, angles between **a** and **b** in degrees, and density in molecule/nm^2.

Structure	Experimental results				Theory			coupling
	a	b	∠ab	density	a	b	∠ab	
chain on terraces	17.0	–	–	–	17.0	–	–	sideways
SM	36.4	36.4	60	0.523	36.5	36.5	61	sideways
FM	27.2	27.2	90	0.541	28	28	90	sideways
grid	20.8	28.5	60	0.390	20.1	31.6	58	head-on
Tran A	17.0	52.5	88	0.336	17.0	54.0	88	sideways
Tran B	17.0	33.7	106	0.364	17.2	33.0	106	sideways
stripe	16.5	17.0	60	0.424	17.7	17.7	55	sideways
Lander ND	12.5	15.4	85	0.521	13.2	15.9	89	–

6.5.2 1D-chain structure of Lander-DAT

At low coverage of Lander-DAT evaporated on a substrate kept at 300-400 K, long-range ordered 1D chains have been formed both at the step edges and on terraces. As seen from the large-scale STM image in Fig. 6.8a, the chains aligned along the step edges can extend over hundreds of nanometers. The close-up view of a single chain at sub-molecular resolution is presented in the inset of Fig. 6.8a. The periodicity along the chain is 17.0$\pm$0.5 Å, and the molecular axis is tilted by an angle of about 18° with respect to the orientation of the chain. These values are consistent with the theoretical results (16.9 Å and 19°) for the "*sideways*" configuration. Two of the four spacer legs of each single Lander-DAT look brighter/dimmer in this STM image, suggesting that the molecules in the chain are inclined on the step edge with two legs on upper/lower terraces, respectively.

The formation of similar 1D Lander-DAT chains on terraces (see Fig. 6.8b) does not disturb the herringbone reconstruction of the Au(111) substrate, implying a weak molecule-substrate interaction. The high-resolution STM image of an individual 1D chain adsorbed on terrace (inset of Fig. 6.8b) presents a "*sideways*" coupling identical to that observed at the step edges.

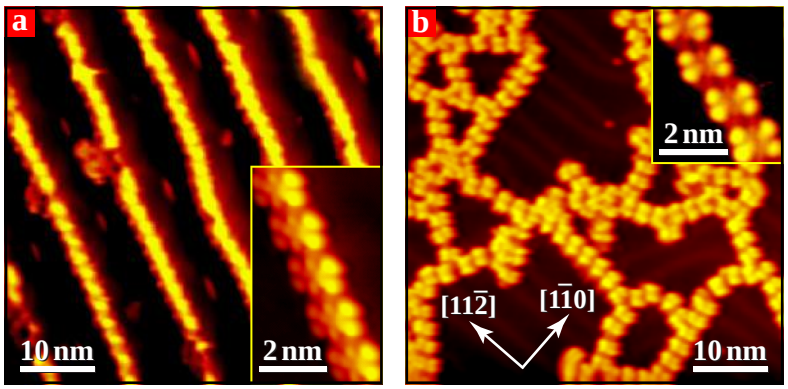

Figure 6.8: STM images of 1D chains of Lander-DAT on Au(111). (a) Large-scale view at the step edges ($I_t = 0.70$ nA, $V_t = 1250$ mV) and close-up view (inset, $I_t = 0.48$ nA, $V_t = 1487$ mV). (b) Large-scale view on terraces ($I_t = 0.52$ nA, $V_t = 1250$ mV) and close-up view (inset, $I_t = 0.46$ nA, $V_t = 1250$ mV).

6.5.3 H-bonded 2D structures of Lander-DAT

At higher coverage, five distinct 2D molecular architectures formed under different deposition conditions have been observed on the Au(111) surface. The structural parameters for each of these phases are summarized in Table 6.1.

The "six-blade mill" (SM) and the "four-blade mill" (FM) phases were obtained when the substrate was kept at relatively low temperature range (160-200 K) while depositing molecules. The coverage of the SM phase is lower than that of the FM phase. Both of them form large extended islands on the Au(111) surface, and can coexist in different domains. The FM phase appears as a defect-free network, which is more stable and ordered than the SM phase. The well-ordered large domains of the SM and FM phases together with their zoom-in STM images are presented in Fig. 6.9a,b and Fig. 6.10a,b respectively. A common feature for both phases is that these motifs are built from tiling of Lander-DAT dimers, as marked by the transparent rectangles joining the centers of two parallel molecules in Figs. 6.9b and 6.10b. In both cases, the molecules are adsorbed with their main axis along $\langle 11\bar{2} \rangle$ directions of the Au(111) substrate, i.e. the angle between molecules in different orientations is 60°.

There are three and two different molecular orientations for the SM and FM phases, respectively. The three different oriented Lander-DAT dimers of the SM phase are marked by white, green and blue rectangles, and the angle between these dimers is also 60°. Notice that the orientations of the dimers are not the same as for individual molecules. The unit cell parameters of the SM phase are $|\mathbf{a}| = |\mathbf{b}| = 36.4 \pm 1.0$ Å with $\angle \mathbf{ab} = 60°$, leading to a molecular density of 0.523 molecule per nm^2. The two different oriented Lander-DAT dimers of the FM phase are marked by the green and blue rectangles, which are orthogonal to each other. The unit cell parameters of the FM phase are $|\mathbf{a}| = |\mathbf{b}| = 27.2 \pm 1.0$ Å with $\angle \mathbf{ab} = 90°$, and the molecular density is 0.541 molecule per nm^2.

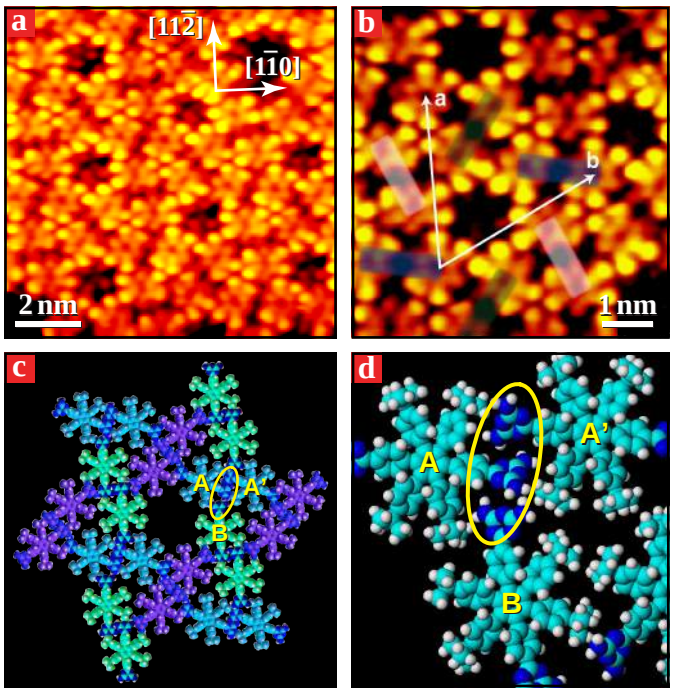

Figure 6.9: The "Six-blade Mill" (SM) phase of Lander-DAT on Au(111). (a) Large-scale STM image of a SM phase domain ($I_t = 0.23$ nA, $V_t = 1165$ mV), with orientations of Au(111) substrate. (b) High-resolution STM image of SM phase composed of three kinds of Lander-DAT dimers oriented at 60° between each other (rectangles in white, green and blue, $I_t = 0.24$ nA, $V_t = 1265$ mV). (c) The SM phase space-filling model of Lander-DAT where "*sideways*" coupled DAT dimers in different orientations are presented in pale blue, green and purple respectively. (d) Enlarged view of theoretical simulation for the 'SM' phase, showing the rotation of neighbouring DAT groups for 3-D optimized inner-dimer and inter-dimer hydrogen bonding interaction, where the A, A' correspond to the dimer in pale blue and B corresponds to the neighbouring molecule in green in panel (c).

The associated models for these two phases are illustrated in Figs. 6.9c and 6.10c, obtained by superimposing carefully-scaled space-filling Lander-DAT models onto the experimental STM image. The dimers with the same orientation are presented in the same color. Theoretical calculations have been performed on these two phases. Enlarged views of calculated configurations for the 'SM' and 'FM' phases are presented in Fig. 6.9d and 6.10d, respectively, centered on the section highlighted by the yellow ellipses in Figs. 6.9c and 6.10c, showing the rotation effect of DAT groups. In Fig. 6.9d, the A and A' correspond to the dimer in pale blue while B corresponds to the neighbouring molecule in green in Fig. 6.9c. In Fig. 6.10d, the A, A' and B, B' correspond to the dimers in pale blue and green in Fig. 6.10c, respectively. These close views of the proposed models display clearly the optimization of intermolecular hydrogen bonding optimized in three dimensions: each dimer is formed by double N-H$\cdots$N

hydrogen bonds in a "*sideways*" coupling as presented in Fig. 6.7c,e. The networks are further stabilized by additional inter-dimer double N-H···N hydrogen bonding between the free DAT groups of the neighbouring molecules which are not involved in the inner-dimer hydrogen bonding. The calculated structural parameters are consistent with the experimental values as shown in Table 6.1. The hydrogen-bond length and angle may present small variations with respect to the two model configurations in Fig. 6.7 in order to maximize the energy of the whole network.

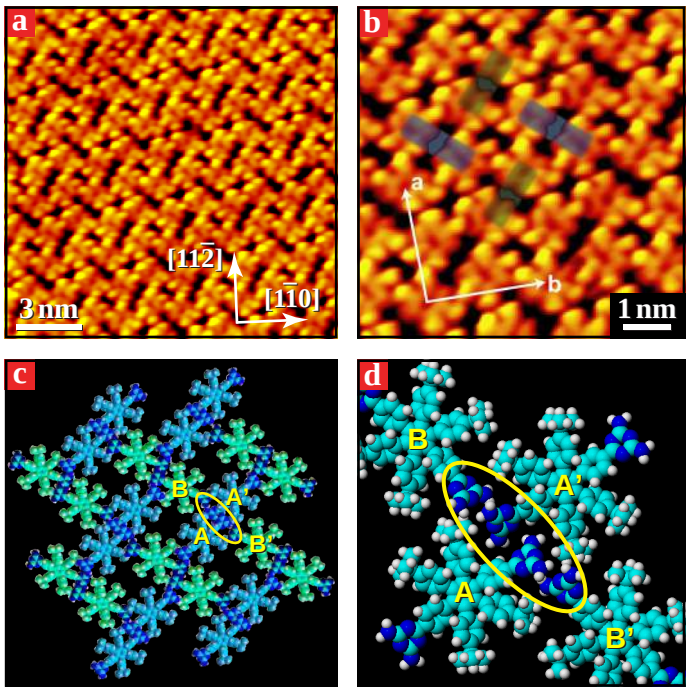

Figure 6.10: The "Four-blade Mill" (FM) phase of Lander-DAT on Au(111). (a) Large-scale STM image of a FM phase domain ($I_t = 0.50$ nA, $V_t = 1250$ mV) with orientations of Au(111) substrate. (b) A high-resolution STM image of FM phase ($I_t = 0.47$ nA, $V_t = 1250$ mV) composed of two kinds of Lander-DAT dimers oriented at 60° between each other (rectangles in green and blue). (c) The FM phase space-filling model of Lander-DAT where the "*sideways*" coupled DAT dimers in two orientations are presented in pale blue and green respectively. (d) Theoretical simulation for the "FM" phase, showing the rotation of neighbouring DAT groups for 3D optimized inner-dimer and inter-dimer hydrogen bonding interaction, where the A, A' correspond to the dimer in pale blue; B, B' correspond to the neighbouring dimer in green in panel (c).

By exposing the surface kept at a temperature range of 260-300 K to Lander-DAT molecules, the 'grid', 'transition' and 'stripe' phases have been gradually formed on the surface with increasing coverage. Careful inspection of the Au(111) surface revealed that the 'transition' and 'stripe' phases can occur simultaneously, while the 'grid' phase can coexist with 1D chains grown on terraces. These three phases have lower densities

than those of the 'SM' and 'FM' phases (see Table 6.1). Typical large scale and high-resolution STM images of the grid phase are depicted in Fig. 6.11a,b. As highlighted in Fig. 6.11a, the molecules in this phase either form a row-like motif (type A) as marked by the blue rectangles or connect these rows (type B) as marked by the green rectangles. Both of them are aligned with the main axis of DAT along $\langle 1\bar{1}0 \rangle$ type directions of the Au(111) substrate, hence the angle between A- and B-type molecules is also 60°. The unit cell parameters are $|\mathbf{a}|$=20.8±1.0 Å and $|\mathbf{b}|$=28.5±1.0 Å, with $\angle\mathbf{ab}$ = 60° and a density of 0.390 molecule/nm^2.

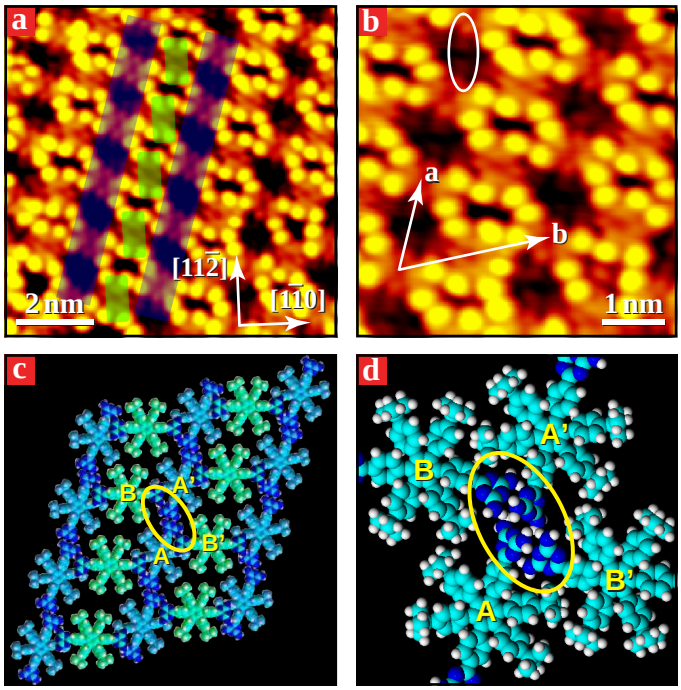

Figure 6.11: The 'Grid' phase of Lander-DAT on Au(111). (a) Large-scale STM image ($I_t = 0.44$ nA, $V_t = 1250$ mV), showing the individual connectors in green rectangles sitting between two row-like motifs of Lander-DAT (blue rectangles) with orientations of Au(111) substrate. (b) High-resolution STM image ($I_t = 0.42$ nA, $V_t = 1250$ mV), showing molecules aligned with their main axis along $\langle 1\bar{1}0 \rangle$ type directions of the Au(111) substrate. The features in the white circle are relevant to the tunneling through the DAT groups imaged at special tip conditions. (c) Space-filling model of Lander-DAT where row-like structures are in pale blue and the connectors are in green. (d) Enlarged view of the proposed model obtained by theoretical simulation showing the rotation effect of DAT groups. A, A' and B, B' correspond to two "*sideways*" coupled molecules in pale blue and two connectors in green.

Unlike the case of 1D chains, 'SM', and 'FM' phases, the periodicity of 20.8 Å and the nearly straight arrangement of the A-type motif is in a good agreement with the "*head-on*" configuration depicted in Fig. 6.7d,g. This arrangement is clearly distinct

from the signature of the "*sideways*" configuration, which has a periodicity of 17.0 Å and the molecular axis tilted by 19° away from the row direction. The structural parameters optimized with MM4 (see Table 6.1) are also consistent with the experimental values. In Fig. 6.11b, some features relevant to the DAT groups can be distinguished within the white ellipse. This image was registered at a special tip condition. It gives a direct evidence for the presence of DAT functional groups, and confirms that the Lander-DAT deposited on surfaces are intact. The associated model obtained using the same approach as for SM and FM phases is given in Fig. 6.11c, where the Lander-DAT in the row-like motifs are in pale blue and the connectors in green.

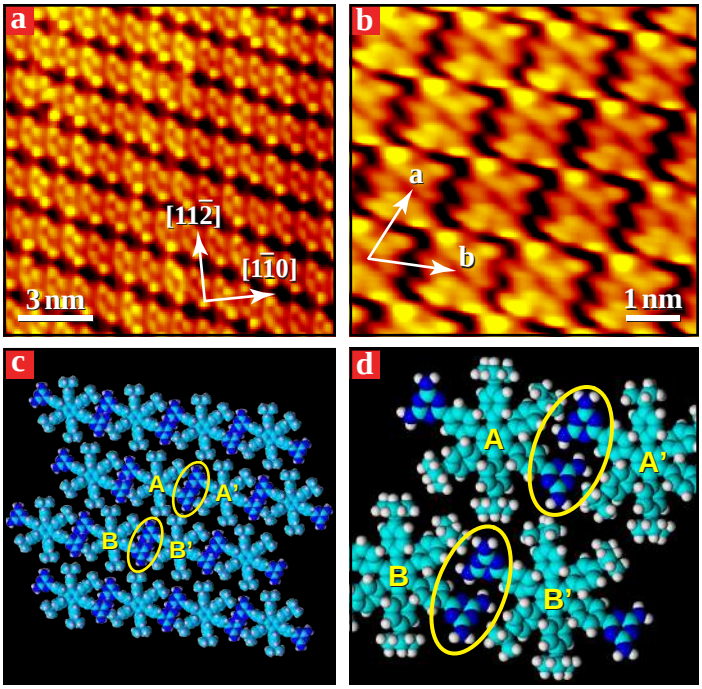

Figure 6.12: The 'Stripe' phase of Lander-DAT on Au(111). (a) Large-scale STM image (I_t = 0.48 nA, V_t = 1250 mV), showing close-packed parallel stripes of Lander-DAT with orientations of Au(111) substrate. (b) High-resolution STM image of the stripe phase (I_t = 0.48 nA, V_t = 1250 mV). (c) Space-filling model of Lander-DAT stripes. (d) Close-up view of panel c, where the yellow ellipses show the double N-H···N hydrogen bonding between the A, A' and B, B' molecules in "*sideways*" coupling.

A close view of the calculated model is presented in Fig. 6.11d, where the section highlighted by the yellow ellipse shows the configuration details of adjacent DAT groups. The A, A' and B, B' correspond to two 'sideways' coupled molecules and two connector-molecules illustrated in Fig. 6.11c in pale blue and green colors, respectively. It is seen that the row-like arrangement of A-type molecules are indeed stabilized by four N-H···N hydrogen bonding in 'head-on' coupling, while the B-type molecules in-

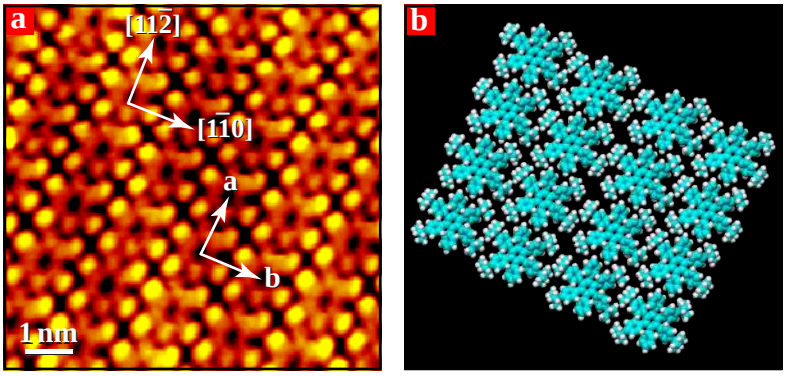

Figure 6.13: (a) A STM image of closed-packed Lander-ND on Au(111) ($I_t = 0.31$ nA, $V_t = 1250$ mV). (b) The simulated model of close-packed Lander-ND after full relaxation.

terconnect the rows by additional double hydrogen bonding as shown in Fig. 6.11d.

Fig. 6.12a displays the well-ordered extended island of the close-packed "stripe" phase, which is the most condensed of the structures obtained by dosing the molecules onto a substrate held at a relative high-temperature range (260-300 K). In most of the cases, the molecules in this phase are aligned along $\langle 1\bar{1}0 \rangle$ type directions of the Au(111) substrate, and there are three rotational domains on the surfaces. As shown in Fig. 6.12b, the unit cell parameters are |**a**|=16.5±0.5 Å, |**b**|=17.0±0.5 Å, with an angle ∠**ab** = 60° and a density of 0.424 molecule/nm^2.

The model based on STM images of the stripe phase is presented in Fig. 6.12c. In Fig. 6.12d the close-up view of the calculated configuration of the "stripe" phase reveals that each stripe along the b direction is formed by double N-H$\cdots$N hydrogen bonding between adjacent molecules in "sideways" coupling. In turn, these stripes are close-packed by vdW forces.

Two "transition" patterns (Tran A and Tran B) sharing some common structural features with "grid" and "stripe" phases were also found on Au(111) surface. They are mainly stabilized by double hydrogen bonding of DAT groups in "sideways" couplings.

6.5.4 Comparison with 2D structure of Lander-ND

In order to experimentally confirm that 3D hydrogen bonding between DAT end-groups is involved in the formation of the above described structures, the Lander-ND have been synthesized and studied with STM for comparison. In contrast to the various phases of Lander-DAT, we observed only a single adsorption structure for this compound, a close-packed 2D row structure shown in Fig. 6.13a.

Its unit cell parameters are |**a**| = 12.5±0.5 Å and |**b**| =15.4±0.5 Å, with ∠**ab** = 85° and a density of 0.521 molecule per nm^2. As seen in Table 6.1, the MM4 optimized structural parameters are consistent with experimental data. We suggest that within the Lander-ND rows, the molecules are stabilized by $\pi - \pi$ interaction between the phenyl rings of neighbouring molecules, and that the molecular rows are close-packed sideways by vdW interaction. Similar to Lander-DAT, the lifted-up peripheral phenyl groups also

possess enough flexibility to optimize the intermolecular $\pi - \pi$ interaction. This Lander-ND architecture has a great similarity with the stripe phase of Lander-DAT, but it is much more condensed (see Fig. 6.13b). It has a shorter periodicity along the row (12.5 Å vs 17.0 Å) and a smaller rotation angle of each molecule relative to the stripe axis (15° vs 19°). The difference in packing observed for Lander-DAT and Lander-ND molecules provide further evidence that the Lander-DAT are adsorbed intact on the surface, while the DAT end-groups may guide or influence the molecular self-assembly.

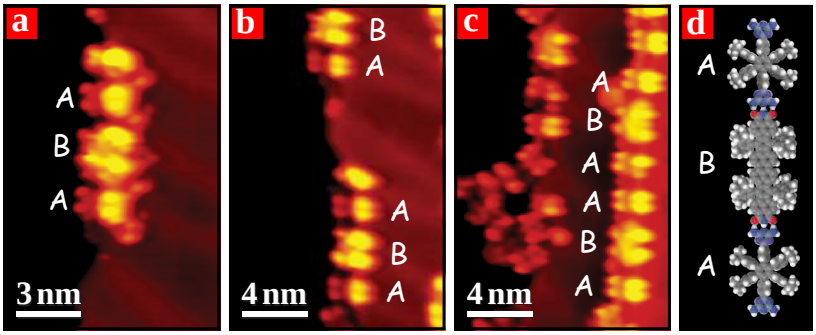

Figure 6.14: (a-c) STM images of short molecular chains formed from Lander-DAT (A) and Lander-DCI (B) at step edges of the Au(111) surface taken at the same $V_t = -1250$ mV, and $I_t = -0.45$, $I_t = -0.46$, $I_t = -0.33$ nA, respectively. (d) Tentative models of the chains formed by complementary triple hydrogen bonds.

6.6 Co-adsorption of Lander-DCI and DAT

In the present work, the co-deposition and self-assembly of two Lander-type molecules is achieved for the first time to fabricate hetero-molecular structures on the Au(111)surface. STM studies show that at low coverage, Landers DAT and DCI form alternated DAT-DCI-DAT short chains through triple hydrogen-bonds. The intriguing result of the present work is that at higher coverage these molecular building blocks self-assemble into a two-dimensional grid-like structure which consists of parallel Lander-DCI chains interconnected by Lander-DAT moieties.

6.6.1 Short molecular chains at step edges

STM images of the surface subsequent to codeposition of Lander-DAT and DCI molecules at low coverage are shown in Figs. 6.13a-c. This case is reflected by preferential anchoring of the molecules at step edges. Each moiety appears as two bright and two dim protrusions like in previous STM studies on related Lander molecules [152, 161]. A reasonable explanation for this observation is that the two bright spacer legs protrude on the upper terrace while the two dim spacer legs stand on the lower terrace. One can infer from comparison with high resolution images of single molecules (Figs. 6.2c and 6.3c) that the small and large four-lobed features have dimensions similar to those of Lander-DAT (A) and Lander-DCI (B) molecules, respectively. Therefore, the short chains in Figs. 6.14a-c are composed by alternating A-B-A molecules. The periodic-

ity in the A-B-A sequence is 51.5 Å. Assuming planar conformations of Lander-DAT and DCI molecules with dimensions of 22.6 Å and 28.9 Å, respectively, the NH···O and NH···N distance between DAT and DCI groups is of about 1.6 Å. This estimate corresponds well to the expected value of the triple hydrogen bond.

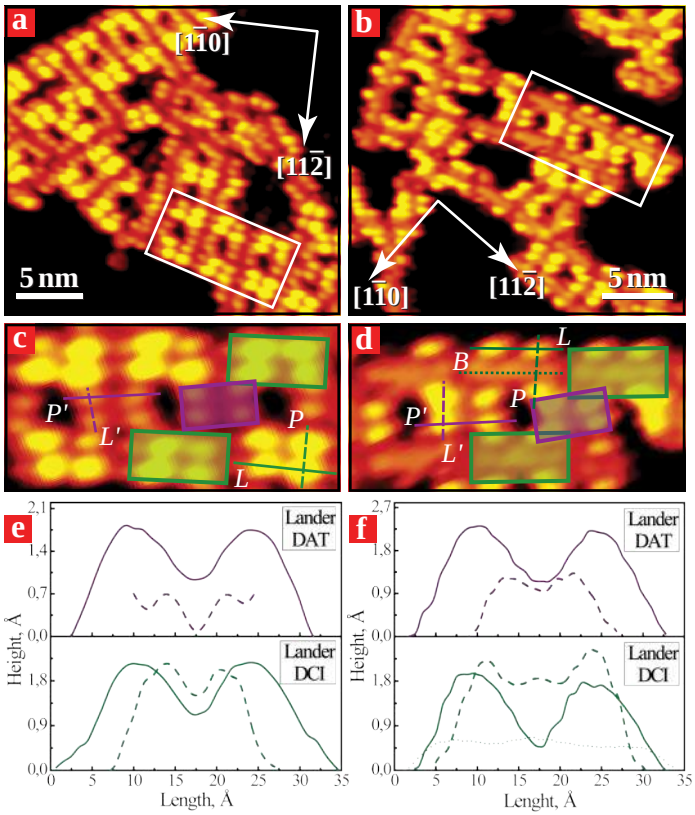

Figure 6.15: (a,b) Two STM imaging modes of the 2D grid-like molecular network formed after the co-deposition of Lander-DAT and DCI on the Au(111) surface, recorded at $V_t = -1250$ mV, and $I_t = -0.51$, $I_t = -0.39$ nA, respectively. (c,d) High resolution images of molecular islands in panels (a,b), where violet and green frames correspond to Lander-DAT and DCI, respectively. (e,f) The height profiles measured along indicated lines perpendicular and parallel to the axes of the molecules for both imaging modes.

Filled-space models of the DAT and DCI molecules superimposed with the experimental images of the short chains fit perfectly with *head-to-tail* interactions entailing complementary 2NH···O and 1NH···N triple hydrogen bonding illustrated in Figs. 6.14d,e. The binding energy of the triple hydrogen bond is expected to be similar to that calculated between CA and melamine molecules (0.48eV) [25]. It should be noticed that further annealing of the samples did not lead to the formation of longer A-B-A nanowires on the surface. Therefore, one may conclude that experimental conditions are

not directly responsible for the growth of short molecular chains.

This result provides the first experimental evidence that large Lander molecules can form 1D hetero-molecular structure through hydrogen bonding like in the predetermined filled-space model of Fig. 6.14d. This observation is extremely relevant regarding the possible usage of the known moulding properties of the Lander family to grow longer 1D metallic wires by trapping evaporated metal atoms under the molecules.

6.6.2 2D supramolecular network

With increasing adsorbate coverage, the Lander molecules co-deposited onto an atomically clean surface self-assemble into extended grid-like structure which was recorded in two different imaging modes (Figs. 6.15a,b). The high resolution STM images in Figs. 6.15c,d clearly attest that both Lander DAT (violet) and Lander DCI (green) molecules participate in the formation of this pattern.

Fig. 6.15e shows the line scans obtained for the first imaging mode along the directions (L, P) and (L', P') indicated in Fig. 6.15c. The distances between maxima of bright protrusions are consistent with characteristic distances of single Lander DCI and DAT molecules in Fig. 6.2c and Fig. 6.3c, respectively. Both molecules are imaged as four lobes. The high brightness lobes belong to Lander DCI molecules arranged into 1D chains interconnected by Lander DAT molecules imaged with lower contrast. In the second STM imaging mode, the DAT molecules appear as bright four-lobed features, while the DCI molecules are imaged as rods decorated by four protrusions (Fig. 6.15d). An additional line scan marked B in Fig. 6.15d,f gives a rod length of 26.5 Å in fair concordance with the backbone dimension of the Lander DCI model represented in Fig. 6.2c. Fig. 6.15d displays the STM registry of entire Lander molecules, where the molecular board is visualized together with the spacer legs groups.

Fig. 6.16a displays the STM image of a large molecular island with grid-like structure. The enhanced representation in Fig. 6.16b exemplifies a 2D molecular array formed by the regular arrangement of Lander DAT and DCI molecules. A tentative space-filled model of this structure is given in Fig. 6.16c. The framework of the grid-like structure consists of Lander DCI molecules forming wires via head-to-tail interaction. The periodicity along the chains is of 31.5 Å and is consistent with a hydrogen bond length of 3 Å close to that determined earlier for the isolated 1D rows of Lander DCI molecules adsorbed on Au(111) surface (Fig. 6.4).

A model of possible molecular bondings is presented in Fig. 6.16d. In this model the interaction between neighbouring Lander DCI molecules in the 2D network involves the same double NH$\cdots$O bonds as in the isolated 1D chains (shown by dashed lines). The O$-$O distances between Lander DCI chains are $d(12) = d(1'2') = 26$ Å. They accommodate well the size of embedded Lander A molecules in this framework. Furthermore, the O$-$O distances between Lander DCI in the chains are $d(11') = d(22') = 5.1$ Å which correspond well to the NH$\cdots$NH distance in the DAT group of the Lander-DAT molecule. As a consequence, each DAT Lander may interact with four DCI Landers via NH$\cdots$O hydrogen bonding (2NH$\cdots$O of 1.4 Å and 2NH$\cdots$O of 2.7 Å). The optimization of the DAT-DCI interactions causes the symmetry axis of Lander DAT molecules to be tilted by 78° from the backbone axis of Lander DCI molecules. Additionally, the chains of Lander DCI are shifted by 4.8 Å with respect to each other along the long axis of the

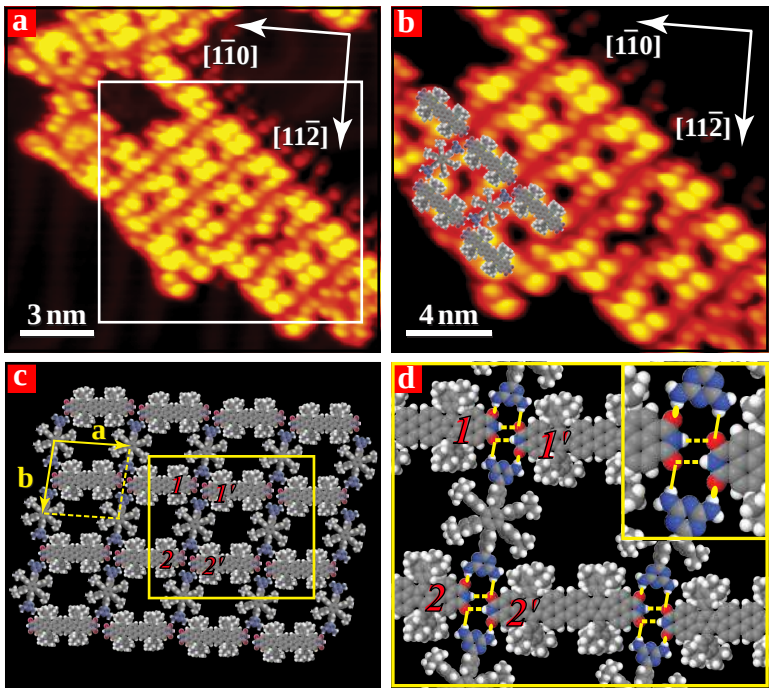

Figure 6.16: (a) Two-dimensional island formed from Lander-DAT and Lander-DCI on the Au(111) surface ($V_t = -1250$ mV, and $I_t = -0.49$ nA). (b) High resolution image of the same island with superimposed molecular models. (c) Model of the 2D molecular structure composed of Lander-DCI chains interconnected by Lander-DAT molecules. (d) Zoom-in on the model showing the hydrogen bonding interactions involved in the formation of the 2D network structure.

molecular backbone.

Surprisingly, the anticipated 1D hetero-molecular chains stabilized by complementary triple H-bonding between alternating Lander DAT and DCI molecules were not found on the Au(111) terraces. This observation might be ascribed to the difference in binding energy of Lander DCI-DCI and Lander DCI-DAT dimers. The next attempt to facilitate the growth of extended 1D hetero-molecular chains formed by alternating Lander DAT and DCI molecules via triple H-bonding, could be realized by self-assembly of these molecular species on anisotropic metal substrates such as Au(110).

6.7 Conclusion

In summary, by utilizing diamino-triazine and di-carboxylic imide functional groups to guide the self-assembly of molecular Landers, we have achieved 1D and several distinct 2D supramolecular nanostructures on a Au(111) surface. It is the first time that long-range well-ordered 1D and complex 2D organic architectures lifted above and decoupled from the substrate are successfully built up. Evaporation of these heavy molecules required careful trials to delineate the proper temperature ranges for the most efficient

sublimations without fragmentation of the compounds.

For the Lander-DCI the present results demonstrate that the N-H$\cdots$O double hydrogen bonding can not only induce stable 2D structures for molecules with their boards adsorbed directly on surfaces but also stabilize isolated 1D chains formed from larger molecules with spacer legs. While the hydrogen bonding between DCI groups dominates the formation of the 1D chains, the molecule-substrate interaction primarily guides the alignment of the resultant chains along preferred substrate directions.

In the case of the Lander-DAT, long-range well-ordered 1D chains can be formed at step edges and short chains on the terraces under specific deposition conditions. The conformational flexibility of this molecule induces a variety of different 2D molecular architectures that are stabilized by hydrogen bonding optimized in three dimensions.

Finally, we have investigated the formation of hetero-molecular structures by codepositing Lander DAT and DCI molecules. At low coverage, short 1D structures are growing at steps with typical ABAABA sequential order. This constitutes the first evidence that complementary head-to-tail intermolecular interactions resulting from triple hydrogen bonds can lock together different species of bulky Lander molecules at surfaces. At higher coverages, Lander DAT and DCI molecules self-organize on the substrate into an extended 2D grid-like structure. This pattern is composed of hydrogen-bonded Lander-DCI chains interconnected through hydrogen bonding provided by Lander-DAT molecules. No mixed A-B-A linear structure was found on the terraces of Au(111). Under the codeposition conditions described above, Lander-DAT molecules cement together parallel chains made of Lander-DCI molecules into a well contrived 2D network. These intriguing results indicate that double NH$\cdots$O bonding between Lander-DCI molecules is favoured to the detriment of the strongly directional interaction which ought to be provided by triple NH$\cdots$O and NH$\cdots$N bonds between Lander-DAT and Lander-DCI species. More investigations on different substrate surfaces are ongoing in an effort to solve this question.

The present work demonstrates the possibility to generate and stabilize complex homo- and hetero-molecular nanoarchitectures made of large Lander molecules without modifying their chemical integrity. With the proven function of molecular Landers as molecular moulds, a next step will be to investigate if the synthesized 1D chains or 2D structures are able to act as extended moulds for bottom-up assembly of metal adatoms on surfaces, e.g. into conducting atomic-scale wires and networks with potential relevance for applications in areas of nanoelectronics and other nanodevices. Moreover, since the self-assembly of these functionalized Lander molecules is guided primarily by intermolecular hydrogen bonding interactions, it may be possible to transfer the 1D and 2D synthesis to other more practically relevant substrates such as insulators or thin insulating films.

CHAPTER 7

Summary and outlook

Self-assembly of molecules and biomolecules at surfaces is of utmost interest in many technological areas such as molecular switches, nanomachines, sensors, nanoelectronics, integrated optics, biochemistry, and pharmaceuticals. Therefore, this bottom-up strategy undergoes an exponentional growth as a complement and alternative to top-down approaches.

Self-assembly techniques are based on the paradigm that atomic and building blocks can self-organize spontaneously via autonomous mechanisms involving intramolecular attributes, intermolecular interactions, and subtle interplay between the adsorbate and the substrate. The inner forces driving molecular self-assembly at surfaces are yet to be fully understood. In a majority of cases they are non-covalent in nature. Among non-covalent interactions that can be exploited to direct the assembly of molecules into nanometre-sized functional structures, hydrogen bonding competes efficiently with dipolar coupling, van der Waals forces, $\pi - \pi$, and hydrophobic interactions.

Studying such molecular interactions requires that the adsorbates will be deposited - by thermal evaporation in this thesis - on ultra clean, well characterized surfaces, and thus imposes to work under well-controlled ultra-high vacuum conditions with appropriate tools able to probe the systems at the nanometer scale. No better choice can be made than to benefit from the powerful capability of the scanning tunnelling microscope which offers unparalleled amenities to decipher complex self-organized patterns with submolecular resolution. The present work reports on several novel advances in the self-assembly of complex molecular systems studied by UHV STM.

The challenge of this thesis was to find the appropriate conditions to self-assemble five different molecular systems on metallic and insulating substrates under UHV and to register successfully STM images of each self-assembly in order to obtain reliable

data for subsequent analysis. The Ariadne's thread of this study leads to one of the most fascinating chemical interactions virtually responsible for the various patterns observed: the hydrogen bond. The H-bond is present in the β-strands forming β-sheets in the aggregation of peptides and is expected to play a significant role in their self-assembly. Among the investigated molecular systems, melamine, cyanuric acid, and Lander molecules seem quite different by their chemical nature. They were, however, chosen because they share the same functional groups. Self-organization of these compounds appears to be directed by intermolecular hydrogen bonding between these groups. The coadsorption of CA and M molecules on an insulating layer is totally driven by the H-bond. Similarly, in the adsorption of large Lander molecules on Au(111), the H-bond reveals itself the essential intermolecular ingredient able to stabilize these molecules into a wealth of complex 1D and 2D supramolecular architectures.

It is well-known that chirality plays a crucial role not only in biochemistry but also for technological applications. For instance, biological molecules adopt only left-handed configurations. One family of molecules investigated during the thesis are the oligo-phenylene ethynylenes which have the chemical backbone of many of the molecules used in molecular electronics. Before the beginning of the present work two members of the iNANO group, S. Weigelt and T. Linderoth, made a breakthrough experiment by showing that *tert*-butyl oligo-phenylene-ethynylene molecules can switch between two different surface chiral forms even after adsorption on Au. This work has paved the way to come up with a fundamental question: is it possible that only one chiral form of these molecules could cover the entire surface? The third chapter of this thesis has addressed this issue in the sense that homochirality of *sec*- and *tert*-butyl oligo-phenylene-ethynylene compounds adsorbed on Au was evidenced. Moreover, it was demonstrated that achiral *sec*-butyl molecules can be used to seed the surface in order to force *tert*-butyl molecules into the same chiral configuration. This phenomenon is referred to as chiral amplification or chiral induction. The mechanism responsible for chiral induction is analogous to the "sergeants-and-soldiers" effect reported earlier for the adsorption of the achiral-chiral SU-TA system on surfaces. A significant proportion of "sergeants" (*sec*-butyl molecules) was able to induce homochirality in the "soldiers" (*tert*-butyl molecules) self-assembly. Two experimental protocols led to this observation. In the first case, chiral amplification is promoted by the formation of seamless boundaries between *sec*-butyl nucleation islands and *tert*-butyl domains. Here, the *sec*-butyl chiral conformation propagates to *tert*-butyl domains. In the second case, a different codeposition process induces strong intermixing between *sec*-butyl and *tert*-butyl molecules. This results in extended domains where *tert*-butyl molecules adopt the chirality of the *sec*-butyl ones.

There is no doubt among the community working in the field of protein aggregation that the understanding of assembly mechanisms in amyloid fibrils requires to determine the fibril structures at the atomic scale. It is our belief that STM can provide valuable information about the subtle architecture of model systems like tetrapeptides which are known to form fibrils. The huge difficulty to obtain high resolution details of the fibril structure can be at least removed and at best solved by means of STM investigations carried out on these simple systems. Most experiments so far have not probed the structural

organization of short peptides in fibrils beyond single β-sheets. The focus of Chapter 4 was to find organizational and conformational clues from the atomic visualization of self-assembled structures at surface which could be transferred to more complex biochemical architectures. The work presented in this thesis goes on a much deeper level than in previous studies, and is mainly based on a descriptive and tentative analysis of tetrapeptide interactions at the nanoscale, sustained by solid experimental evidence and by a well-known efficient computational method used for protein structure determination.

In the frame of this ambitious project, it was shown that it is possible to depose tetrapeptide biomolecules (KFFE and KVVE) at metallic surface under UHV by thermal evaporation while preserving their structural integrity and that they can form an incredible variety of self-assembled structures. Although self-assembly of dipeptides was achieved previously by other groups on Cu surfaces, there is at the present knowledge no published work concerning the deposition of longer peptides under UHV. Depending on the tip state, the STM images of tetrapeptide self-assemblies obtained at submolecular resolution allow to identify the peptide side chains: glutamate, phenylalanine, lysine, and valine. This identification mainly relies on the examination of point defects and island perimeters in the observed patterns and on restrained MDFF structures obtained by Jakob Nielsen (Department of Chemistry at the University of Aarhus) with the XPLOR-NIH software package for computational structural biology. Having identified the residues or side chains, it was possible to show that the tetrapetides can form different surface conformers that can be clearly distinguished in the STM images. KFFE and KVVE adsorb on surface in row-like structures consisting of several sub-patterns such as ziz-zag, and cross-linked arrangements. The determination of the intermolecular distances and the analysis of conformer orientations enable to propose that upon adsorption on the surface in UHV environment, adjacent peptides can aggregate into either "parallel" or "antiparallel" molecular configuration. In one instance, it was observed that KVVE organizes into an antiparallel row structure in which molecules are arranged in rotor-like shapes with clockwise and anticlockwise chiral patterns. There is a line of evidence that the latter configuration could be related to the fibrillization process involving the so-called *antiparallel* β-strands. Under slightly different deposition conditions KFFE forms also a porous windmill structure with a chiral pattern also disclosing some *antiparallel* characteristics.

The perspectives associated to the tetrapeptide aggregation study are multiple. The change in environmental conditions and deposition (like spray deposition, or liquid phases) could bring this research towards new horizons in defining for example what are the external conditions which may affect (or favour) the aggregation of peptides on surfaces. Remaining questions touch on the influence of the surface itself on these mechanisms (chiral metallic surfaces, semi-conducting or dielectric surfaces) as well as to the patterns which could be observed by studying related peptides with other residue sequences.

Another project has explored the dynamics and self-assembly of organic molecules on non-metallic substrates such as thin dielectric films. We started by developing the competence to grow ultrathin dielectric substrates consisting of a few atom layers, by

UHV thermal evaporation of NaCl onto metallic surfaces cleaned by sputtering and annealing cycles. The previous studies of melamine/cyanuric acid initiated in the STM group have been therefore extended to this thin film in order to investigate the effects of a reduced molecule-substrate interaction. We demonstrated that it is possible to stabilize 2D islands of the bimolecular system M-CA on this ultrathin NaCl layer, which have the typical rosette structure previously found on Au(111) at coverage below one monolayer.

Since M and CA can form self-assembled networks through triple H-bonding provided by diamino-triazine and di-carboxylic imide functional groups, we have shifted to the self-assembly of more advanced compounds, referred to as Landers, bearing the same end groups. These Lander molecules (DCI, DAT) are synthesized in the laboratory of Andre Gourdon in Toulouse. A Lander molecule consists of a π-system conducting board and several spacer legs that elevate the board from the substrate, with the aim of electronically isolating it from the surface. We have first achieved the monomolecular self-assembly of 1D chains and 2D extended domains of Landers DAT (A) and DCI (B) on Au(111). It was shown that, in specific deposition conditions, these molecules self-organize on the surface by head-to-tail, head-on, and sideways H-bonding interactions. The final aim of this investigation was to inquire into the possibility to grow bimolecular Lander chains (ABABAB...) interacting via complementary triple H-bonds. Several bimolecular self-assemblies were indeed evidenced upon sublimation of the two compounds on the surface. At low coverage, short segments with sequential order ABAABA adsorb at step-edges. This is the first demonstration that complementary head-to-tail interactions can occur between two different, codeposited Landers. At higher coverage, long wires of Lander-DCI grow via head-to-tail interaction. These chains are held together in 2D grid-like structures by Lander-DAT connectors.

On that account, the present work has proved that it is possible to grow 1D molecular wires and 2D "grids" of Lander compounds on Au(111) by complementary ABAB or BBB/AAA/BBB bonding interactions. We are therefore on firm grounds to advance further on toward the next perspective which would be to use molecular self-assembly in combination with metal deposition on *insulating surfaces* and *dielectric* films (see Fig. 7.1). Still a formidable task to manage, we believe that synthesis of nanowires and molecule-electrode nano-contacts relevant for the field of "molecular electronics" should be feasible by using the known moulding property of the Lander family to trap evaporated metal atoms beneath their molecular board.

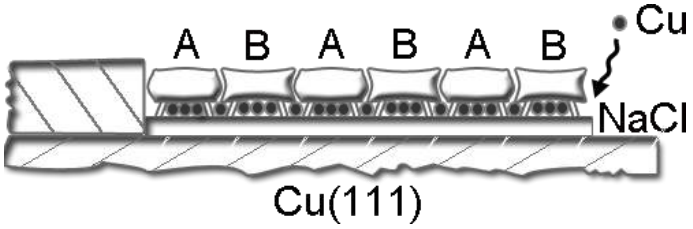

Figure 7.1: Self-assembly of linear molecular nanostructures from complementary A and B molecules adsorbed at ultrathin NaCl layers deposited on Cu(111) surface, and use of these molecular structures as moulds to trap Cu adatoms.

As another perspective, it could be also interesting to extend these studies to the growth of highly regular nanostructures of hexagonal boron nitride (h-BN) which has the advantage to be a much more stable insulating layer to external environment factors than NaCl. Electronic decoupling of molecules and nanoparticles from the metal substrate by a thin insulating h-BN layer can be relevant in nanoelectronics. h-BN monolayer can be grown on Ni(111) and Pd(110) surfaces and h-BN nanomesh structure can be formed on Rh(111) and Ru(001) substrates. Both h-BN structures are very promising for adsorption of functional molecules or deposition of metallic nanoclusters. The possibility of molecular self-assembly on the h-BN monolayer and trapping of molecules in the h-BN nanomesh could be investigated. Boron nitride layers can be obtained by exposing the atomically clean transition metal surface to a borazine $(HBNH)_3$ vapour pressure inside an UHV chamber.

Bibliography

[1] R. P. Feynman, "There's plenty of room at the bottom", *J. Microelectromech. Syst.* **1**, 60 (1992).

[2] J. V. Barth, G. Costantini, and K. Kern, "Engineering atomic and molecular nanostructures at surfaces", *Nature* **437**, 671 (2005).

[3] F. Rosei, M. Schunack, Y. Naitoh, P. Jiang, A. Gourdon, E. Laegsgaard, I. Stensgaard, C. Joachim, and F. Besenbacher, "Properties of large organic molecules on metal surfaces", *Prog. Surf. Sci.* **71**, 95 (2003).

[4] T. Ito and S. Okazaki, "Pushing the limits of lithography", *Nature* **406**, 1027 (2000).

[5] J. V. Barth, "Molecular architectonic on metal surfaces", *Annu. Rev. Phys. Chem.* **58**, 375 (2007).

[6] J. Weckesser, J. V. Barth, and K. Kern, "Direct observation of surface diffusion of large organic molecules at metal surfaces: PVBA on Pd(110)", *J. Chem. Phys.* **110**, 5351 (1999).

[7] J. Weckesser, J. V. Barth, and K. Kern, "Mobility and bonding transition of C60 on Pd(110)", *Phys. Rev. B* **64**, 161403 (2001).

[8] J. K. Gimzewski, C. Joachim, R. R. Schlittler, V. Langlais, H. Tang, and I. Johannsen, "Rotation of a single molecule within a supramolecular bearing", *Science* **281**, 531 (1998).

[9] G. M. Whitesides, J. P. Mathias, and C. T. Seto, "Molecular self-assembly and nanochemistry - a chemical strategy for the synthesis of nanostructures", *Science* **254**, 1312 (1991).

[10] J. V. Barth, J. Weckesser, N. Lin, A. Dmitriev, and K. Kern, "Supramolecular architectures and nanostructures at metal surfaces", *Appl. Phys. A: Mater. Sci. Process.* **76**, 645 (2003).

[11] R. Otero, M. Schock, L. M. Molina, E. Laegsgaard, I. Stensgaard, B. Hammer, and F. Besenbacher, "Guanine quartet networks stabilized by cooperative hydrogen bonds", *Angew. Chem. Int. Ed.* **44**, 2270 (2005).

[12] A. G. Trant, T. E. Jones, and C. J. Baddeley, "Thermal treatment of glutamic acid-modified nickel nanoclusters on Au111 leads to the formation of one-dimensional metal-organic coordination networks", *J. Phys. Chem. C* **111**, 10534 (2007).

[13] T. Yokoyama, S. Yokoyama, T. Kamikado, Y. Okuno, and S. Mashiko, "Selective assembly on a surface of supramolecular aggregates with controlled size and shape", *Nature* **413**, 619 (2001).

[14] T. Steiner, "The hydrogen bond in the solid state", *Angew. Chem. Int. Ed.* **41**, 48 (2002).

[15] S. M. Barlow and R. Raval, "Complex organic molecules at metal surfaces: bonding, organisation and chirality", *Surf. Sci. Rep.* **50**, 201 (2003).

[16] A. Gerlach, F. Schreiber, S. Sellner, H. Dosch, I. A. Vartanyants, B. C. C. Cowie, T. L. Lee, and J. Zegenhagen, "Adsorption-induced distortion of F16CuPc on Cu(111) and Ag(111): An x-ray standing wave study", *Phys. Rev. B* **71**, 205425 (2005).

[17] T. A. Jung, R. R. Schlittler, and J. K. Gimzewski, "Conformational identification of individual adsorbed molecules with the STM", *Nature* **386**, 696 (1997).

[18] S. Weigelt, C. Busse, L. Petersen, E. Rauls, B. Hammer, K. V. Gothelf, F. Besenbacher, and T. R. Linderoth, "Chiral switching by spontaneous conformational change in adsorbed organicmolecules", *Nat. Mater.* **5**, 112 (2006).

[19] K. H. Ernst, "Supramolecular surface chirality", T*op. Curr. Chem.* **265**, 209 (2006).

[20] M. Bohringer, W. D. Schneider, and R. Berndt, "Real space observation of a chiral phase transition in a two-dimensional organic layer", A*ngew. Chem. Int. Ed.* **39**, 792 (2000).

[21] A. Kühnle, T. R. Linderoth, B. Hammer, and F. Besenbacher, "Chiral recognition in dimerization of adsorbed cysteine observed by scanning tunnelling microscopy", *Nature* **415**, 891 (2002).

[22] M. de Wild, S. Berner, H. Suzuki, H. Yanagi, D. Schlettwein, S. Ivan, A. Baratoff, H. J. Guentherodt, and T. A. Jung, "A novel route to molecular self-assembly: Self-intermixed monolayer phases", *ChemPhysChem* **3**, 881 (2002).

[23] S. Weigelt, C. Busse, C. Bombis, M. M. Knudsen, K. V. Gothelf, T. Strunskus, C. Woll, M. Dahlbom, B. Hammer, E. Laegsgaard, F. Besenbacher, and T. R. Linderoth, "Covalent interlinking of an aldehyde and an amine on a Au(111) surface in ultrahigh vacuum", *Angew. Chem. Int. Ed.* **46**, 9227 (2007).

[24] L. Stryer, *Biochemistry*, 4th ed. (W. H. Freeman, New York, 1995).

[25] W. Xu, M. D. Dong, H. Gersen, E. Rauls, S. Vazquez-Campos, M. Crego-Calama, D. N. Reinhoudt, I. Stensgaard, E. Laegsgaard, T. R. Linderoth, and F. Besenbacher, "Cyanuric acid and melamine on Au(111): Structure and energetics of hydrogen-bonded networks", *Small* **3**, 854 (2007).

[26] P. A. Staniec, L. M. A. Perdigao, B. L. Rogers, N. R. Champness, and P. H. Beton, "Honeycomb networks and chiral superstructures formed by cyanuric acid and melamine on Au(111)", J. *Phys. Chem. C* **111**, 886 (2007).

[27] J. A. Theobald, N. S. Oxtoby, M. A. Phillips, N. R. Champness, and P. H. Beton, "Controlling molecular deposition and layer structure with supramolecular surface assemblies", *Nature* **424**, 1029 (2003).

[28] M. Ruiz-Oses, N. Gonzalez-Lakunza, I. Silanes, A. Gourdon, A. Arnau, and J. E. Ortega, "Self-assembly of heterogeneous supramolecular structures with uniaxial anisotropy", *J. Phys. Chem. B* **110**, 25573 (2006).

[29] R. A. Sheldon, *Chirotechnology: Industrial Synthesis of Optically Active Compounds*, 1st ed. (Marcel Dekker, New York, 1993).

[30] L. Pasteur, "Sur les relations qui peuvent exister entre la forme cristalline, la composition chimique, et le sens de la polarisation rotatoire", *Ann. Chim. Phys.* **24**, 442 (1848).

[31] J. M. Bonello, F. J. Williams, and R. M. Lambert, "Aspects of enantioselective heterogeneous catalysis: structure and reactivity of (S)-(-)-1-(1-naphthyl)ethylamine on Pt111", *J. Am. Chem. Soc.* **125**, 2723 (2003).

[32] M. O. Lorenzo, S. Haq, T. Bertrams, P. Murray, R. Raval, and C. J. Baddeley, "Creating chiral surfaces for enantioselective heterogeneous catalysis: R,R-Tartaric acid on Cu(110)", *J. Phys. Chem. B* **103**, 10661 (1999).

[33] T. Verbiest, S. Van Elshocht, M. Kauranen, L. Hellemans, J. Snauwaert, C. Nuckolls, T. J. Katz, and A. Persoons, "Strong enhancement of nonlinear optical properties through supramolecular chirality", *Science* **282**, 913 (1998).

[34] K. Ray, S. P. Ananthavel, D. H. Waldeck, and R. Naaman, "Asymmetric scattering of polarized electrons by organized organic films of chiral molecules", *Science* **283**, 814 (1999).

[35] M. O. Lorenzo, C. J. Baddeley, C. Muryn, and R. Raval, "Extended surface chirality from supramolecular assemblies of adsorbed chiral molecules", *Nature* **404**, 376 (2000).

[36] S. M. Barlow, S. Louafi, D. Le Roux, J. Williams, C. Muryn, S. Haq, and R. Raval, "Supramolecular assembly of strongly chemisorbed size-and shape-defined chiral clusters: S- and R-alanine on Cu(110)", *Langmuir* **20**, 7171 (2004).

[37] H. P. Steinrück, W. Huber, T. Pache, and D. Menzel, "The Adsorption of Benzene Monolayers and Multilayers on Ni(111) Studied by TPD and LEED", *Surf. Sci.* **218**, 293 (1989).

[38] J. V. Barth, J. Weckesser, C. Z. Cai, P. Gunter, L. Burgi, O. Jeandupeux, and K. Kern, "Building supramolecular nanostructures at surfaces by hydrogen bonding", *Angew. Chem. Int. Ed.* **39**, 1230 (2000).

[39] C. B. France and B. A. Parkinson, "Naphtho[2,3-a]pyrene forms chiral domains on Au(111)", *J. Am. Chem. Soc.* **125**, 12712 (2003).

[40] F. Vidal, E. Delvigne, S. Stepanow, N. Lin, J. V. Barth, and K. Kern, "Chiral phase transition in two-dimensional supramolecular assemblies of prochiral molecules", *J. Am. Chem. Soc.* **127**, 10101 (2005).

[41] C. M. Dobson, "Protein folding and misfolding", *Nature* **426**, 884 (2003).

[42] X. J. Ma, L. Liu, X. B. Mao, L. Niu, K. Deng, W. H. Wu, Y. M. Li, Y. L. Yang, and C. Wang, "Amyloid beta (1-42) Folding Multiplicity and Single-Molecule Binding Behavior Studied with STM", *J. Mol. Biol.* **388**, 894 (2009).

[43] X. B. Mao, X. J. Ma, L. Liu, L. Niu, Y. L. Yang, and C. Wang, "Structural characteristics of the beta-sheet-like human and rat islet amyloid polypeptides as determined by scanning tunneling microscopy", *J. Struct. Biol.* **167**, 209 (2009).

[44] X. B. Mao, Y. B. Wang, L. Liu, L. Niu, Y. L. Yang, and C. Wang, "Molecular-Level Evidence of the Surface-Induced Transformation of Peptide Structures Revealed by Scanning Tunneling Microscopy", *Langmuir* **25**, 8849 (2009).

[45] R. E. A. Kelly, W. Xu, M. Lukas, R. Otero, M. Mura, Y. J. Lee, E. Laegsgaard, I. Stensgaard, L. N. Kantorovich, and F. Besenbacher, "An investigation into the interactions between self-assembled adenine molecules and a Au(111) surface", *Small* **4**, 1494 (2008).

[46] M. Lukas, R. E. A. Kelly, L. N. Kantorovich, R. Otero, W. Xu, E. Laegsgaard, I. Stensgaard, and F. Besenbacher, "Adenine monolayers on the Au(111) surface: Structure identification by scanning tunneling microscopy experiment and ab initio calculations", *J. Chem. Phys.* **130** (2009).

[47] R. Otero, M. Lukas, R. E. A. Kelly, W. Xu, E. Laegsgaard, I. Stensgaard, L. N. Kantorovich, and F. Besenbacher, "Elementary structural motifs in a random network of cytosine adsorbed on a gold(111) surface", *Science* **319**, 312 (2008).

[48] R. Otero, W. Xu, M. Lukas, R. E. A. Kelly, E. Laegsgaard, I. Stensgaard, J. Kjems, L. N. Kantorovich, and F. Besenbacher, "Specificity of Watson-Crick Base Pairing on a Solid Surface Studied at the Atomic Scale", *Angew. Chem. Int. Ed.* **47**, 9673 (2008).

[49] L. M. A. Perdigão, P. A. Staniec, N. R. Champness, R. E. A. Kelly, L. N. Kantorovich, and P. H. Beton, "Experimental and theoretical identification of adenine monolayers on Ag-terminated Si(111)", *Phys. Rev. B* **73** (2006).

[50] W. Xu, R. E. A. Kelly, H. Gersen, E. Laegsgaard, I. Stensgaard, L. N. Kantorovich, and F. Besenbacher, "Prochiral Guanine Adsorption on Au(111): An Entropy-Stabilized Intermixed Guanine-Quartet Chiral Structure", *Small* **5**, 1952 (2009).

[51] W. Xu, R. E. A. Kelly, R. Otero, M. Schock, E. Laegsgaard, I. Stensgaard, L. N. Kantorovich, and F. Besenbacher, "Probing the hierarchy of thymine-thymine interactions in self-assembled structures by manipulation with scanning tunneling microscopy", *Small* **3**, 2011 (2007).

[52] Q. Chen and N. V. Richardson, "Enantiomeric interactions between nucleic acid bases and amino acids on solid surfaces", *Nat. Mater.* **2**, 324 (2003).

[53] M. Lingenfelder, G. Tomba, G. Costantini, L. C. Ciacchi, A. De Vita, and K. Kern, "Tracking the chiral recognition of adsorbed dipeptides at the single-molecule level", *Angew. Chem. Int. Ed.* **46**, 4492 (2007).

[54] G. Tomba, M. Lingenfelder, G. Costantini, K. Kern, F. Klappenberger, J. V. Barth, L. C. Ciacchi, and A. De Vita, "Structure and energetics of diphenylalanine self-assembling on Cu(110)", *J. Phys. Chem. A* **111**, 12740 (2007).

[55] I. Stensgaard, "Adsorption of di-L-alanine on Cu(110) investigated with scanning tunneling microscopy", *Surf. Sci.* **545**, L747 (2003).

[56] G. Binning, H. Rohrer, C. Gerber, and E. Weibel, "Surface Studies by Scanning Tunneling Microscopy", *Phys. Rev. Lett.* **49**, 57 (1982).

[57] J. V. Lauritsen, R. T. Vang, and F. Besenbacher, "From atom-resolved scanning tunneling microscopy (STM) studies to the design of new catalysts", *Catal. Today* **111**, 34 (2006).

[58] F. Besenbacher, "Scanning tunnelling microscopy studies of metal surfaces", *Rep. Prog. Phys.* **59**, 1737 (1996).

[59] R. Wolkow and P. Avouris, "Atom-Resolved Surface-Chemistry Using Scanning Tunneling Microscopy", *Phys. Rev. Lett.* **60**, 1049 (1988).

[60] S. Rousset, S. Chiang, D. E. Fowler, and D. D. Chambliss, "Intermixing and 3-Dimensional Islands in the Epitaxial-Growth of Au on Ag(110)", *Phys. Rev. Lett.* **69**, 3200 (1992).

[61] M. Amrein, A. Stasiak, H. Gross, E. Stoll, and G. Travaglini, "Scanning Tunneling Microscopy of Reca-DNA Complexes Coated with a Conducting Film", *Science* **240**, 514 (1988).

[62] D. M. Eigler and E. K. Schweizer, "Positioning Single Atoms with a Scanning Tunneling Microscope", *Nature* **344**, 524 (1990).

[63] R. Otero, F. Rosei, and F. Besenbacher, "Scanning tunneling microscopy manipulation of complex organic molecules on solid surfaces", *Annu. Rev. Phys. Chem.* **57**, 497 (2006).

[64] S. Messerli, S. Schintke, K. Morgenstern, A. Sanchez, U. Heiz, and W. D. Schneider, "Imaging size-selected silicon clusters with a low-temperature scanning tunneling microscope", *Surf. Sci.* **465**, 331 (2000).

[65] H. J. Lee and W. Ho, "Single-bond formation and characterization with a scanning tunneling microscope", *Science* **286**, 1719 (1999).

[66] W. Hebenstreit, J. Redinger, Z. Horozova, M. Schmid, R. Podloucky, and P. Varga, "Atomic resolution by STM on ultra-thin films of alkali halides: experiment and local density calculations", *Surf. Sci.* **424**, L321 (1999).

[67] K. Glöcker, M. Sokolowski, A. Soukopp, and E. Umbach, "Initial growth of insulating overlayers of NaCl on Ge(100) observed by scanning tunneling microscopy with atomic resolution", *Phys. Rev. B* **54**, 7705 (1996).

[68] J. Repp, G. Meyer, S. M. Stojkovic, A. Gourdon, and C. Joachim, "Molecules on insulating films: Scanning-tunneling microscopy imaging of individual molecular orbitals", *Phys. Rev. Lett.* **94**, 026803 (2005).

[69] L. Ramoino, M. von Arx, S. Schintke, A. Baratoff, H. J. Guntherodt, and T. A. Jung, "Layer-selective epitaxial self-assembly of porphyrins on ultrathin insulators", *Chem. Phys. Lett.* **417**, 22 (2006).

[70] S. Schintke and W. D. Schneider, "Insulators at the ultrathin limit: electronic structure studied by scanning tunnelling microscopy and scanning tunnelling spectroscopy", *J. Phys.: Condens. Matter* **16**, R49 (2004).

[71] J. Bardeen, "Tunnelling from a Many-Particle Point of View", *Phys. Rev. Lett.* **6**, 57 (1961).

[72] J. Tersoff and D. R. Hamann, "Theory and Application for the Scanning Tunneling Microscope", *Phys. Rev. Lett.* **50**, 1998 (1983).

[73] J. Tersoff and D. R. Hamann, "Theory of the Scanning Tunneling Microscope", *Phys. Rev. B* **31**, 805 (1985).

[74] E. Lægsgaard, F. Besenbacher, K. Mortensen, and I. Stensgaard, "A Fully Automated, Thimble-Size Scanning Tunnelling Microscope", *J. Microsc-Oxford* **152**, 663 (1988).

[75] P. Sautet and C. Joachim, "Calculation of the Benzene on Rhodium Stm Images", *Chem. Phys. Lett.* **185**, 23 (1991).

[76] J. T. Nielsen, "NMR structural studies of locked nucleic acid modified nucleic acid complexes", *PhD thesis, Department of Chemistry and Physics, University of Southern Denmark, Denmark* (2006).

[77] C. D. Schwieters, J. J. Kuszewski, N. Tjandra, and G. M. Clore, "The Xplor-NIH NMR molecular structure determination package", *J. Magn. Reson.* **160**, 65 (2003).
CHAP 3

[78] T. Mallat, E. Orglmeister, and A. Baiker, "Asymmetric catalysis at chiral metal surfaces", *Chem. Rev.* **107**, 4863 (2007).

[79] L. M. Haupert and G. J. Simpson, "Chirality in Nonlinear Optics", *Annu. Rev. Phys. Chem.* **60**, 345 (2009).

[80] E. M. Arnett, J. Chao, B. J. Kinzig, M. V. Stewart, O. Thompson, and R. J. Verbiar, "Chiral Aggregation Phenomena. 3. Chiral Discrimination in the Monolayer Packing of N-(-Methylbenzyl)stearamides on Aqueous Acid Subphases: Thermodynamic Behavior", *J. Am. Chem. Soc.* **104**, 389 (1982).

[81] S. De Feyter, P. C. M. Grim, M. Rucker, P. Vanoppen, C. Meiners, M. Sieffert, S. Valiyaveettil, K. Mullen, and F. C. De Schryver, "Expression of chirality by achiral coadsorbed molecules in chiral monolayers observed by STM", *Angew. Chem. Int. Ed.* **37**, 1223 (1998).

[82] J. Weckesser, A. De Vita, J. V. Barth, C. Cai, and K. Kern, "Mesoscopic correlation of supramolecular chirality in one-dimensional hydrogen-bonded assemblies", *Phys. Rev. Lett.* **87**, 096101 (2001).

[83] M. C. Blum, E. Cavar, M. Pivetta, F. Patthey, and W. D. Schneider, "Conservation of chirality in a hierarchical supramolecular self-assembled structure with pentagonal symmetry", *Angew. Chem. Int. Ed.* **44**, 5334 (2005).

[84] A. Kühnle, T. R. Linderoth, and F. Besenbacher, "Self-assembly of monodispersed, chiral nanoclusters of cysteine on the Au(110)-(1 x 2) surface", *J. Am. Chem. Soc.* **125**, 14680 (2003).

[85] S. De Feyter, A. Gesquiere, K. Wurst, D. B. Amabilino, J. Veciana, and F. C. De Schryver, "Homo- and heterochiral supramolecular tapes from achiral, enantiopure, and racemic promesogenic formamides: Expression of molecular chirality in two and three dimensions", *Angew. Chem. Int. Ed.* **40**, 3217 (2001).

[86] A. Dally, "Thalidomide: was the tragedy preventable?" *Lancet* **351**, 1197 (1998).

[87] M. M. Green, M. P. Reidy, R. J. Johnson, G. Darling, D. J. Oleary, and G. Willson, "Macromolecular Stereochemistry - the out-of-Proportion Influence of Optically-Active Co-Monomers on the Conformational Characteristics of Polyisocyanates - the Sergeants and Soldiers Experiment", *J. Am. Chem. Soc.* **111**, 6452 (1989).

[88] M. M. Green, N. C. Peterson, T. Sato, A. Teramoto, R. Cook, and S. Lifson, "A Helical Polymer with a Cooperative Response to Chiral Information", *Science* **268**, 1860 (1995).

[89] A. R. A. Palmans and E. W. Meijer, "Amplification of chirality in dynamic supramolecular aggregates", *Angew. Chem. Int. Ed.* **46**, 8948 (2007).

[90] J. van Gestel, P. van der Schoot, and M. A. J. Michels, "Amplification of chirality in helical supramolecular polymers", *Macromolecules* **36**, 6668 (2003).

[91] J. van Gestel, "Amplification of chirality in helical supramolecular polymers: The majority-rules principle", *Macromolecules* **37**, 3894 (2004).

[92] M. M. Green, B. A. Garetz, B. Munoz, H. P. Chang, S. Hoke, and R. G. Cooks, "Majority Rules in the Copolymerization of Mirror-Image Isomers", *J. Am. Chem. Soc.* **117**, 4181 (1995).

[93] E. Yashima, T. Matsushima, and Y. Okamoto, "Chirality assignment of amines and amino alcohols based on circular dichroism induced by helix formation of a stereoregular poly((4-carboxyphenyl)acetylene) through acid-base complexation", *J. Am. Chem. Soc.* **119**, 6345 (1997).

[94] L. Brunsveld, E. W. Meijer, R. B. Prince, and J. S. Moore, "Self-assembly of folded m-phenylene ethynylene oligomers into helical columns", *J. Am. Chem. Soc.* **123**, 7978 (2001).

[95] A. Schenning, P. Jonkheijm, E. Peeters, and E. W. Meijer, "Hierarchical order in supramolecular assemblies of hydrogen-bonded oligo(p-phenylene vinylene)s", *J. Am. Chem. Soc.* **123**, 409 (2001).

[96] T. Ishi-i, M. Crego-Calama, P. Timmerman, D. N. Reinhoudt, and S. Shinkai, "Enantioselective formation of a dynamic hydrogen-bonded assembly based on the chiral memory concept", *J. Am. Chem. Soc.* **124**, 14631 (2002).

[97] M. A. Mateos-Timoneda, M. Crego-Calama, and D. N. Reinhoudt, "Amplification of chirality in hydrogen-bonded tetrarosette helices", *Chem. Eur. J.* **12**, 2630 (2006).

[98] M. Parschau, S. Romer, and K. H. Ernst, "Induction of homochirality in achiral enantiomorphous monolayers", *J. Am. Chem. Soc.* **126**, 15398 (2004).

[99] R. Fasel, M. Parschau, and K. H. Ernst, "Amplification of chirality in two-dimensional enantiomorphous lattices", *Nature* **439**, 449 (2006).

[100] J. D. Mougous, A. J. Brackley, K. Foland, R. T. Baker, and D. L. Patrick, "Formation of Uniaxial Molecular Films by Liquid-Crystal Imprinting in a Magnetic Field", *Phys. Rev. Lett.* **84**, 2742 (2000).

[101] H. Bulou and C. Goyhenex, "Local strain analysis of the herringbone reconstruction of Au(111) through atomistic simulations", *Phys. Rev. B* **65**, 045407 (2002).

[102] P. Kowalczyk, W. Kozlowski, Z. Klusek, W. Olejniczak, and P. K. Datta, "STM studies of the reconstructed Au(111) thin-film at elevated temperatures", *Appl. Surf. Sci.* **253**, 4715 (2007).

[103] F. Yin, R. Palmer, and Q. Guo, "Nanoscale surface recrystallization driven by localized electric field", *Phys. Rev. B* **73**, 073405 (2006).

[104] M. G. Wolf, J. A. Jongejan, J. D. Laman, and S. W. de Leeuw, "Quantitative Prediction of Amyloid Fibril Growth of Short Peptides from Simulations: Calculating Association Constants To Dissect Side Chain Importance", *J. Am. Chem. Soc.* **130**, 15772 (2008).

[105] A. Baumketner and J.-E. Shea, "Free energy landscapes for amyloidogenic tetrapeptides dimerization", B*iophys. J.* **89**, 1493 (2005).

[106] G. Bellesia and J.-E. Shea, "What Determines the Structure and Stability of KFFE Monomers, Dimers, and Protofibrils?", *Biophys. J.* **96**, 875 (2009).

[107] B. Strodel and D. J. Wales, "Implicit solvent models and the energy landscape for aggregation of the amyloidogenic KFFE peptide", *J. Chem. Theory Comput.* **4**, 657 (2008).

[108] L. Tjernberg, W. Hosia, N. Bark, J. Thyberg, and J. Johansson, "Charge attraction and beta propensity are necessary for amyloid fibril formation from tetrapeptides", *J. Biol. Chem.* **277**, 43243 (2002).

[109] V. Humblot, C. Methivier, R. Raval, and C. M. Pradier, "Amino acid and peptides on Cu(110) surfaces: Chemical and structural analyses of L-lysine", *Surf. Sci.* **601**, 4189 (2007).

[110] F. Tielens, V. Humblot, and C. M. Pradier, "Elucidation of the low coverage chiral adsorption assembly of L-lysine on Cu(110) surface: A theoretical study", *Surf. Sci.* **602**, 1032 (2008).

[111] A. Schiffrin, A. Riemann, W. Auwarter, Y. Pennec, A. Weber-Bargioni, D. Cvetko, A. Cossaro, M. Alberto, and J. V. Barth, "Zwitterionic self-assembly of L-methionine nanogratings on the Ag(111) surface", *Proc. Nat. Acad. Sci. U. S. A.* **104**, 5279 (2007).

[112] A. Kühnle, T. R. Linderoth, M. Schunack, and F. Besenbacher, "L-cysteine adsorption structures on Au(111) investigated by scanning tunneling microscopy under ultrahigh vacuum conditions", *Langmuir* **22**, 2156 (2006).

[113] R. R. Nazmutdinov, J. D. Zhang, T. T. Zinkicheva, I. R. Manyurov, and J. Ulstrup, "Adsorption and in situ scanning tunneling microscopy of cysteine on Au(111): Structure, energy, and tunneling contrasts", *Langmuir* **22**, 7556 (2006).

[114] E. M. Marti, A. Quash, C. Methivier, P. Dubot, and C. M. Pradier, "Interaction of S-histidine, an amino acid, with copper and gold surfaces, a comparison based on RAIRS analyses", *Colloids Surf. A: Physicochem. Eng. Aspects* **249**, 85 (2004).

[115] X. Y. Zhao, H. Yan, X. W. Tu, R. G. Zhao, and W. S. Yang, "Spillover-induced chemisorption of amino acid on silver surfaces", *Langmuir* **19**, 5542 (2003).

[116] L. M. Ghiringhelli, B. Hess, N. F. A. van der Vegt, and L. Delle Site, "Competing adsorption between hydrated peptides and water onto metal surfaces: From electronic to conformational properties", *J. Am. Chem. Soc.* **130**, 13460 (2008).

[117] C. Wang, L. X. Huang, L. J. Wang, Y. K. Hong, and Y. L. Sha, "One-dimensional self-assembly of a rational designed beta-structure peptide", *Biopolymers* **86**, 23 (2007).

[118] Z. G. Wang, C. Q. Zhou, C. Wang, L. J. Wan, X. H. Fang, and C. L. Bai, "AFM and STM study of beta-amyloid aggregation on graphite", *Ultramicroscopy* **97**, 73 (2003).

[119] C. Whitehouse, J. Y. Fang, A. Aggeli, M. Bell, R. Brydson, C. W. G. Fishwick, J. R. Henderson, C. M. Knobler, R. W. Owens, N. H. Thomson, D. A. Smith, and N. Boden, "Adsorption and self-assembly of peptides on mica substrates", *Angew. Chem. Int. Ed.* **44**, 1965 (2005).

[120] M. Lepère, C. Chevallard, G. Brezesinski, M. Goldmann, and P. Guenoun, "Crystalline Amyloid Structures at Interfaces", *Angew. Chem. Int. Ed.* **48**, 5005 (2009).

[121] S. M. Barlow, S. Haq, and R. Raval, "Bonding, organization, and dynamical growth behavior of tripeptides on a defined metal surface: Tri-L-alanine and tri-L-leucine on Cu100", Langmuir 17, 3292 (2001).

[122] Y. Wang, M. Lingenfelder, T. Classen, G. Costantini, and K. Kern, "Ordering of dipeptide chains on cu surfaces through 2D cocrystallization", *J. Am. Chem. Soc.* **129**, 15742 (2007)

[123] S. Maier, L. A. Fendt, L. Zimmerli, T. Glatzel, O. F. Pfeiffer, F. Diederich, and E. Meyer, "Nanoscale engineering of molecular porphyrin wires on insulating surfaces", *Small* **4**, 1115 (2008).

[124] T. Kunstmann, A. Schlarb, M. Fendrich, T. Wagner, R. Moller, and R. Hoffmann, "Dynamic force microscopy study of 3,4,9,10-perylenetetracarboxylic dianhydride on KBr(001)", *Phys. Rev. B* **71**, 121403(R) (2005).

[125] L. Nony, R. Bennewitz, O. Pfeiffer, E. Gnecco, A. Baratoff, E. Meyer, T. Eguchi, A. Gourdon, and C. Joachim, "Cu-TBPP and PTCDA molecules on insulating surfaces studied by ultra-high-vacuum non-contact AFM", *Nanotechnology* **15**, S91 (2004).

[126] L. Nony, E. Gnecco, A. Baratoff, A. Alkauskas, R. Bennewitz, O. Pfeiffer, S. Maier, A. Wetzel, E. Meyer, and C. Gerber, "Observation of individual molecules trapped on a nanostructured insulator", *Nano Lett.* **4**, 2185 (2004).

[127] A. Scarfato, S. H. Chang, S. Kuck, J. Brede, G. Hoffmann, and R. Wiesendanger, "Scanning tunneling microscope study of iron(II) phthalocyanine growth on metals and insulating surfaces", *Surf. Sci.* **602**, 677 (2008).

[128] E. Cavar, M. C. Blum, M. Pivetta, F. Patthey, M. Chergui, and W. D. Schneider, "Fluorescence and phosphorescence from individual C-60 molecules excited by local electron tunneling", *Phys. Rev. Lett.* **95**, 196102 (2005).

[129] C. J. Villagomez, T. Zambelli, S. Gauthier, A. Gourdon, C. Barthes, S. Stojkovic, and C. Joachim, "A local view on hyperconjugation", *Chem. Phys. Lett*. **450**, 107 (2007).

[130] S. W. Wu, G. V. Nazin, X. Chen, X. H. Qiu, and W. Ho, "Control of relative tunneling rates in single molecule bipolar electron transport", *Phys. Rev. Lett.* **93**, 236802 (2004).

[131] R. Bennewitz, "Structured surfaces of wide band gap insulators as templates for overgrowth of adsorbates", *J. Phys.: Condens. Matter* **18**, R417 (2006).

[132] C. Barth and M. Reichling, "Imaging the atomic arrangements on the high-temperature reconstructed alpha-Al2O3(0001) surface", *Nature* **414**, 54 (2001).

[133] R. Hoffmann, L. N. Kantorovich, A. Baratoff, H. J. Hug, and H. J. Guntherodt, "Sublattice identification in scanning force microscopy on alkali halide surfaces", *Phys. Rev. Lett.* **92**, 146103 (2004).

[134] J. Viernow, D. Y. Petrovykh, A. Kirakosian, J. L. Lin, F. K. Men, M. Henzler, and F. J. Himpsel, "Chemical imaging of insulators by STM", *Phys. Rev. B* **59**, 10356 (1999).

[135] W. Hebenstreit, M. Schmid, J. Redinger, R. Podloucky, and P. Varga, "Bulk terminated NaCl(111) on aluminum: A polar surface of an ionic crystal?", *Phys. Rev. Lett.* **85**, 5376 (2000).

[136] M. Pivetta, F. Patthey, M. Stengel, A. Baldereschi, and W. D. Schneider, "Local work function Moire pattern on ultrathin ionic films: NaCl on Ag(100)", *Phys. Rev. B* **72**, 115404 (2005).

[137] J. Repp and G. Meyer, "Scanning tunneling microscopy of adsorbates on insulating films. From the imaging of individual molecular orbitals to the manipulation of the charge state", *Appl. Phys. A: Mater. Sci. Process.* **85**, 399 (2006).

[138] I. Mauch, G. Kaindl, and A. Bauer, "Formation of NaCl stripes on Cu(100)", *Surf. Sci.* **522**, 27 (2003).

[139] F. E. Olsson and M. Persson, "A density functional study of adsorption of sodium-chloride overlayers on a stepped and a flat copper surface", *Surf. Sci.* **540**, 172 (2003).

[140] R. Bennewitz, V. Barwich, M. Bammerlin, C. Loppacher, R. Guggisberg, A. Baratoff, E. Meyer, and H. J. Guntherodt, "Ultrathin films of NaCl on Cu(111): a LEED and dynamic force microscopy study", *Surf. Sci.* **438**, 289 (1999).

[141] J. Repp, G. Meyer, and K. H. Rieder, "Snell's law for surface electrons: Refraction of an electron gas imaged in real space", *Phys. Rev. Lett.* **92**, 036803 (2004).

[142] J. Repp, G. Meyer, S. Paavilainen, F. E. Olsson, and M. Persson, "Imaging bond formation between a gold atom and pentacene on an insulating surface", *Science* **312**, 1196 (2006).

[143] H. Rauscher, T. A. Jung, J. L. Lin, A. Kirakosian, F. J. Himpsel, U. Rohr, and K. Mullen, "One-dimensional confinement of organic molecules via selective adsorption on CaF1 versus CaF2", *Chem. Phys. Lett.* **303**, 363 (1999).

[144] C. Loppacher, U. Zerweck, and L. M. Eng, "Kelvin probe force microscopy of alkali chloride thin films on Au(111)", *Nanotechnology* **15**, S9 (2004).

[145] J. Repp, S. Folsch, G. Meyer, and K. H. Rieder, "Ionic films on vicinal metal surfaces: Enhanced binding due to charge modulation", *Phys. Rev. Lett.* **86**, 252 (2001).

[146] C. Schwennicke, J. Schimmelpfennig, and H. Pfnur, "Morphology of Thin Nacl Films Grown Epitaxially on Ge(100)", *Surf. Sci.* **293**, 57 (1993).

[147] D. R. Lide, *CRC handbook of chemistry and physics*, 80th ed. (CRS Press, Boca Raton, Florida, 1999).

[148] G. M. Whitesides, E. E. Simanek, J. P. Mathias, C. T. Seto, D. N. Chin, M. Mammen, and D. M. Gordon, "Noncovalent Synthesis - Using Physical-Organic Chemistry to Make Aggregates", Acc. Chem. Res. 28, 37 (1995).

[149] F. Moresco, "Manipulation of large molecules by low-temperature STM: model systems for molecular electronics", Phys. Rep. 399, 175 (2004).

[150] F. Moresco and A. Gourdon, "Scanning tunneling microscopy experiments on single molecular landers", Proc. Nat. Acad. Sci. U. S. A. 102, 8809 (2005).

[151] L. Grill and F. Moresco, "Contacting single molecules to metallic electrodes by scanning tunnelling microscope manipulation: model systems for molecular electronics", J. Phys.: Condens. Matter 18, S1887 (2006).

[152] L. Grill, K. H. Rieder, F. Moresco, S. Stojkovic, A. Gourdon, and C. Joachim, "Exploring the interatomic forces between tip and single molecules during STM manipulation", Nano Lett. 6, 2685 (2006).

[153] L. Grill, K. H. Rieder, F. Moresco, S. Stojkovic, A. Gourdon, and C. Joachim, "Controlling the electronic interaction between a molecular wire and its atomic scale contacting pad", Nano Lett. 5, 859 (2005).

[154] R. Otero, F. Hummelink, F. Sato, S. B. Legoas, P. Thostrup, E. Laegsgaard, I. Stensgaard, D. S. Galvao, and F. Besenbacher, "Lock-and-key effect in the surface diffusion of large organic molecules probed by STM", Nat. Mater. 3, 779 (2004).

[155] F. Rosei, M. Schunack, P. Jiang, A. Gourdon, E. Laegsgaard, I. Stensgaard, C. Joachim, and F. Besenbacher, "Organic molecules acting as templates on metal surfaces", Science 296, 328 (2002).

[156] R. Otero, F. Rosei, Y. Naitoh, P. Jiang, P. Thostrup, A. Gourdon, E. Laegsgaard, I. Stensgaard, C. Joachim, and F. Besenbacher, "Nanostructuring Cu surfaces using custom-designed molecular molds", Nano Lett. 4, 75 (2004).

[157] L. Gross, K. H. Rieder, F. Moresco, S. M. Stojkovic, A. Gourdon, and C. Joachim, "Trapping and moving metal atoms with a six-leg molecule", Nat. Mater. 4, 892 (2005).

[158] X. Ge, J. Kuntze, R. Berndt, H. Tang, and A. Gourdon, "Tunneling spectroscopy of lander molecules on coinage metal surfaces", Chem. Phys. Lett. 458, 161 (2008).

[159] R. Otero, Y. Naitoh, F. Rosei, P. Jiang, P. Thostrup, A. Gourdon, E. Laegsgaard, I. Stensgaard, C. Joachim, and F. Besenbacher, "One-dimensional assembly and selective orientation of lander molecules on an O-Cu template", Angew. Chem. Int. Ed. 43, 2092 (2004).

[160] Y. Naitoh, F. Rosei, A. Gourdon, E. Laegsgaard, I. Stensgaard, C. Joachim, and F. Besenbacher, "Scanning Tunneling Microscopy and Spectroscopy Studies of Individual Lander Molecules Anchored on a Copper Oxide Nanotemplate", J. Phys. Chem. C 112, 16118 (2008).

[161] J. Kuntze, X. Ge, and R. Berndt, "Chiral structures of lander molecules on Cu(100)", Nanotechnology 15, S337 (2004).

[162] M. Schunack, F. Rosei, Y. Naitoh, P. Jiang, A. Gourdon, E. Laegsgaard, I. Stensgaard, C. Joachim, and F. Besenbacher, "Adsorption behavior of Lander molecules on Cu(110) studied by scanning tunneling microscopy", J. Chem. Phys. 117, 6259 (2002).

[163] L. Gross, F. Moresco, P. Ruffieux, A. Gourdon, C. Joachim, and K. H. Rieder, "Tailoring molecular self-organization by chemical synthesis: Hexaphenylbenzene, hexa-peri-hexabenzocoronene, and derivatives on Cu(111)", Phys. Rev. B 71, 165428 (2005).

[164] R. Barattin and A. Gourdon, "Synthesis of Two Complementary Molecular Moulds", Eur. J. Org. Chem., 1022 (2009).

[165] T. Zambelli, S. Goudeau, J. Lagoute, A. Gourdon, X. Bouju, and S. Gauthier, "Molecular self-assembly of jointed molecules on a metallic substrate: From single molecule to monolayer", ChemPhysChem 7, 1917 (2006).

[166] N. L. Allinger, K. S. Chen, and J. H. Lii, "An improved force field (MM4) for saturated hydrocarbons", J. Comput. Chem. 17, 642 (1996).

[167] M. E. Cañas-Ventura, W. Xiao, D. Wasserfallen, K. Mullen, H. Brune, J. V. Barth, and R. Fasel, "Self-assembly of periodic bicomponent wires and ribbons", Angew. Chem. Int. Ed. 46, 1814 (2007).

[168] L. M. A. Perdigão, E. W. Perkins, J. Ma, P. A. Staniec, B. L. Rogers, N. R. Champness, and P. H. Beton, "Bimolecular networks and supramolecular traps on Au(111)", J. Phys. Chem. B 110, 12539 (2006).

[169] F. Silly, A. Q. Shaw, M. R. Castell, G. A. D. Briggs, M. Mura, N. Martsinovich, and L. Kantorovich, "Melamine structures on the Au(111) surface", J. Phys. Chem. C 112, 11476 (2008).

[170] M. Mura, N. Martsinovich, and L. Kantorovich, "Theoretical study of melamine superstructures and their interaction with the Au(111) surface", Nanotechnology 19, 465704 (2008).

[171] A. Miura, P. Jonkheijm, S. De Feyter, A. Schenning, E. W. Meijer, and F. C. De Schryver, "2D self-assembly of oligo(p-phenylene vinylene) derivatives: From dimers to chiral rosettes", Small 1, 131 (2005).

[172] I. E. Knaggs, K. Lonsdale, R. G. Wood, and G. Williams, "The Structure of Melamine, $C_3N_6H_6$", Proc. R. Soc. London, Ser. A 177, 140 (1940).

Acknowledgements

The multidisciplinary research presented in this thesis was made possible through a collaborative effort and accounts for the work that was done during my PhD studies in the SPM group at the Interdisciplinary Nanoscience Center (iNANO), in the Department of Physics and Astronomy, University of Aarhus. During my PhD I had the great pleasure of collaborating with a large number of people skilled in chemistry, surface science, biochemistry, and theoretical physics. All of these collaborators and friends have been very helpful for me during my stay at iNANO and I would like to thank them.

First, I would like to especially acknowledge my supervisor Trolle R. Linderoth for his guidance, advice, and enthusiasm in all the areas covered by this thesis. He was teaching me a lot during these three years for writing papers and presenting conferences, but also I learned from him most of the highly compelling knowledge necessary for ultra high vacuum and STM technologies. I would like to thank Christian Bombis who trained me at the beginning of my PhD studies. I thank my collaborators Sigrid Weigelt, Miao Yu, Federico Masini, Wei Xu, as well as Erik Lægsgaard who often solved delicate technical issues related to STM equipment. I am also very grateful to Flemming Besenbacher for providing the opportunity of working within the Marie-Curie Early Stage Training network MONET. I am very grateful to Enette Berndt Knudsen who helped me a lot for adminisitrative issues relative to the organization of my PhD studies in Denmark.

I thank Niels Chr. Nielsen and Daniel Otzen for supplying peptides molecules which I have extensively studied in this work. This allowed me to become acquainted with a fascinating topics in biophysics, and to create strong scientific links with Jakob Toudahl Nielsen who brillantly succeeded to model some of the surprisingly numerous tetrapeptide self-assemblies I have described in Chapter 4. I am indebted to Martin M. Nielsen in the group of Kurt Gothelf, iNANO, Department of Chemistry who synthesised the chiral *sec*-butyl compound discussed in Chapter 3. I thank André Gourdon and Xavier Bouju at CEMES-CNRS in Toulouse who provided the Lander compounds discussed in Chapter 6 and carried out the EHMO-ESQC calculations. Finally, I would like to thank T. Eralp from the University of Reading, who visited the group in 2009 and with whom I spent excellent time in studying amino acid adsorption on surfaces.